STRUCTURAL AND MAGNETIC CHARACTERIZATION OF NITROGEN ION IMPLANTED STAINLESS STEEL AND CoCrMo ALLOYS

A Thesis submitted to
the Graduate School of Engineering and Sciences of
İzmir Institute of Technology
in Partial Fulfilment of the Requirements for the Degree of

MASTER OF SCIENCE

in Physics

by
Mehmet FİDAN

January 2014
İZMİR

We approve the thesis of **Mehmet FİDAN**

Examining Committee Members:

_____

Prof. Dr. Orhan ÖZTÜRK
Department of Physics, Izmir Institute of Technology

_____

PD. Dr. Stephan MÄNDL
Plasma Physics, Leibniz-Institut für Oberflächenmodifizierung

_____

Assoc. Prof. Dr. Sami SÖZÜER
Department of Physics, Izmir Institute of Technology

_____

Prof. Dr. M. Ahmet ÖZTARHAN
Department of BioEngineering, Ege University

_____

Prof. Dr. Saim SELVİ
Department of Physics, Ege University

03 January 2014

_____

Prof. Dr. Orhan ÖZTÜRK
Supervisor, Department of Physics,
Izmir Institute of Technology

_____ _____

Prof. Dr. Nejat BULUT
Head of the Department of Physics

Prof. Dr. R. Tugrul SENGER
Dean of the Graduate School of
Engineering and Sciences

ACKNOWLEDGEMENTS

First of all, I would like to thank my advisor, Prof. Dr. Orhan Öztürk. His encouragement and support made this thesis possible. I am very grateful for his invaluable help, guidance, encouragement and his endless patience as well as his understanding provided during this thesis. The work presented here is part of a joint project between Department of Physics, Izmir Institute of Technology, Turkey and Leibniz Institute of Surface Modification, Leibniz, Germany. I would like to thank Dr. Stephan Mändle and his research group for carrying out the Plasma Immersion Ion Implantatin (PIII) of stainless steel and CoCrMo alloys, providing nitrogen-depht and hardness measurements. I am very thankful to TIPSAN (Izmir) for providing the stainless steel and CoCrMo alloy materials. Special thanks go to thank the staff of Material Research Center of Izmir Institute of Technology for their contribution. Also, I would like to acknowledge my institution, Izmir Institute of Technology, for providing me research facilities during my graduate study. I would like to thank Gökhan Özdemir of MikronMak Kalıp (Manisa, Turkey) for cross-sectional sample preparation by providing wire electrical discharge machine. My other big ‘’Thank you!’’ is to Prof. Dr. Mustafa Güden for providing polishing system.

Finally, I can’t find better words to explain contribution of my family to my education. Especially, I want to thank my mother for her understanding, support, and love since elementary school.

ABSTRACT

STRUCTURAL AND MAGNETIC CHARACTERIZATION OF NITROGEN ION IMPLANTED STAINLESS STEEL AND CoCrMo ALLOYS

Ion beam surface modification methods can be used to create hard and wear resistant surface layers with enhanced corrosion resistance on austenitic stainless steels (SS) and CoCr base alloys using nitrogen ions. This is mainly due to the formation of high N content phase, γ_N, at relatively low substrate temperatures from about 350 to 450 ºC. This surface layer is known as an expanded austenite layer. Different N contents and diffusion rates depending on grain orientations as well as anisotropic lattice expansion and high residual stresses are some peculiar properties associated with the formation of this phase. Another peculiar feature of the expanded austenite phase is related to its magnetic character.

In this study, new data related to the magnetic nature of the expanded austenite layers on austenitic stainless steel (304 SS) and CoCrMo alloy by nitrogen plasma immersion ion implantation (PIII) are presented. Magnetic behaviour, nitrogen distribution, implanted layer phases, surface topography, and surface hardness were studied with a combination of experimental techniques involving magnetic force microscopy, SIMS, XRD, SEM, AFM and nanoindentation method.

The experimental analyses indicate that the low temperature samples clearly show the formation of the expanded austenite phase, while the decomposition of this metastable phase into CrN precipitates occurs at higher temperatures. As a function of the processing temperature, phase evolution stage for both alloys follows the same trend: (1) initial stage of the expanded phase, γ_N, formation; (2) its full development, and (3) its decomposition into CrN precipitates and the Cr-depleted matrix, fcc γ-(Co,Mo) for CoCrMo and bcc α-(Fe,Ni) for 304 SS.

MFM imaging reveals distinct, stripe-like ferromagnetic domains for the fully developed expanded austenite layers both on 304 SS and CoCrMo alloys. Weak domain structures are observed for the CoCrMo samples treated at low and high processing temperatures. The images also provide strong evidence for grain orientation dependence of magnetic properties. The ferromagnetic state for the γ_N phase observed here is mainly linked to large lattice expansions due to high N content.

ÖZET

AZOT İYON İMPLANTE EDİLMİŞ PASLANMAZ ÇELİK VE CoCrMo ALAŞIMLARININ YAPISAL VE MANYETİK KARAKTERİZASYONU

İyon demeti yüzey modifikasyon metotları, azot iyonları kullanarak ostenitik paslanmaz çelikler ve CoCrMo baz alaşımlarının yüzeylerinde sert ve gelişmiş korozyon direncine sahip sert yüzey tabakaları oluşturmak için kullanılabilir. Bu durum başlıca 350 - 450 ºC gibi görece düşük altlık sıcaklıklarında yüksek N içeren γ_N fazı oluşumundan ileri gelir. Bu tabaka genişlemiş ostenit tabakası olarak bilinir. Farklı N içeriği ve difüzyon hızına bağlı olarak tane yönlenmeleri ile birlikte anizotropik kafes genleşmesi ve yüksek artık gerilmeler bu fazın oluşumuna has özelliklerdir. Genişlemiş ostenit fazına has bir diğer ilginç özellik de bu fazın manyetik karakteri ile ilgilidir.

Bu çalışmada, ostenitik paslanmaz çelik (304 SS) ve CoCrMo alaşımı üzerinde azot plazma daldırma iyon implantasyonu ile oluşturulan genişlemiş ostenit tabakalarının manyetik doğası ile ilgili yeni veriler sunulmuştur. Manyetik davranış, azot dağılımı, implantasyon tabakası fazları, yüzey topografisi ve yüzey sertliği manyetik kuvvet mikroskopisi, SIMS, XRD, SEM, AFM ve nanoindentasyon metotlarını içeren deneysel teknikler bileşimiyle incelenmiştir.

Deneysel analizler, düşük sıcaklıktaki numunelerin açık bir şekilde genişlemiş ostenit tabakası oluşumu gösterdiğine işaret ederken, yüksek sıcaklarda yarıkararlı bu faz CrN çökeleklerine dönüşür. Faz gelişim aşamaları her iki alaşım için de işlem sıcaklığının bir fonksiyonu olarak aynı trendi takip eder: (1) genişlemiş faz, γ_N, oluşumunun başlangıç evresi; (2) tam gelişmesi ve (3) CrN çökeleklerine ve Cr fakir matrikse bozunması (CoCrMo için fcc γ-(Co,Mo) ve 304 SS için bcc α-(Fe,Ni)).

MFM görüntülemesi, hem 304 SS hem de CoCrMo alaşım yüzeylerinde tam oluşmuş genleşmiş ostenit tabakaları için belirgin, şerit şeklinde ferromanyetik domainler ortaya çıkarmıştır. Düşük ve yüksek sıcaklıklarda işlem görmüş CoCrMo numunelerinde zayıf domain yapıları gözlenmiştir. Görüntüler ayrıca manyetik özelliklerin tane hizalanmasına olan bağımlılığı hakkında güçlü deliller sağlamaktadır. γ_N fazında gözlenen ferromanyetik durum temel olarak yüksek N içeriği nedeniyle oluşan aşırı kafes genişlemelerine bağlanmıştır.

To my Family

TABLE OF CONTENTS

LIST OF FIGURES

Figure **Page**

LIST OF TABLES

CHAPTER 1

INTRODUCTION

Austenitic stainless steels and CoCr alloys are widely used in medical applications such as dental implants, bone plates, stents and prosthesis due to their high corrosion resistance, wear resistance and biocompatibility. Figure 1.1 shows the components of a hip prosthesis. CoCr alloys have greater wear resistance as compared to stainless steel since CoCr alloys have the higher Cr content (~ 30 at.%) than austenitic stainless steels (~ 18-20 at.%). In addition, their non-magnetic properties at room temperature are necessary because of magnetic resonance imaging.

Figure 1.1. Hip implant prosthesis.

However, some problems are found with these materials in medical applications. There is unavoidable corrosion and wear of them in body fluid, such as crevice corrosion and fretting corrosion (Kamachimudali et al., 2003; Walczak et al., 1998). These factors probably lead to an early fracture or failure of the implanted materials, and corrosion of the implanted materials may result in release of harmful products into the body. Another important problem is the negative effect of metal ions or fretting debris, which can be released from the surface of the materials due to corrosion and wear (Pulido and Parrish, 2003). When the materials are placed in body, toxic metal

ions such as Co, Cr and Ni may release into the body environments, which may give rise to significant health concerns over time.

In order to improve surface properties of these materials, nitrogen ion beam surface modification methods can be used to form protective layers on the surface of these alloys by modifying the near surface layers of these materials (Buhagiar and Dong, 2012; Zhang and Bell, 1985). Not only nitrogen is used in surface modification but also carbon, boron and inert ions (Ar, He). Nitrogen has been extensively studied with respect to others due to its abundance in nature and the results in improved properties such as wear, corrosion resistances and also fatigue resistance.

Surface modification by inserting nitrogen ions with plasma and ion implantation techniques offers improvements to the properties of metallic materials. These techniques contain plasma nitriding, plasma immersion ion implantation (PIII) and conventional beam line ion implantation. The main differences between these techniques are the varying ion energy and the relative fraction of energetic ions, electrons, thermal atoms and ions impinging on the surface (Roth, 2002).

In this study, the nitrogen implantation into stainless steel and CoCrMo alloys will be carried out by plasma immersion ion implantation (PIII) method, where positive ions are extracted from the plasma by applying negative high voltage pulses to the substrate and simultaneously accelerated towards the whole surface. PIII is a very appealing technique for industrial applications as it overcomes the line-of-sight restrictions of conventional ion beam implantation and also for the possibility of implanting complex, three-dimensional materials.

Different surface modification methods for nitrogen insertion into stainless steel and CoCr base alloys have been described in the literature, including plasma nitriding (Baranowska, 2004; Öztürk et al., 2011; Öztürk et al., 2009), plasma immersion ion implantation (Lutz et al., 2011a; Manova et al., 2009) and conventional ion beam implantation (Blawert et al., 2001; Wei et al., 1996). All these methods can be used to create hard and wear resistant surface layers with enhanced corrosion resistance on austenitic stainless steels (SS) and CoCr base alloys using nitrogen ions (Bazzoni et al., 2013; Lutz et al., 2008a; Mandl and Rauschenbach, 2000; Ozturk and Williamson, 1995; Pichon et al., 2010; Williamson et al., 1994). This is mainly due to the formation of a metastable, high N content phase, γ_N, at relatively low substrate temperatures from about 350 to 450 ºC. This surface layer is known as an expanded austenite layer. Different N contents and diffusion rates depending on grain orientation as well as

anisotropic lattice expansion and high residual stresses are some peculiar properties associated with the formation of this phase (Ozturk and Williamson, 1995; Williamson et al., 1994). Another peculiar feature of the expanded austenite phase is related to its magnetic character: the expanded phase/layer is found to have ferromagnetic as well as paramagnetic characteristics depending on its N contents (20-30 at.%) and associated lattice expansions (as high as 10%) (Ozturk and Williamson, 1995).

The magnetic nature of the γ_N phase was first reported by Ichii et al. in 1986. This study (K. Ichii, 1986), involving low temperature nitriding of 304 SS at 400 ºC, found that the nitrided layer was composed of the γ_N phase (the term they used was S-Phase) and was of ferromagnetic nature. A much later study (Ozturk and Williamson, 1995) involving low-energy, high-flux N implantation of 304 SS at 400 ºC revealed more details about the magnetic nature of the γ_N phase. Through Mössbauer spectroscopy and MOKE this investigation found the expanded phase to be ferromagnetically soft in nature, and to be distributed in the highest concentration region of the implanted layer. The γ_N phase transforms to the paramagnetic state deeper into the layer as the N content and associated lattice expansion decreased. That study (Ozturk and Williamson, 1995) suggested that the ferromagnetic γ_N phase is achieved above a certain threshold of N content (above about 20 at.%). Two recent studies, involving ion and gas-phase nitride 316 stainless steel (Basso et al., 2009; Wu et al., 2011), however, find a lower threshold N content value, about 14 at.%, for the ferromagnetic expanded phase. After the detailed study (Ozturk and Williamson, 1995), a number of publications reported observations related to the magnetic character of the γ_N phase formed on austenitic SSs (Fewell et al., 2000; Menéndez et al., 2008; Menéndez et al., 2010; Öztürk et al., 2009). More recently, the ferromagnetic nature of the γ_N phase in austenitic SS alloys was revealed through the observation of stripe-like domains via magnetic force microscopy (MFM) imaging and through the observation of hysteresis loops via magneto-optic Kerr effect (MOKE) (Menéndez et al., 2013; Öztürk et al., 2009). In these studies, the origin of the magnetism in the γ_N phase is mainly explained by large lattice expansions (due to high N contents), and should eventually be related to the underlying origins of the magnetic effect in fcc-Fe and related alloys. Some other researchers link the ferromagnetism of the γ_N phase to various defects (stacking faults, twins, etc.) observed in the expanded phase layers (Blawert et al., 2001).

While, according to literature of the last twenty years, there has been considerable amount of research related to the expanded austenite phase in CoCr based alloys (the expanded phase in CoCrMo alloy was first reported by Wei et al. in 2004 (Lanning and Wei, 2004)), there is only one study related to the magnetic nature of the γ_N phase in this alloy system (Öztürk et al., 2011). This study involving low temperature nitriding of CoCrMo alloy at 400 ºC provided strong evidence for the ferromagnetic nature of the γ_N phase in this alloy through MFM observation of stripe domain structures as well as the hysteresis loops obtained through MOKE analysis.

Although the expanded phase itself has now been studied in detail by various research groups, its magnetic nature has been relegated to a minor role. Instead, the focus rather has been on mechanical, tribological, corrosion, and biocompatibility of expanded layers. However, there may be possible applications for magnetic γ_N layers on non-magnetic substrates, underlying fcc γ phases of austenitic SS and CoCrMo alloys have paramagnetic properties at room temperature. Two possible application areas that may utilize the magnetism of the expanded phase may be magnetic recording (H. Sanda et. al., 1990) and magnetic separation (very localized zone for trapping magnetic particles) (Menéndez et al., 2008). On the other hand, the ferromagnetism of the expanded phase is probably unwelcome for biomedical SSs and CoCr based alloys, particularly from the view point of magnetic resonant imaging (i.e., MR compatibility).

In this research, new data related to the magnetic nature of the expanded austenite layer/phase formed on CoCrMo and 304 SS alloys by nitrogen plasma immersion ion implantation (PIII) is presented. The purpose of this study is to improve our understanding of surface modification of 304 SS and CoCrMo alloy with nitrogen plasma immersion ion implantation process. In addition to structural, topographical and magnetic properties, nitrogen depht profiles and hardness features of the N implanted layers at processing temperatures ranging from 300 to 550 °C for fixed one hour are investigated. This will be accomplished by experimental characterization, using X-ray diffraction in both $\theta/2\theta$ geometry and grazing incidence (GIXRD) mode, atomic force microscopy (AFM), magnetic force microscopy (MFM), scanning electron microscopy (SEM), secondary ion mass spectroscopy (SIMS), energy dispersive X-ray (EDX), nanoindentation measurements with a Berkovic indenter.

CHAPTER 2

MATERIALS AND EXPERIMENTAL METHODS

2.1. Austenitic Stainless Steel and CoCrMo Alloy

Austenitic stainless steel and CoCrMo are alloys of composition Fe, Cr, Ni and Co, Cr, Mo. Stainless steels can be divided into three different groups depending on their crystal structure at room temperature. These are austenitic, ferritic, martensitic stainless steel corresponding to face-centered cubic (fcc), body-centered cubic (bcc) and body-centered tetragonal (bct) crystal lattice structure, respectively.

Austenitic stainless steel (304 SS) and cobalt-chromium-molybdenum (CoCrMo) alloy (ISO 5832-12) are the investigated materials in this study. These samples provided by TIPSAN are cut from cylindrical bars and used as substrates. The specimens have disc-like geometry with a diameter of 16 mm and a thickness of 4 mm for 304 SS; a diameter of 14 mm and a thickness of 4 mm for CoCrMo alloy. Both materials used in this work have mainly face-centered cubic (fcc-γ) crystal structure and are non-magnetic at room temperature. Figure 2.1 illustrates lattice structures of these materials (these simulations were carried out using VESTA software program).

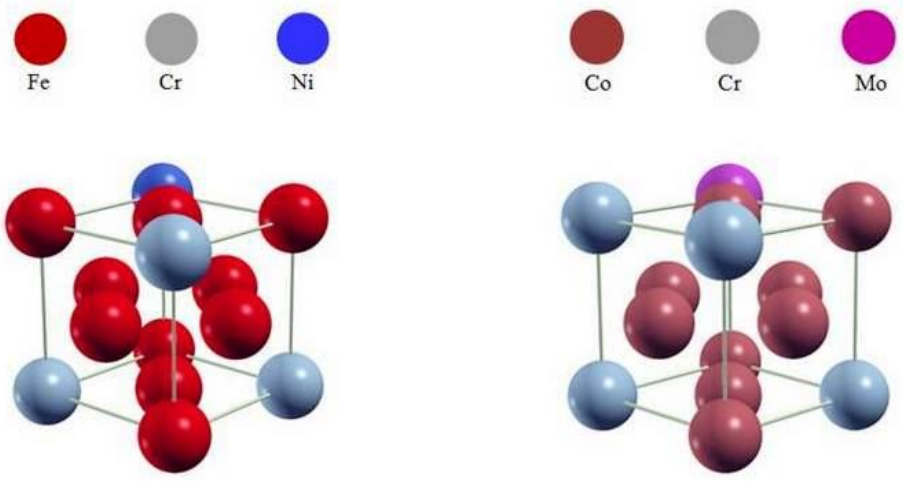

Figure 2.1. A view of fcc γ-(Fe,Cr,Ni) and fcc γ-(Co,Cr,Mo) lattice

According to literature (Öztürk et al., 2009; Öztürk et al., 2006), while the grain sizes of 304 SS are between 25 and 50 μm, the grain size of CoCrMo alloy changes from 5 to 15 μm.

The main chemical composition of the alloys used in this study is listed in Table 2.1 in weight percentage (wt.%) and atomic percentage (at.%).

Table 2.1. Chemical composition in both wt.% and at.% of 304 SS and CoCrMo alloy samples used in this study. In this table, only the main elements of the samples are listed. The balance is either provided by Fe or Co, depending on the alloy class.

304 SS		Cr	Ni	Mn	Si	C	Fe
	wt.%	18.30	8.30	1.42	0.43	0.045	Bal.
	at.%	19.39	7.79	1.42	0.84	0.21	Bal.

CoCrMo		Cr	Mo	Mn	Si	C	Co
	wt.%	27.92	5.86	0.59	0.72	0.048	Bal.
	at.%	30.87	3.51	0.61	1.47	0.23	Bal.

In both alloys, chemical elements are randomly distributed on substitutional sites of the lattice. To stabilize austenitic structure it is necessary to add about 8% nickel (Gavriljuk and Berns, 1999). Chromium causes the formation of a very thin chromium-containing oxide layer at the surface. This formation can help protect these alloys from corrosion. In addition, the other elements like nickel, manganese, silicon, carbon etc. can be added to give characteristic properties such as strength, toughness or hardenability to the alloy (Khatak and Raj, 2002).

2.2. Sample Preparation

Sample preparation mainly involves polishing before nitrogen plasma immersion ion implantation process. All the disc-shaped samples, obtained from TIPSAN, were polished to mirror-like quality observed by AFM. Additionally, the cross-sectional samples were prepared in order to observe the nitrogen implanted layer thickness.

2.2.1. Polishing

Prior to nitrogen plasma immersion ion implantation process, all the specimens were polished to mirror-like quality by using a polishing system (Buehler) at IYTE. The polishing was performed in two steps: (i) polishing with SiC papers and (ii) polishing with diamond suspension solutions,

i. All samples were polished with SiC grinding papers (with 320, 600, 800, 1200 grid sizes). In this case, approximately 5 N force was applied for 5 minutes. Then 2400 grinding paper was applied with the same force for 10 minutes. After each step, the samples were cleaned in distilled water.
ii. Polishing cloths and diamond suspension solutions (9 μm, 3 μm, 1 μm) were used. For each step, a force of 5 N was applied. Firstly, 9 μm diamond solution was used for 10 minutes. Secondly, 3 μm diamond solution was used for 15 minutes and lastly, 1 μm diamond solution was used for 20 minutes. After each step, samples were cleaned with ethanol in ultrasonic cleaner for 10 minutes, then cleaned in distilled water.

The main parts of the polishing equipments used in this study can be seen in Figure 2.2.

Figure 2.2. Polishing equipments

2.2.2. Cross-Sectional Sample Preparation

Cross-sectional sample preparation involves nitrogen implanted samples. The idea is to measure N implanted layer thicknesses using imaging methods such as optical microscopy, SEM and AFM. The following are the cross-sectional sample preparation steps:

i. Firstly, nitrogen implanted samples (disc-shaped) were cut into pieces by using wire electrical discharge machine (Mikron-Mak Kalıp, Organize Sanayi, Manisa).
ii. Secondly, cut pieces were bakalited by Struers LaboPress-3 (4 minutes heating at 150 °C and 4 minutes cooling).
iii. Lastly, bakalited cross-sectional samples were polished according to the polishing procedures described above.

The polishing was one of the difficult steps of this study in terms of time. Approximately, it was two hours for each sample. Afterwards, a cylindrical metal (with a diameter of 7 cm, a height of 3 cm and a weight of 0.5 kg) was used to hold the samples, as it can be seen from Figure 2.3. In this way, 3 or 5 samples depending on sample size were attached with double-stick tape on the sample holder and polished manually by hand. In this study, total polishing time was about 50 hours for 20 disc-shape materials and 40 cross-sectioned samples.

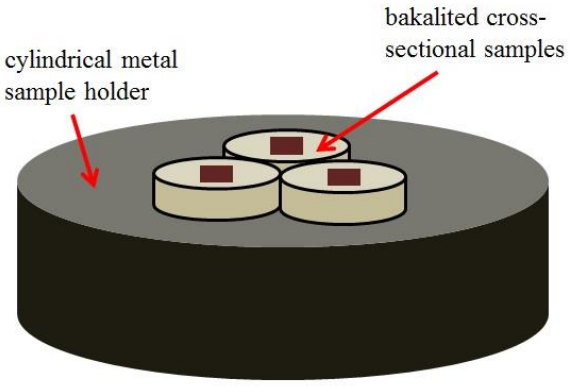

Figure 2.3. A cylindrical metal sample holder was used to polish bakalited cross-sectional samples as well as disc-shaped materials

2.3. Plasma Immersion Ion Implantation (PIII)

Surface modification by inserting nitrogen ions with plasma and ion implantation techniques offers improvements to the properties of metallic materials. These techniques include plasma nitriding, plasma immersion ion implantation (PIII) and conventional beam line ion implantation. The main differences between these techniques are the varying ion energy and the relative fraction of energetic ions, electrons, thermal atoms and ions impinging on the surface (Roth, 2002).

Plasma immersion ion implantation (PIII) is a surface modification technique, which positive ions are extracted from the plasma by applying negative high voltage pulses to the substrate and simultaneously accelerated towards the whole surface. Owing to the line-of-sight nature of conventional ion beam implantation, the cost of the large ion source required for modifying large components with complicated areas is prohibitive. Since PIII overcomes the line-of-sight restrictions of conventional ion beam implantation, it is a versatile method for complex shaped surfaces. Thus, PIII is very appealing for industrial applications, removes the line-of-sight and cost limitation of conventional ion beam implantation.

Different surface modification methods by inserting nitrogen ions into stainless steel and CoCr base alloys have been studied in the literature, including plasma nitriding (Baranowska, 2004; Öztürk et al., 2011; Öztürk et al., 2009), plasma immersion ion implantation (Lutz et al., 2011a; Manova et al., 2009) and conventional ion beam implantation (Blawert et al., 2001; Wei et al., 1996). A study (Wei et al., 1996) shows that the nitrogen concentration and depths of nitrogen-enriched layers changed depending on the process, in which the processes applied on the samples are at the same conditions. PIII method produces thick nitrogen-enriched layers (greater than 1 μm) at high concentrations (20-30 at.%) compared to plasma nitriding (layers less than 1 μm thick with low N content). Here, the difference between them is the energy of the ion beams. In PIII, the ions are highly energetic ranging between 1 keV and 100 keV, whereas the ion energies are in the range of 10-100 eV in plasma nitriding.

Sputtering is essential for nitriding/implantation of materials like stainless steel and CoCr alloys. Sputtering removes the native oxide layer from the substrate at the beginning of the process. In PIII, the surface is sputtered due to higher ion beam energies compared to the plasma nitriding process. During the PIII process, pure N_2

nitrogen gas is used. On the other hand, Ar and H_2 are used before the plasma nitriding to remove native oxide layer and sometimes N_2+H_2 mixtures are applied to keep the surface layer oxide free.

2.3.1. PIII Setup

In this study, nitrogen was applied on the investigated materials by tecnique of plasma immersion ion implantation (PIII). Schematic experimental setup of the PIII system used in this work can be seen in Figure 2.4. The PIII experiments were carried out using an electron cyclotron resonance (ECR) plasma source in an Ultra-High Vacuum (UHV) chamber by Dr. Stephan Mändle's research group in Leibniz Institute of Surface Modification in Leipzig, Germany. The ECR plasma source operating with frequency of 2.45 GHz at a power of 150 W generated plasma with an resulting electron temperature and plasma density of 1.3 eV and 1.6×10^{10} cm^{-3}, respectively. At a nitrogen gas flow of 150 sccm the resulting pressure during the experiments was 0.53 Pa. Negative high voltage of 10 kV with a pulse length of 15 μs was applied to the samples which were mounted on a sample holder.

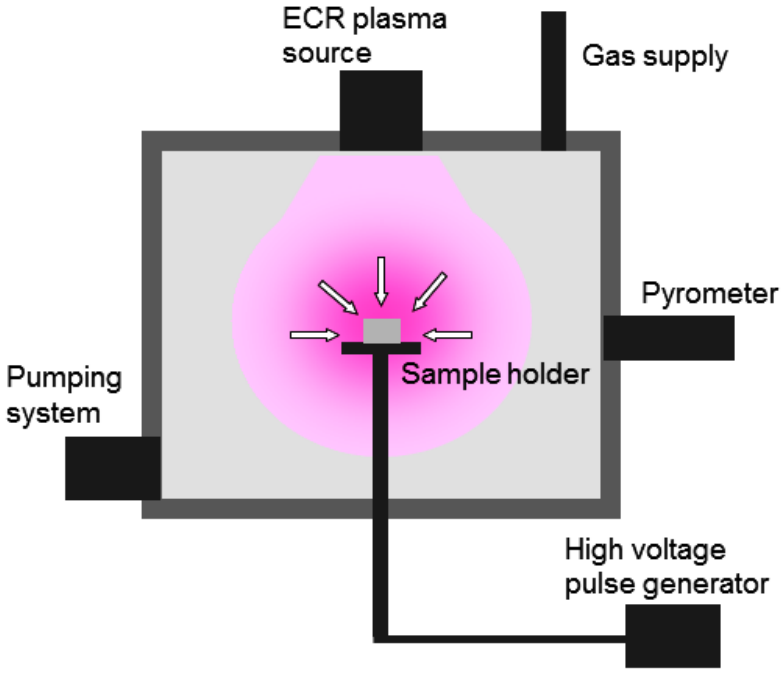

Figure 2.4. A schematic diagram of PIII system

The nitrogen implantations were performed in the temperature range between 300 and 550 °C for fixed processing time of 1 hour. The temperature variation was achieved by changing the pulse frequency from 0.25 kHz to 4.5 kHz. During the implantation, external heating was switched off and the samples were heated only by the impinging ions. The temperature was monitored using an IR pyrometer on the surface of sample holder.

2.4. Experimental Techniques

Structural, compositional, topographical and magnetic characterization of polished and nitrogen implanted samples were carried out by the following techniques:

- θ/2θ (Bragg-Branteno) X-Ray Diffraction (XRD)
- Grazing incidence X-Ray Diffraction (GIXRD)
- Atomic Force Microscopy (AFM)
- Magnetic Force Microscopy (MFM)
- Scanning Electron Microscopy (SEM) and Energy Dispersive X-Ray (EDX)
- Cross-Sectional Scanning Electron Microscopy (CS-SEM)
- Secondary Ion Mass Spectroscopy (SIMS)

Phase analysis was investigated with X-ray diffraction in both θ/2θ geometry and grazing incident (GIXRD) mode. Topography was studied by scanning electron microscopy (SEM) and atomic force microscopy (AFM). Surface roughness was measured by atomic force microscopy (AFM). Elemental compositions were estimated with EDX. The N implanted layer thicknesses were measured by SEM on the polished sample cross-sections. Nitrogen depth profiles were obtained from SIMS.

Additionally, hardness measurements on the sample surfaces were performed with Dynamic Nanoindentation Experiment using a Berkovich tip.

2.4.1. X-Ray Diffraction (XRD)

X-ray diffraction can be used to identify some physical and chemical information such as composition, crystal structure and layer thickness determination. Basically, the information is obtained from the diffraction of x-rays by a crystalline material, which is a process of scattering of the beam by the electrons associated with the atoms in any crystal.

Figure 2.5 indicates basic components of XRD system in this study. The following gives a brief explanation for these components.

- Ceramic X-ray tube: the source of X-rays.
- Incident beam slits: to control the axial width of the incident beam.
- X-ray mirror: to maintain parallel incident beams on the sample surface.

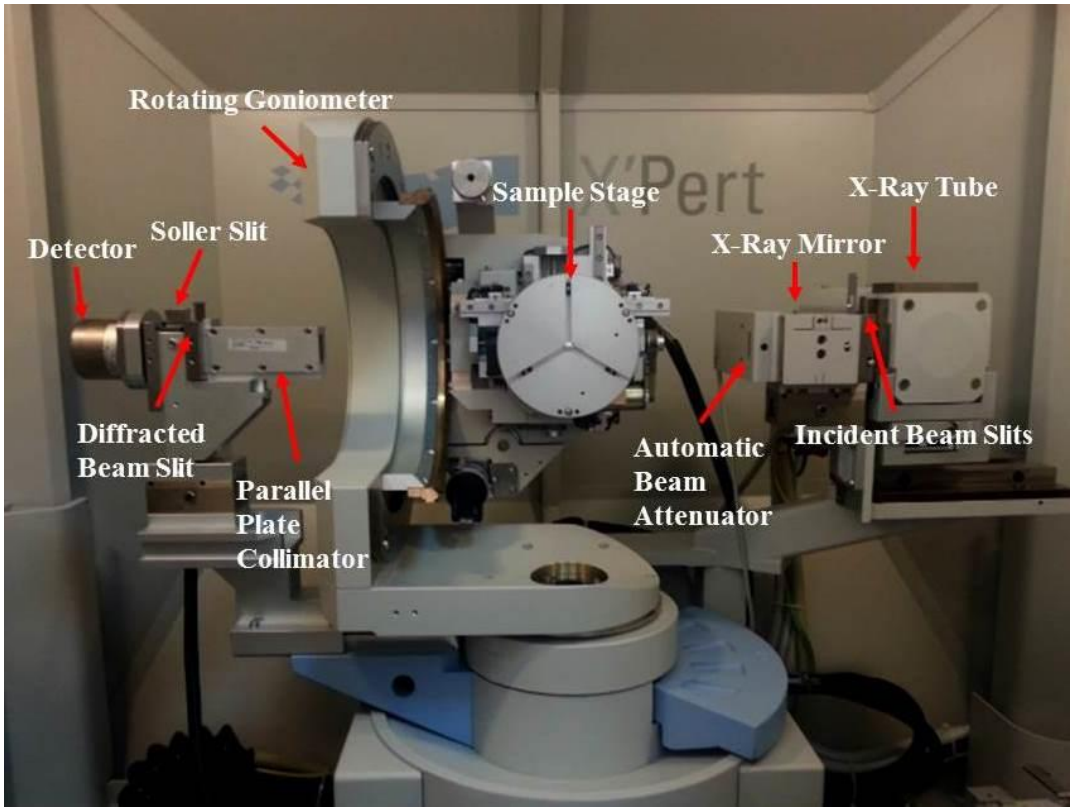

Figure 2.5. This figure illustrates Thin Film Philips X'Pert Pro MRD System which was used for XRD experiments in this study, which was facilitated by Physics Department in Izmir Institute of Technology

- Automatic beam attenuator: an absorber which is placed in the x-ray beam to reduce its intensity by a specific factor. Automatic Beam Attenuator contains a Ni foil that can be set to be switched in and out of the x-ray beam either at a fixed angle or at a fixed intensity.
- Goniometer: a platform that holds and moves the sample and detector.
- Parallel plate collimator: consists of a set of parallel plates perpendicular to the diffraction plane. The distance between the plates defines the acceptance angle of the collimator. The collimator in the X-ray has equatorial acceptance of 0.27^{o}.
- Solar slit: in order to parallel the diffracted beams arriving to the detector.
- Diffracted beam slits: to control the amount of the diffracted X-ray beam that is accepted by the detector. This slit is mainly used for reflectivity measurements to enhance the resolution at very low 2θ angles (less than 4^{o}).
- Proportional detector: counts the number of X-rays scattered by the sample.

In this study, two different geometries: (1) Bragg-Brentano (θ/2θ) and (2) grazing incidence x-ray diffraction (GIXRD) mode were utilized on samples. During all XRD measurements, X-ray tube voltage and current used were 45.0 kV and 40 mA, respectively. XRD was performed using Cu-Kα radiation with the wavelength 1.5406 Å from x-ray tube. The experimental data from XRD was collected with computer-controlled system. The resultant XRD spectrum is in the form of the scattered X-ray intensity (counts) versus 2θ (degrees). The XRD data were evaluated to obtain accurate peak positions and to find lattice parameter using the available software (X'Pert HighScore and PeakFit v 4.11). Here, XRD were used to identify crystal structure, expansion of cells, crystallite sizes.

2.4.1.1. Bragg-Brentano Method

This method is also called as θ/2θ XRD method. The basic geometry of Bragg-Brentano XRD was illustrated in Figure 2.6.

In this configuration (also, shown in Figure 2.7), both the sample and the detector move step by step during the measurement. The X-ray tube is fixed in the experiment while the sample and the detector are rotated through a goniometer. The sample moves by the angle θ while the detector simultaneously moves by the angle 2θ.

During the experiment, since the incident and diffracted X-rays make the same angle to the sample surface, structural information is obtained from only (hkl) planes parallel to the surface, not the others. There is a disadvantage of this method that the effective depth probed by the incident beam always changes during the scan due to the change in the angle of the incident beam. Due to change in the incident beam angle, the effective depth probed by the beam is increased depending on increasing incident beam angle. This property may cause some misinterpretation if it is not taken notice on examining for example, a material having layered-structure.

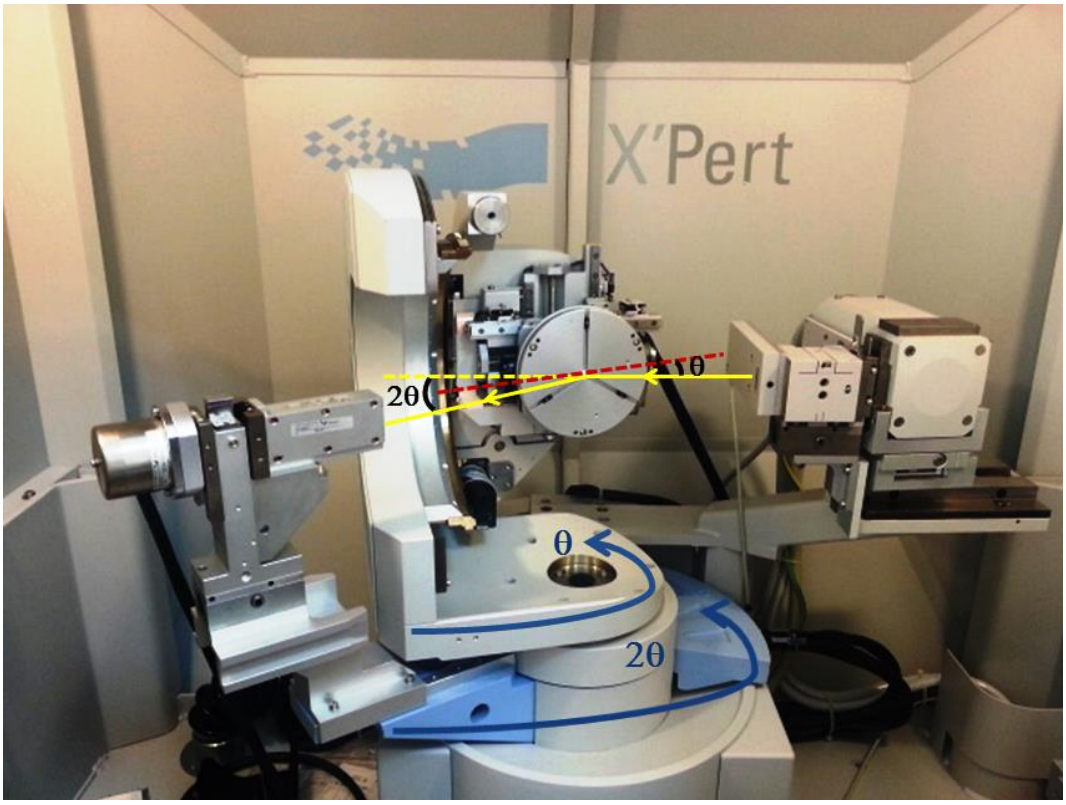

Figure 2.6. Schematic diagram of XRD system in Bragg-Brentano geometry, which belongs to thin film XRD system in Physics Department of IZTECH

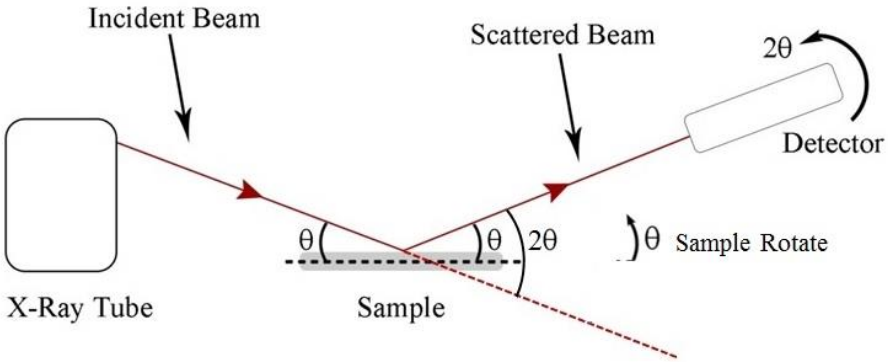

Figure 2.7. Basic geometry of Bragg-Brentano method

When there is constructive interference from X-rays scattered by the atomic planes in a crystal, a diffraction peak is observed. A diffraction pattern is obtained by measuring the intensity of scattered X-ray beam as a function of scattering angle. The condition for constructive interference from planes with spacing d is given by Bragg's law. When the scattered x-ray beams satisfy the Bragg's law in Equation 2.1, very strong intensities known as Bragg peaks are indicated in the diffraction pattern. Also, obtained accurate peak positions (2θ) from the XRD result are used in order to calculate the lattice constant in equations below. The equation 2.2 is valid for cubic structures.

$$2d \sin\theta = n\lambda \tag{2.1}$$

$$d = \frac{a}{(h^2+k^2+l^2)^{1/2}} \tag{2.2}$$

In above equations,

d : distance between atomic planes (hkl)

θ : X-ray diffraction angles from different crystal planes

n : order of diffraction

λ : wavelength of Cu-Kα x-rays

h, k, l : miller indices

a : lattice constant of crystal

In our experiments, XRD measurements of nitrogen implanted samples as well as substrate materials were carried out by using two x-ray diffraction systems: one is powder diffractometer system (Philips X-Pert Pro system in Center for Materials Research) and the other is Philips X'Pert Pro MRD System Thin Film X-Ray Diffraction system (shown in Figure 2.5). In the first system, the XRD experiments were made with a Bragg-Brentano (θ/2θ) geometry. The 2θ range for each specimen was between 30 to 100 degrees, which gives a scan time of about 10 minutes for scan step size and time per step used in this experiment (0.0334° and 19.685 s, respectively). The second system was used to obtain higher quality of the XRD patterns compared to powder diffractometer system. The XRD data was provided by scanning at long time of about 1 hour for each specimen. XRD in θ/2θ geometry were performed on nitrogen implanted samples in the 2θ=35°-55° region. This scan range allows the observation of the region of the (111) and (200) peaks, which are most revealing compared to the higher (hkl) data range.

2.4.1.2. Grazing Incidence X-Ray Method

Grazing Incidence X-ray diffraction (GIXRD) was utilized to obtain further information about near-surface crystal structures on our nitrogen implanted samples. This method generally is used at small incident angles (e.g., 0.25°, 0.5° and 1°) on the surface providing information from quite thin layers. GIXRD data was obtained using the thin film x-ray diffraction system in Physics Department of IZTECH.

Figure 2.8 shows the basic geometry of the GIXRD system used in this work. In this configuration (also, illustrated in Figure 2.9), the incident X-ray beam is fixed to a predetermined value on the sample and only the detector rotates 2θ degrees. Being different from the XRD in Bragg-Brentano geometry, GIXRD facilitates diffraction from the planes which are not parallel to the sample surface.

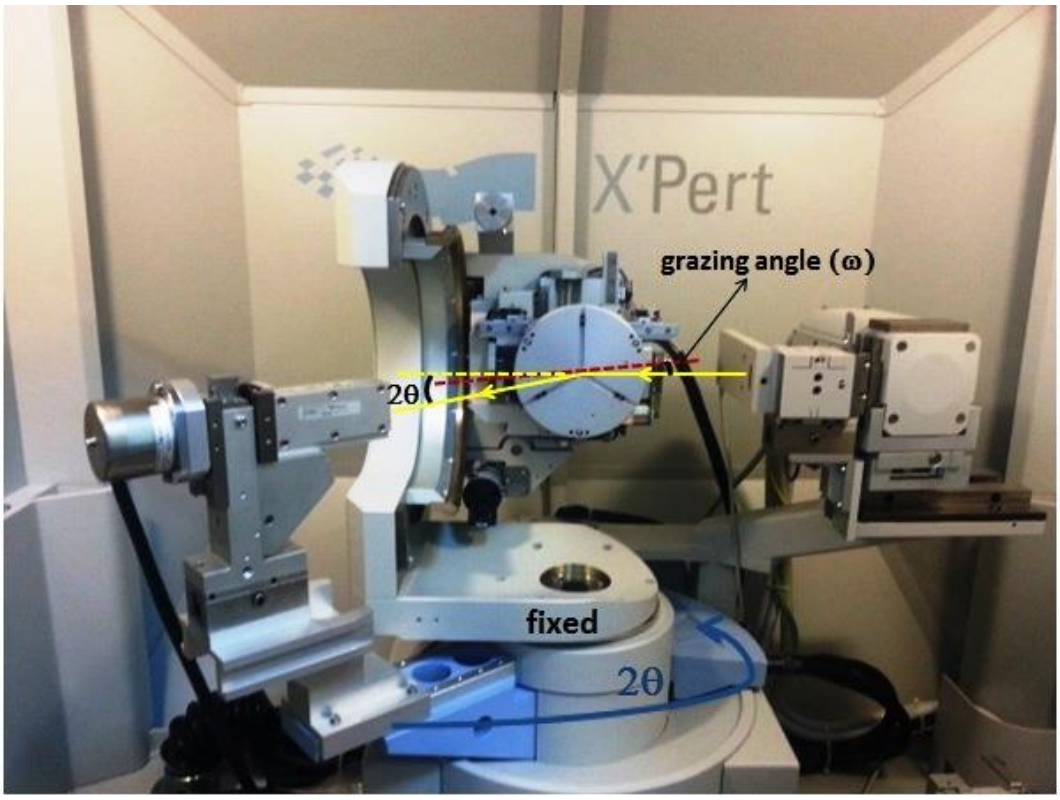

Figure 2.8. Schematic diagram of XRD system during GIXRD measurements, which belongs to Thin Film XRD system in Physics Department of IZTECH

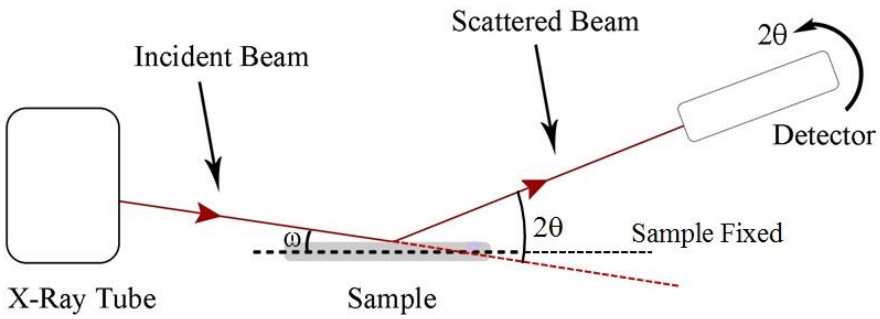

Figure 2.9. Basic geometry of GIXRD mode

In this method, a study (Öztürk et al., 2006) in literature was estimated X-ray penetration depth for nitrogen implanted CoCrMo alloy. There, when the incident grazing angles are 0.5° and 1°, the penetration dephts of X-ray were found to be about 34 nm and 68 nm, respectively. Thus, only by changing the angle of incident X-ray beam incoming on the sample, this method can provide the information layer by layer.

In this study, the angles (ω) of the incident X-ray beam for examination of polished 304 SS were fixed at 0.5°, 1°, 2°, 5°, 10°, respectively in order to obtain further information on top surface (~ 50-100 nm) of the sample. Afterwards, GIXRD measurements of N implanted samples were carried out to identify phase formation with respect the depht of N implanted layer at grazing angles of 0.5°, 1°, 2°, 3°, 4°, 5°, 10°. The scanning range (2θ) was 35°-55°.

2.4.2. Atomic Force Microscopy (AFM)

Atomic force microscopy (AFM) was used to investigate surface roughness and topography (i.e., grain size variations and surface defects) of the polished and nitrogen implanted samples. As can be seen from Figure 2.10, AFM uses a sharp tip mounted on a cantilever usually made from silicon or silicon nitride, with a very low spring constant (~ 0.1 – 1 N/m).

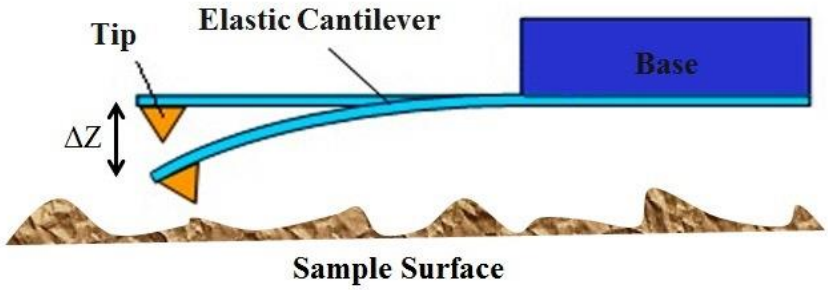

Figure 2.10. A schematic of AFM tip and cantilever

The AFM working principle is described as follows: during AFM measurements, the probe is a tip on the end of a cantilever which bends in response to the interactive force between the tip and the sample surface. The interactive force can be attractive or repulsive force depending on distance between tip and sample. In the case of interaction, this force is in ranging from nN to μN. As shown in Figure 2.11, first of all, when the tip is far away from the sample surface, the cantilever feels no any force from the sample surface. As the tip approaches the sample surface, the cantilever deflects towards the sample due to attractive Van der Walls force (long range). As the

tip gets closer to the sample, this attraction increases and rapidly the tip touches on the sample surface. At this time, since the repulsive coloumb forces (short range) become dominant at very small separation (~ 0.3 nm), instantly the tip into contact with surface deflects up to sample. When the tip moves above the surface, the tip deflection will reflect a change in topografy. Therefore, by measuring the cantilever deflections, the surface topography can be obtained. In addition, this deflection occurs when dF/dz exceeds the cantilever spring constant. According to the Hooke's Law, deflection of the cantilever can be written as;

$$F = k\Delta Z \tag{2.3}$$

Where the deflection of cantilever ΔZ is determined by the acting force F and spring constant k.

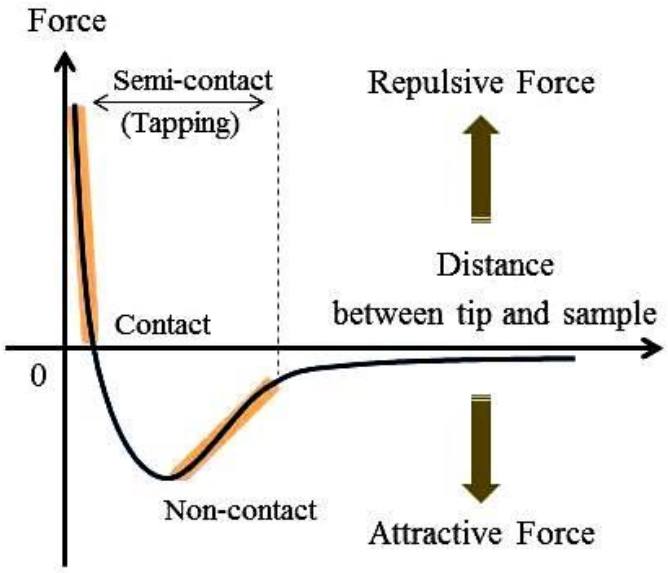

Figure 2.11. Interactive forces versus distance

In this study, AFM measurements were performed in semi-contact (tapping) mode to obtain surface morphology and roughness of the polished and nitrogen implanted specimens by using AFM (Solver Pro 7 from NT-MDT, Russia, which was situated Physics Department in Izmir Institute of Technology). In the tapping mode, the cantilever is approached to the surface with low oscillation and the tip scans the surface

in semi contact. Namely, the tip is not mechanical contact with the surface during the scan. During all the scans, antimony (n)-doped Si cantilever with elastic constant of 20-80 N/m, a resonans frequency of 272-334 kHz (TESP from Veeco) was used. Surface topography measurements on all the samples were performed at least three different regions. Typical scan area was 30 μm x 30 μm.

2.4.2.1. Roughness Measurements

Surface roughness measurements were performed on both substrates and nitrogen implanted samples by using AFM in tapping mode. During nitrogen PIII process sample surfaces are subjected to sputtering which may be detrimental to the surface quality. The aim of the measurements was to get the information about sputtering rates and their effects on the samples of PIII at each processing temperature. The roughness values were obtained from three different regions. And, average roughness values were calculated for all samples. The average roughness (Ra) makes no distinction between peaks and valley and gives the deviation in surface height. On the other hand, root-mean-square (RMS) roughness makes standart deviation of all peaks in a selected region. Therefore, it is expected that RMS roughness values is higher than average roughness.

2.4.3. Magnetic Force Microscopy (MFM)

In this study, the magnetic structures of the sample surfaces were imaged with a scanning probe microscopy (Veeco, Dimension 3100) in magnetic force mode (MFM). In this mode, the probe is a tip coated with a ferromagnetic film (e.g., CoCr or FeNi) gives an image showing the variation in the magnetic force between the magnetized probe and magnetic stray field originating from the sample surface.

Magnetic force microscopy (MFM) is a powerful technique to image domain structures of different magnetic materials. MFM is an extension of atomic force microscopy. During the MFM measurements, topographical image and magnetic data can be simultaneously measured using the two-pass technique, as illustrated in Figure 2.12. In the two-pass technique, the first pass in the semi-contact (tapping) mode of operation is a standart AFM trace that maps out the surface topography along the

surface. Then, in the second pass (lift mode), the magnetic probe tip is lifted above the surface of sample at a constant height in order to minimize the effect of the van der Waals forces (ranging less than 20 nm). However, during the lift height (range 30-300 nm) the tip is more sensitive to far field magnetic force than short range van der Waals force (Wozniak et al., 2005). In literature, a study (Neves and Andrade, 1999) is said that magnetic interactions are between 5 and 300 nm in stainless steel. During the lift scan, the probe is moved over the surface along the same line scanning the surface topography. As a result of the interaction between magnetic coated tip and magnetic sample, the infulence of magnetic forces is monitored by observing changes in resonans frequency of the tip, the results are detected by laser/photo-detector.

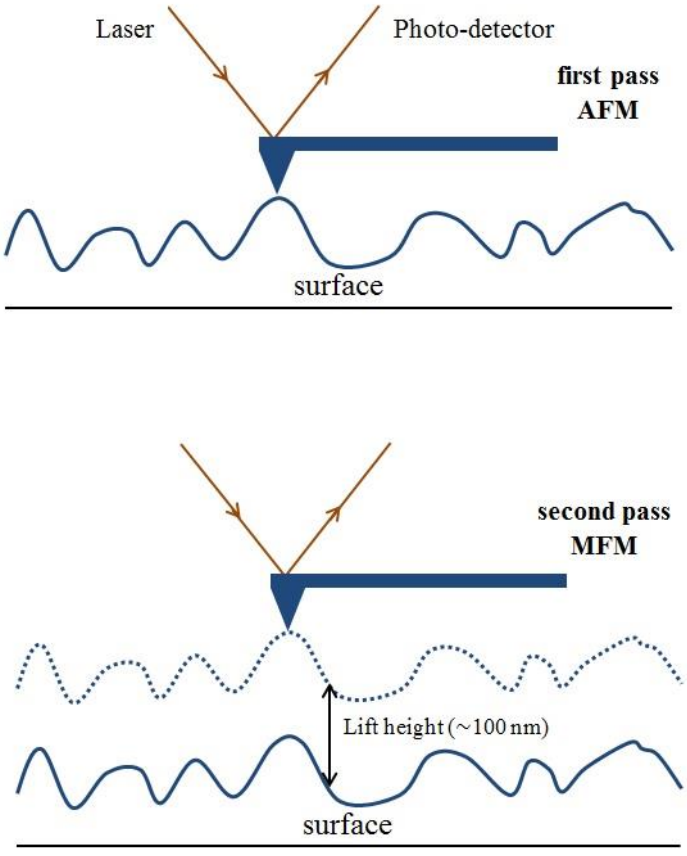

Figure 2.12. The first pass, for topography; the second pass, for the magnetic data

Figure 2.13 shows the interaction between the magnetic tip and sample. During the MFM measurements, the cantilever is deflected by the magnetic interaction force F between the ferromagnetic tip and the stray field emanating from the sample surface.

$$F = (m.\nabla)\, H_s \tag{2.4}$$

Where m is the magnetic moment of the tip and H_s is the magnetic stray field of the sample. Since the magnetization of the tip is parallel to its axis, only the stray field component perpendicular to the sample surface is detected. Thus, the for F_z acting in the z-direction is

$$F_z = (m.\nabla)\, Hs \approx m_z \frac{\partial Hs}{\partial z} \tag{2.5}$$

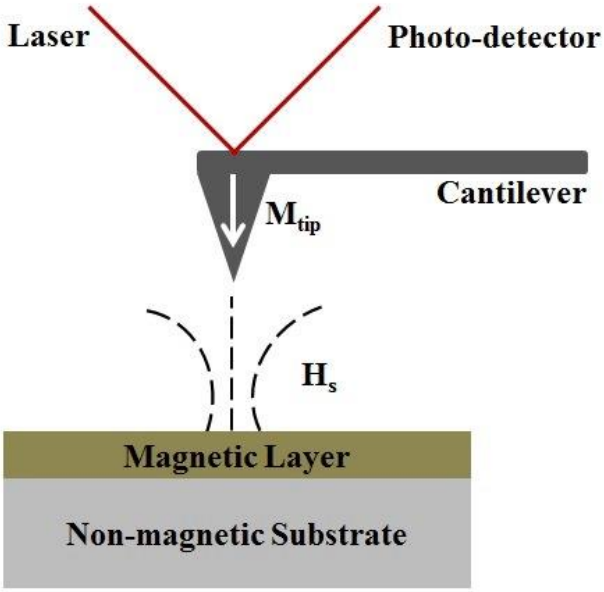

Figure 2.13. Interaction between the magnetic tip and sample

In our experiment, the magnetic structures of the sample surfaces were imaged with a (Veeco, Dimension 3100) magnetic fore microscopy and a CoCr coated tip (the MESP type supplied by Bruker company) with radius of 40 nm and resonant frequency of 60-100 kHz was used. A lift hight of 60-300 nm was chosen for all MFM measurements presented in this study. Before MFM analysis, magnetic tips were remagnetised by strong stray fields above surfaces of bulk permanent magnet sample. Additionally, MFM analysis of the magnetic recording tape was performed to ensure the status of the magnetic tip prior to each measurement. As can be seen from Figure 2.14, the result indicates an image, which contains information about both the topograph and

the magnetic properties of a surface. While the left image is the surface topography, the right image is of magnetic stray field. The dark (light) stripes in the right image indicate domains with a relatively upward (downward) magnetization component. These stripes refer the individual bits recorded on the magnetic tape (Fe_2O_3).

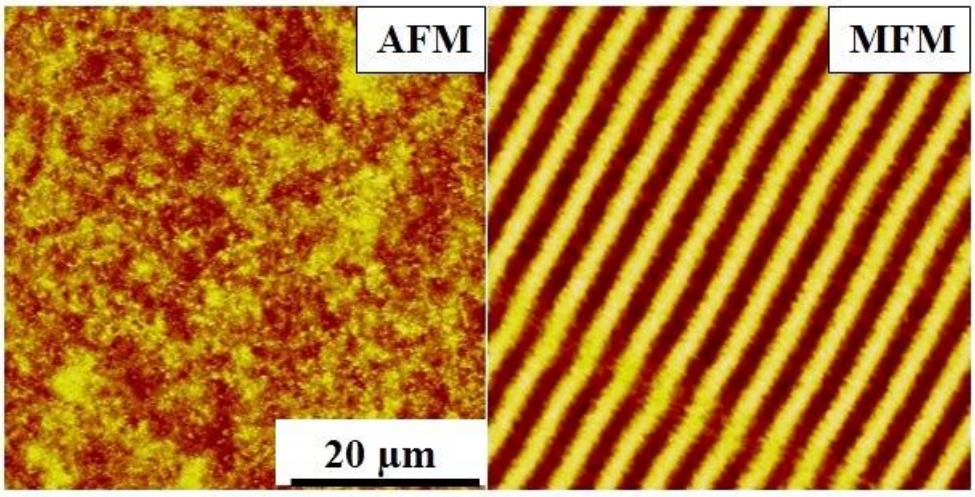

Figure 2.14. Image (left) is a topographical image of the surface of magnetic recording tape in tapping mode. Image (right) is a MFM image of the same surface

2.4.4. Scanning Electron Microscopy (SEM)

A technique to obtain elemental composition and to visualize surface structures is scanning electron microscopy (SEM). As shown from Figure 2.15, when the primary electron beams ranging from a few hundred eV up to 30 keV hit onto the sample surface, electron signals are emitted. The signals most commonly used are the secondary electrons (SE), the back-scattered electrons (BSE) and X-rays. These signals are collected by different detectors in relation with emitted beams. When a primary electron beam interacts with electrons of an atom in an inelastic collision, most of the energy is transferred to the electrons of the sample. In case of that, the energy of emitted electrons have less than about 50 eV and the emitted electrons in the surface near regions with a few nm exit the surface. It is refered as secondary electrons (SE). On the other hand, back-scattered electrons are obtained from the more deeper regions (from a few nm to 100 nm) of the sample in consequence of elastically interactions between primary electron beams and the nucleus of atom. It is known that backscattered

electrons exit the sample with an energy greater than 50 eV. These secondary and backscattered electrons are used for surface imaging.

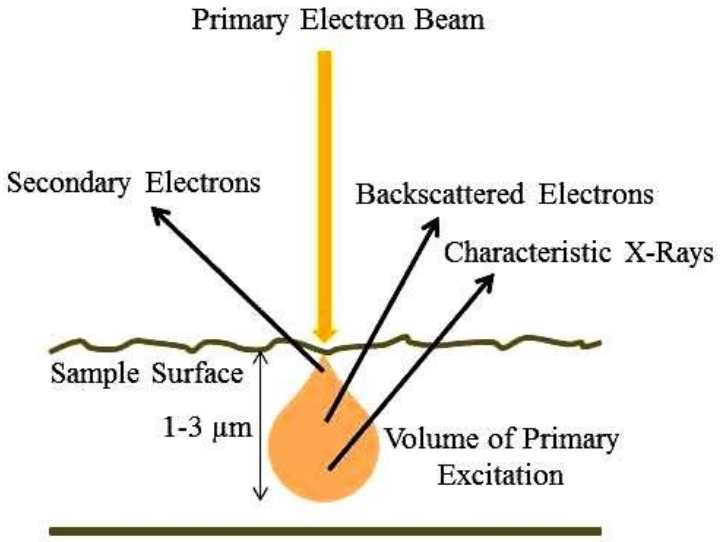

Figure 2.15. Electron beam interaction with material during SEM analysis

In this study, scanning electron microscopy was used to obtain topographical information (i.e., elemental composition, surface image) on the surfaces of nitrogen implanted samples as well as substrates. The SEM images investigated in this work were taken by Center for Materials Research (IZTECH MAM). The images were obtained using backscattered electron detector (BSED) in various magnifications from 2500X to 40000X at 20 kV applied beam voltage.

2.4.4.1. Energy Dispersive X-Ray (EDX)

As can be seen the figure above, when the incident primary electron beams strike on the sample, the primary electron beams generate X-rays from the atoms of the sample as well as scattered electrons and backscattered electrons. These X-rays have a characteristic energy, which is unique to the element which produced it. Because of these unique characteristics, X-rays can be used to provide quantitative information about the elements present at a selected region on the sample. The information is collected with energy-dispersive X-ray (EDX) detector in SEM within a depth about 1-3 µm.

The EDX was used to determine the elemental composition on the surfaces of nitrogen implanted samples as well as substrates. The compositions on randomly selected regions of specimens were taken with SEM in EDX mode. The EDX results provided the composition ratio in units of both weight percent and atomic percent.

2.4.4.2. Cross-Sectional Scanning Electron Microscopy (CS-SEM)

In this study, cross-sectional SEM analysis was performed to measure thichnesses of N implanted layers on the polished sample cross-sections. Before analyzing by CS-SEM, all cross-sectional specimens were polished by polishing procedure as mentioned earlier. During measurements, backscattered electron detector (BSED) was used to obtain cross-sectional images. BSE images were taken at various magnifications ranging from 10000X to 50000X by changing primary incident beam voltages of 15 kV and 20 kV.

2.4.5. Secondary Ion Mass Spectroscopy (SIMS)

Secondary ion mass spectrometry (SIMS) is a technique that used to analyze the elemental composition by sputtering the surface, with ppm sensitivities and lateral (x,y) resolution between 50 nm and 2 μm (Brundle et al., 1992). As can be seen from Figure 2.16, primary ion beams (i.e., oxygen, argon) having energies between 1 and 20 keV is focused on the surface. The energy is transferred to atoms in the surface through collision and generates secondary particles by sputtering. As a result of that, a mixing zone consisting of primary ions and displaced atoms from the sample occurs into sample. The depth of the mixing zone depends on the energy, angle of incidence, mass of the primary ions and sample. During the SIMS analysis, the primary ion beam continuously sputters the sample and removes material from the surface. And, the mixing zone is increased into the sample as a function of the sputtering time. The sputtered ions (secondary ions) are extracted and accelerated towards the detector by an electric field. By measuring their mass-to-charge ratio and their time of flight between the sample and detector, it is possible to estimate the elemental composition of the sample.

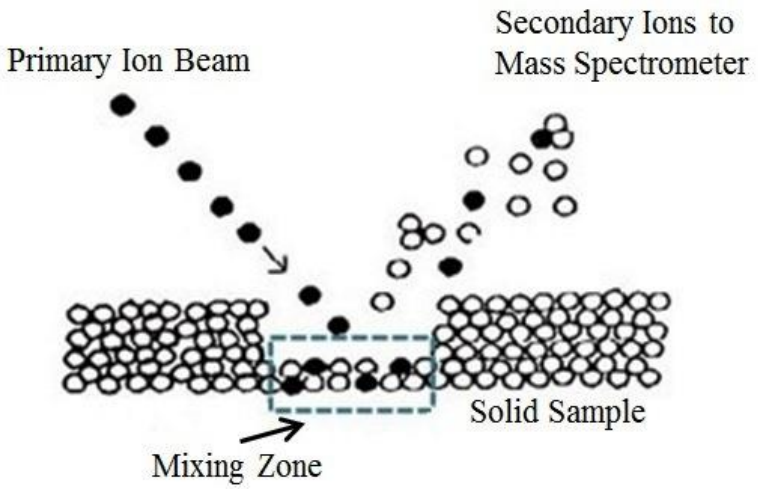

Figure 2.16. The sputtering effect during SIMS

In our work, SIMS measurements were performed using a 15 keV Ga^+ beams and a 2 keV O_2^+ beams for sputtering, respectively. The aim of the measurements was to obtain the nitrogen depth distribution profiles of the nitrogen implanted samples.

2.4.6. Surface Hardness Measurements

The objective of the measurements was to investigate the hardness of nitrogen implanted surfaces compared to substrate samples. The surface hardness values of the samples were obtained as a function of the indentation depth.

The nanoindentation technique was developed in the mid-1970s to estimate the hardness of small volumes of sample (Poon et al., 2008). During the measurements, a special tip is pressed into the sample with increasing loads. The resulting hardness value can be calculated using the contact area between tip and sample, the applied load as well as the penetration depth.

The hardness measurements presented in this study were carried out using a nanoindentation setup with a Berkovich tip, which has a three-sided pyramid geometry, by Dr. Stephan Mändle's research group in Leibniz Institute of Surface Modification in Leipzig, Germany. The loads applied on the nitrogen implanted surfaces were 20 mN and 50 mN, respectively. For each indentation, averaging over 10 independent measurements technique was taken.

CHAPTER 3

PHASE FORMATION

In this chapter, phase analysis of nitrogen implanted samples as well as the substrate alloys will be explained by X-ray diffraction in both θ/2θ geometry and grazing incidence (GIXRD) mode.

3.1. Polished 304 SS and CoCrMo Substrate Alloys

Figure 3.1 presents the XRD patterns of the substrate alloys between the angles 30° and 100°. As can be seen from the substrate XRD patterns, both materials have mainly fcc structure, which are labelled as γ(hkl) in Figure 3.1 and a large majority of the fcc grains are in [111] direction.

The polished CoCrMo alloy structure consists of a mixture of predominant fcc lattice structure [i.e., fcc γ-(Co,Cr,Mo)] and weak hcp crystal structure [hcp ε-(Co,Cr,Mo)]. Literature indicates that the hcp ε phase is located, as thin bands, within the fcc γ matrix. The polished 304 SS alloy has mainly fcc structure [i.e., fcc γ-(Fe,Cr,Ni) phase]. The XRD data for the polished 304 SS also indicates a weak shoulder peak just to the right of fcc γ(111) peak. This peak (labelled as α') is attributed to strain-induced martensite phase due to polishing. GIXRD analysis of this sample clearly confirms this finding. Since α' is to the right of the γ(111) peak, the GIXRD analysis were performed in the range between the angles 35° and 55°. As can be clearly seen from Figure 3.2, at the lowest grazing angle (ω=0.5°), martensite peak is much more intense. The intensity of martensite peak decreases as a function of increasing grazing incidence angle. As stated in the experimental method section, the penetration depth of x-ray changes with incident angle on sample surface. At the grazing angle of 0,5° and 1°, penetration depth of x-rays ($x \sim \sin\omega/\mu$) is calculated as ~41 nm, ~82 nm, respectively (linear mass absorption coefficient (μ) for 304 SS used in this study is 2116 cm^{-1}). According to the results, it can be said that martensite phase is formed on the top surface layer (~ 50 – 100 nm).

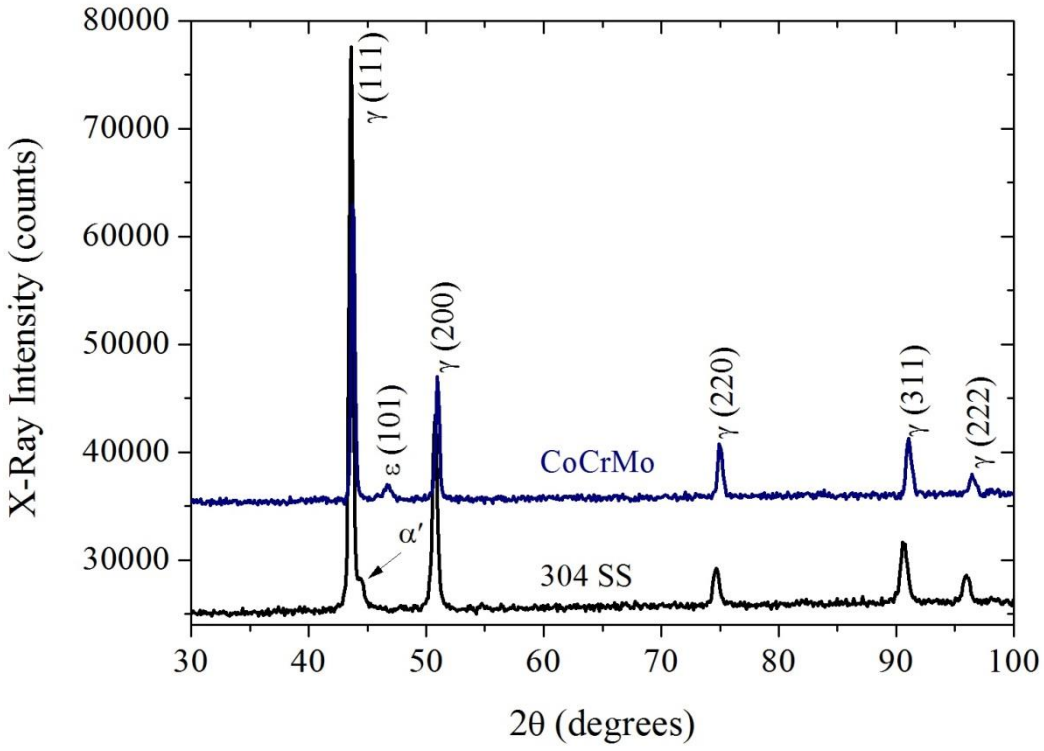

Figure 3.1. XRD patterns for the substrate 304 SS and CoCrMo alloys

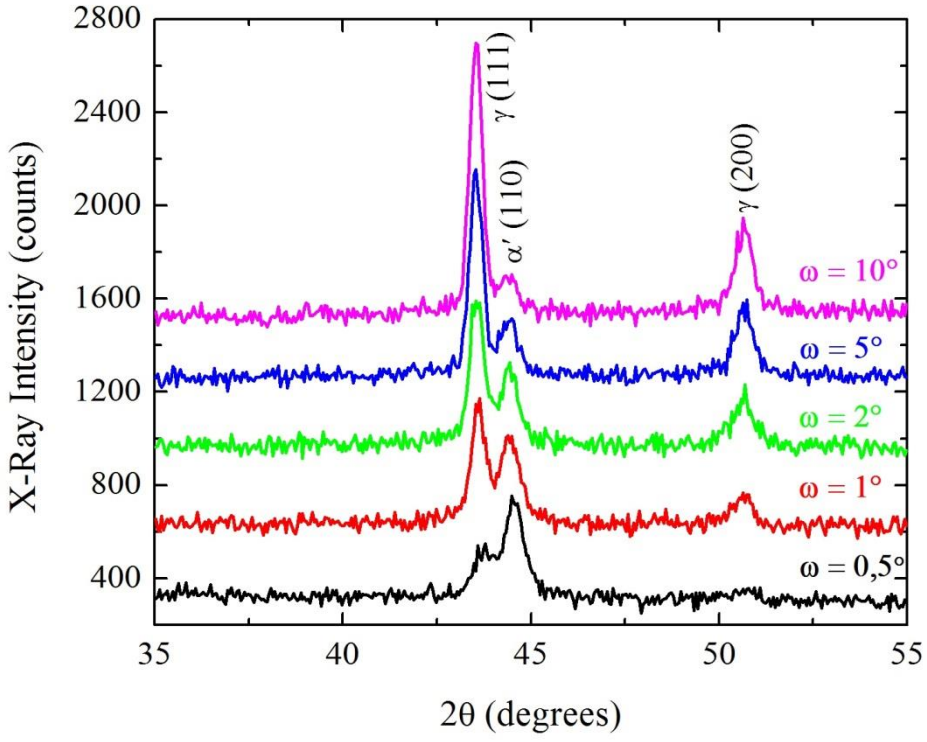

Figure 3.2. GIXRD patterns of the substrate 304 SS at different grazing angles

3.2. Nitrogen Implanted 304 SS and CoCrMo Alloys

Here, XRD was carried out on 304 SS and CoCrMo samples that were nitrogen implanted at temperatures ranging from 300 to 550 °C for a fixed processing time of one hour. The XRD analyses of the nitrogen implanted samples were performed at 2θ degrees between the angles 35° and 55°. This scan range allows the observation of the region of the (111) and (200) peaks, which are most revealing compared to the higher (hkl) data range.

To understand better the phase distribution with depth in the N implanted layers, grazing incidence X-ray diffraction (GIXRD) of the N implanted samples was carried out at the incident angles of ω=0.5, 1, 2, 3, 4, 5 and 10 degrees, respectively. GIXRD analysis were also performed in the 2θ=35°-55° region. Note that the square-root of the intensity is plotted to reveal more clearly the weaker peaks.

3.2.1. θ/2θ XRD Results of Nitrogen Implanted 304 SS

Figure 3.3 shows the XRD patterns of the nitrogen implanted 304 SS at various processing temperatures. As can be seen from Figure 3.3, at lowest processing temperature (300 °C), in addition to the substrate γ peaks, XRD data indicates clearly the formation of the expanded austenite phase, labelled as γ_N(hkl). This phase has the same lattice structure with fcc substrate but in this phase, nitrogen atoms enter into octahedral sites. At higher processing temperature (350 °C), as seen from the XRD data, there is only expanded phase for this alloy and almost no substrate peaks. This indicates that the expanded layer of this alloy is quite thick. In addition, the expanded phase peaks corresponding to this sample are shifted to much lower angles. It means that there is more lattice expansion and much higher nitrogen content in this sample compared to N implanted sample at 300 °C. At the processing temperature of 400 °C, the data shows clearly the formation of a new phase, labelled as CrN, in addition to expanded phase. The data suggests that the expanded phase decomposes into formation of CrN. This sample also has the expanded phase but its peaks are weaker and shifted to higher angles compared to the samples prepared at 300 and 350 °C. At the treatment temperature, 450 °C, the expanded phase peak intensities decreases, furthermore, decomposition process continues not only the results into CrN but also bcc α-phase [α-

(Fe, Ni)]. At highest processing temperature (550 °C), the XRD pattern is mainly composed of fcc CrN and bcc α-(Fe, Ni) phase structures.

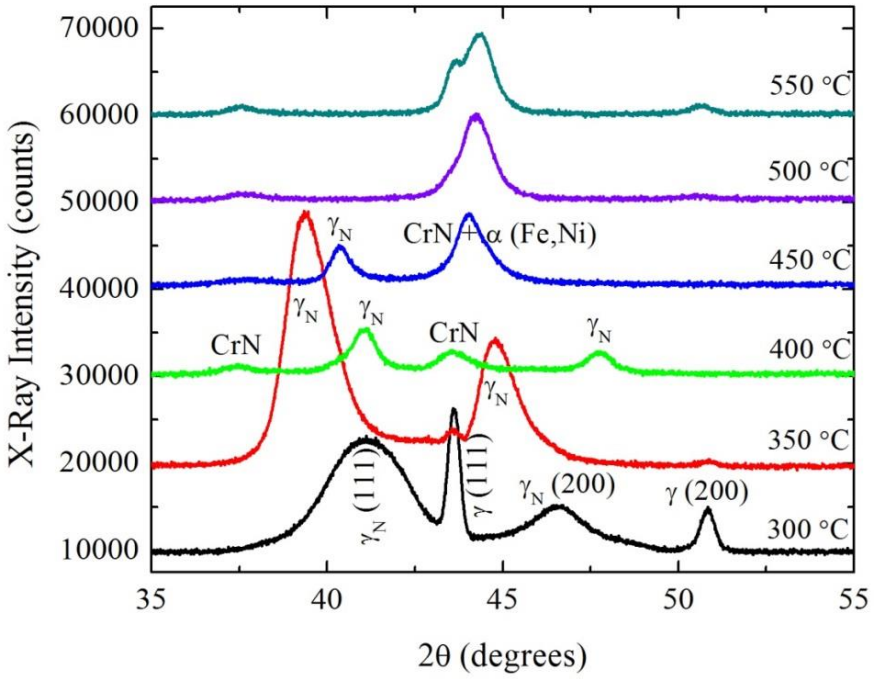

Figure 3.3. XRD data of nitrogen implanted 304 SS samples at different PIII treatment temperatures

The findings here are consistent with previous studies (Collins et al., 1995; Lutz et al., 2008a; Lutz et al., 2011b) in literature. These investigations were performed on similar stainless steels using nitrogen PIII process.

3.2.2. GIXRD Results of Nitrogen Implanted 304 SS

The GIXRD results for N implanted 304 SS samples are shown as a function of implantation temperature in Figure 3.4. In each graph of this figure, top data belongs to the Bragg-Brentano ($\theta/2\theta$) XRD result, which was already discussed before. And the rest are grazing incidence (GIXRD) data. The GIXRD data at the processing temperature 300 °C show that at the lowest angle (0.5°) the N implanted layer has the substrate peaks in addition to γ_N peaks. The GIXRD results at higher incident angles indicate more and more contribution coming from the substrate phase and also increasing γ_N phase. The GIXRD results for N implanted sample at 350 °C show that, at all grazing angles, there are no substrate peaks. Even at highest grazing angle of 10°, the substrate peaks does not observed, where the penetration depth of X-ray is about 4 μm. It suggests that the top layer in this sample only consists of γ_N phase. This finding is quite agreement with the results obtained from cross-sectional SEM and SIMS (these results will be explained in later sections). The GIXRD data for 400 °C clearly indicates that at the lowest grazing angle (0.5°) there are two phases: CrN and γ_N. The intensity of these peaks is small since the penetration depth and volume at 0.5° is less compared to higher grazing angles. In addition, CrN and γ_N phase intensities are increasing as a function of grazing angle. It means that top layer is composed of CrN precipitates and γ_N. The GIXRD data at the processing temperature of 450 °C show that at the lowest angles (0.5° - 1°), the top layer has only CrN and bcc α-(Fe, Ni) phase. As one increases further grazing incidence, it seems there is also contribution γ_N phase. Further decomposition of expanded phase is also evidenced by the grazing incidence data at 450 °C. The GIXRD results for N implanted sample at 500 °C clearly show that the top surface layer is composed of CrN and bcc α- (Fe, Ni). The data at 550 °C indicate that at low grazing incidence angles it suggests top surface layer the phases of CrN, bcc α-(Fe, Ni) in addition to visible substrate γ peaks.

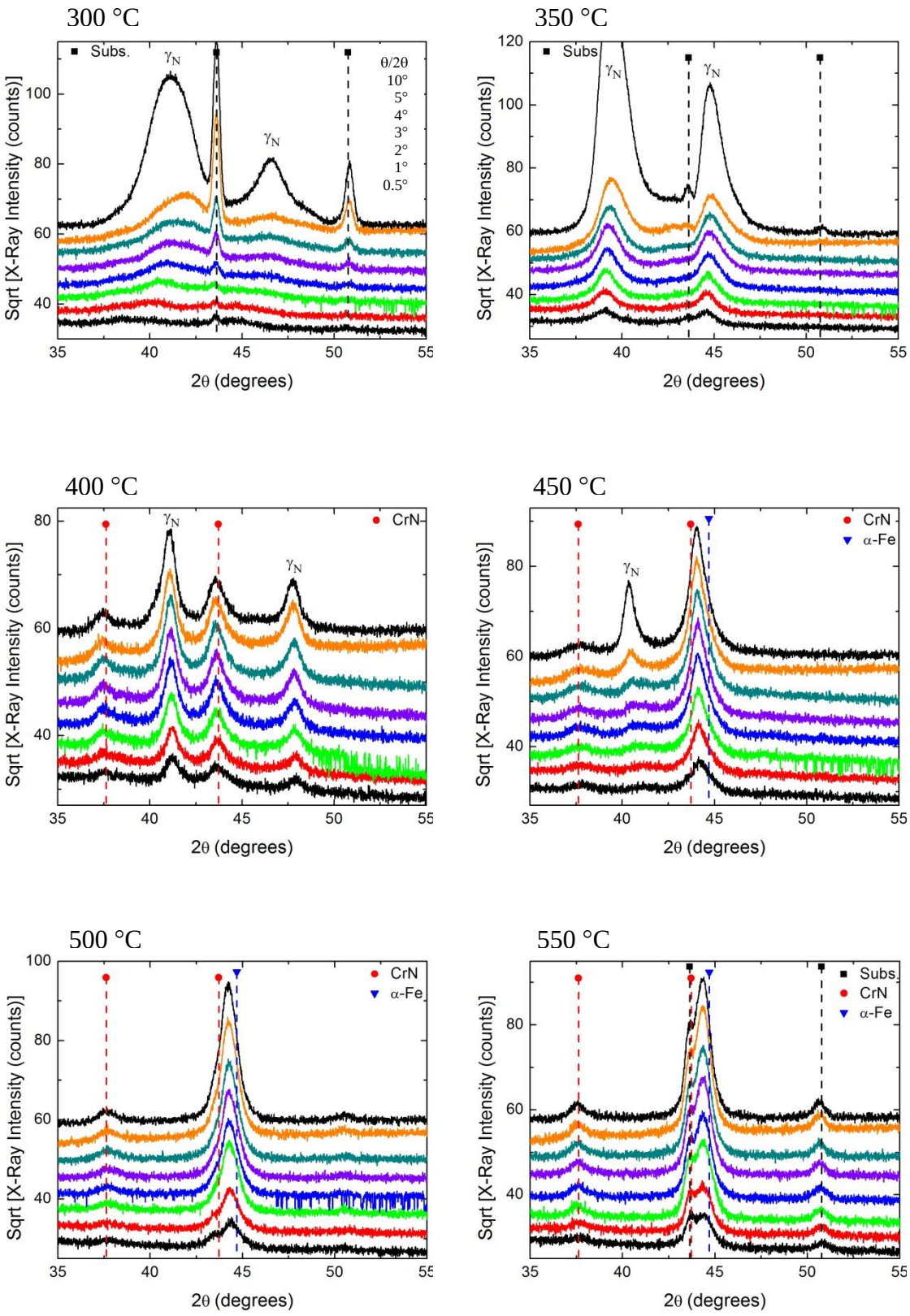

Figure 3.4. GIXRD results for N implanted 304 SS at different grazing angles from 0.5 to 10 degrees. Also, the top data in each graph belongs to XRD in θ/2θ geometry

3.2.3. θ/2θ XRD Results of Nitrogen Implanted CoCrMo

In Figure 3.5, the X-ray diffraction patterns of N implanted CoCrMo samples at various processing temperatures are shown. The XRD data looks identical for specimens processed at low temperatures (300, 350 °C). The broad peaks to the left of the substrate ones correspond to formation of the expanded phase for this alloy system. The γ_N layers on CoCrMo samples at these processing temperatures are found to be significantly thinner compared to the expanded γ_N layers on 304 SS. At the treatment temperature of 400 °C, the expanded layer formation is complete and a much thicker layer is developed (no substrate peaks are visible, similar to 304 SS at 350 °C). At processing temperatures 450 °C and above, the expanded phase is decomposing into CrN precipitates. The precipitation of CrN depletes the expanded austenite of chromium resulting in the formation of a mixture of fcc γ-CrN and the substrate phase [i.e., fcc γ-Co(Mo)]. At the highest processing temperature of 550 °C, this fcc phase is quite visible, albeit with a very low intensity and much broaden than the original substrate peaks. The expanded layer peaks exist up to temperatures of 450 °C, suggesting that at higher temperatures, the nitrogen containing layer is actually a mixture of CrN, and the Cr-depleted fcc phase.

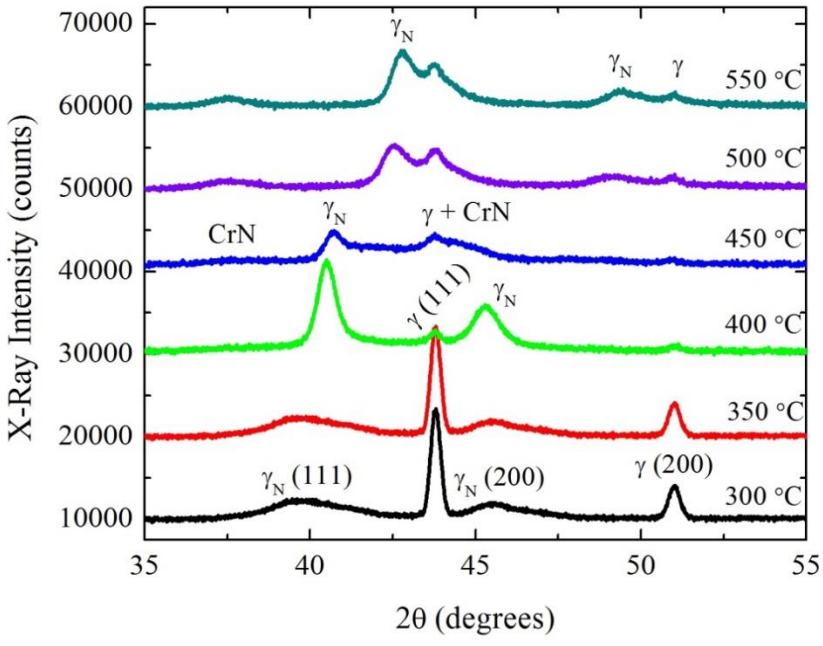

Figure 3.5. XRD data for N implanted CoCrMo alloys at various PIII treatment temperatures

3.2.4. GIXRD Results of Nitrogen Implanted CoCrMo

Figure 3.6 shows the GIXRD results for N implanted CoCrMo alloy samples as a function of implantation temperature. In this figure, the GIXRD data at the lower processing temperature (300, 350 °C) indicate that γ_N layer is observed at all grazing angles (from 0.5 to 10°). However, there are no substrate peaks at $\omega = 0.5°$ for N implanted specimen at 300 °C and at $\omega = 0.5°$, 1° for N implanted specimen at 350 °C. In addition, the GIXRD data at higher incident angles indicate that more contribution from the substrate is observed. Then, the top layer (~ 50 nm) in these samples only consists of γ_N phase. At the same time, the data suggests that the N implanted layer for the sample treated 350 °C is thicker compared to the sample processed at 300 °C. The GIXRD data for N implanted specimen at 400 °C shows that, at all grazing incident angles, no substrate peaks are visible. And the data clearly indicates that up to grazing incidence of 10 degrees the only phase in the layer is expanded phase, where γ_N layer is about 3-4 μm. According to this result, the γ_N layer thickness can be estimated with X-ray penetration depth into this sample, which the thickness of γ_N layer is determined from cross-sectional SEM and SIMS results in later chapter. The GIXRD data for 450 °C clearly shows that at the lowest grazing angle of 0.5° both CrN precipitates and γ_N phase are visible. At this processing temperature, decomposition into CrN starts. The GIXRD results look identical for samples processed at temperatures 500 °C and above. For both samples, the GIXRD data clearly indicate that at low grazing incident angles (from 0.5 to 3-4°) the peaks of γ_N phase are not visible. It suggests that the top layer only consists of CrN phase. As the grazing incident angles exceed up to 3-4°, it seems that there are two phase: CrN and γ_N phase. Additionally, the GIXRD data indicate most intense peak of CrN in sample treated at the highest processing temperatures (500, 550 °C) compared to sample at 450 °C. This means further decomposition of expanded phase into CrN. Then, at highest temperatures, there are only CrN precipitates in top surface layer. Another interesting feature is that at highest processing temperatures, still substrate peaks of the samples are visible. It suggests that γ_N layers on CoCrMo alloys are thinner compared to the expanded γ_N layers on 304 SS. These results are quite consistent with the results obtained from cross-sectional SEM and SIMS.

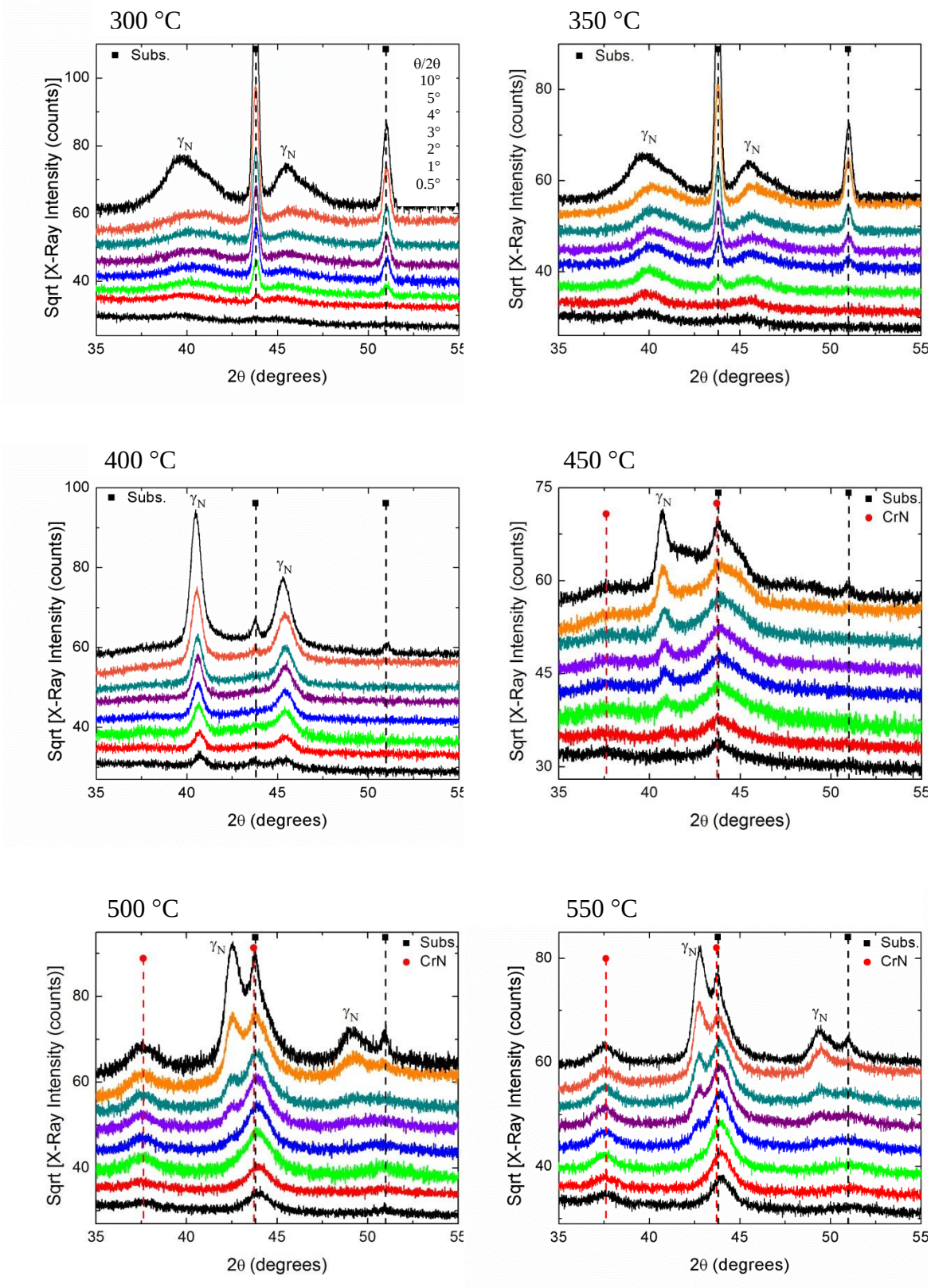

Figure 3.6. GIXRD results for N implanted CoCrMo at different grazing angles from 0.5 to 10 degrees. Also, the top data in each graph belongs to XRD in θ/2θ geometry

3.3. Summary

Figure 3.7 illustrates a schematic representation of fcc γ_N-(Fe,Cr,Ni) and γ_N-(Co,Cr,Mo) phases resulted after the nitrogen plasma immersion ion implantation. As shown in Figure 3.7, in these expanded phases, the nitrogen occupies octahedral sites in the fcc γ-substrate lattice. These simulations were carried out using VESTA software program. The fcc lattice of γ_N phase for N implanted 304 SS was simulated by taking the nitrogen content 39 at.%, in which nitrogen concentration was estimated using EDX analysis on N implanted specimen at 350 °C. For N implanted CoCrMo, nitrogen content used in the schematic drawing was 34 at.%, which was determined by EDX analysis on the surface of N implanted CoCrMo specimen at 400 °C.

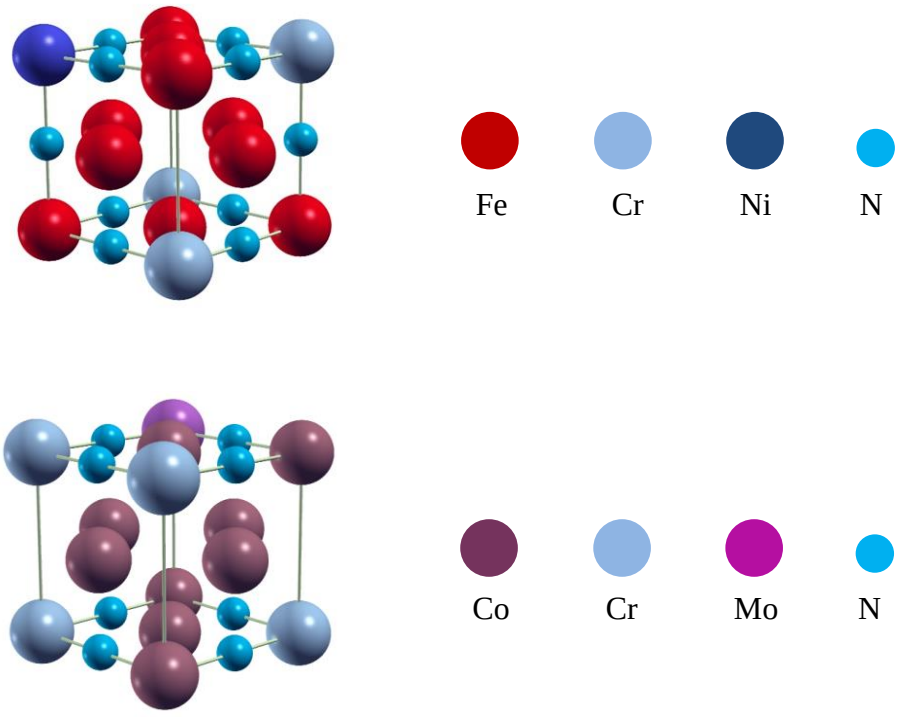

Figure 3.7. Schematic drawing for the crystal structures of N implanted 304 SS at 350 °C (top) and N implanted CoCrMo at 400 °C (bottom)

A simple model of phase distribution in each alloy as a function of implantation temperature is shown below. The model is based on the both θ/2θ XRD and GIXRD data.

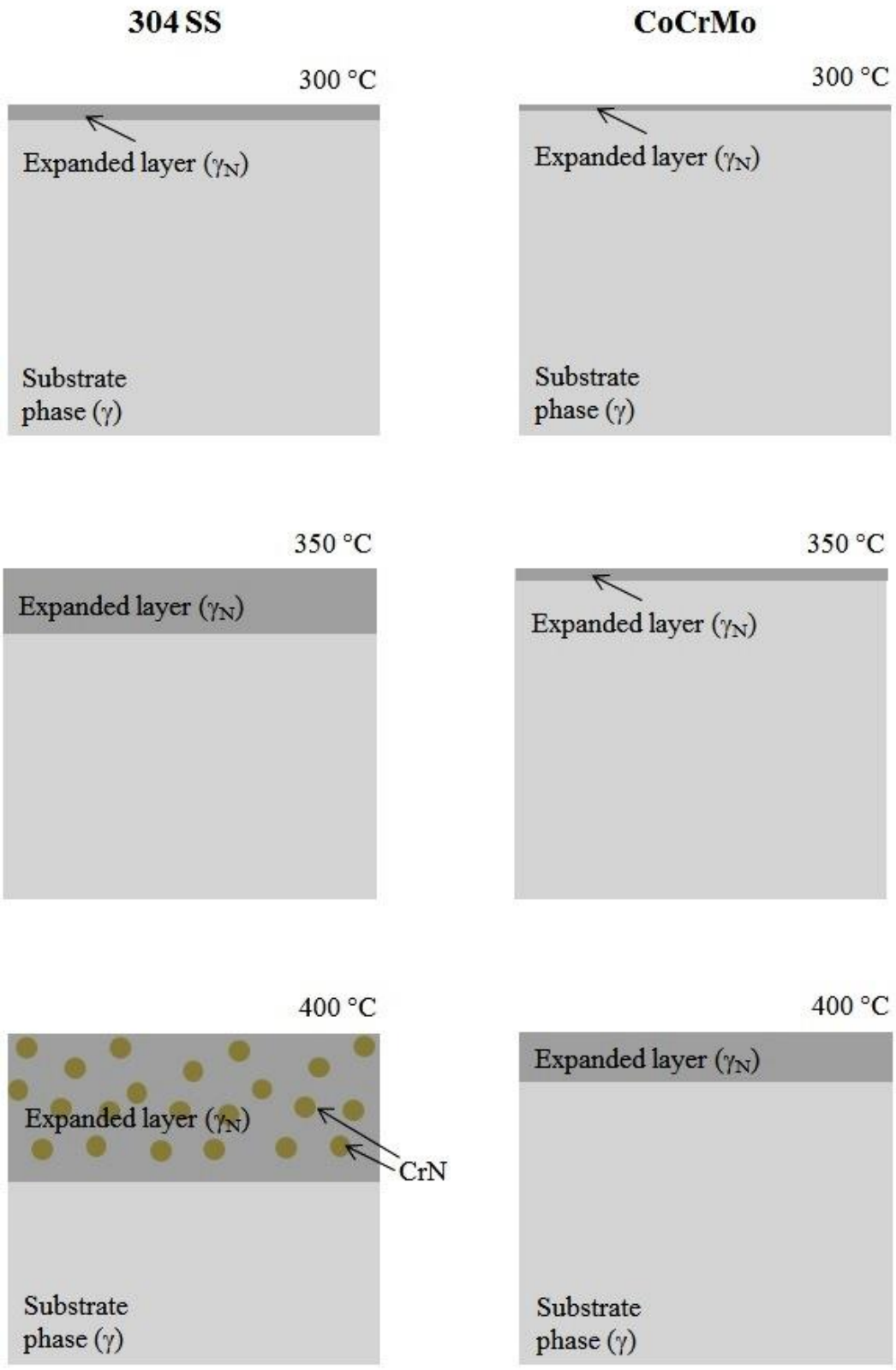

Figure 3.8. Schematic development of phase formation of 304 SS (left) and CoCrMo samples (right) with increasing PIII processing temperatures

(cont. on next page)

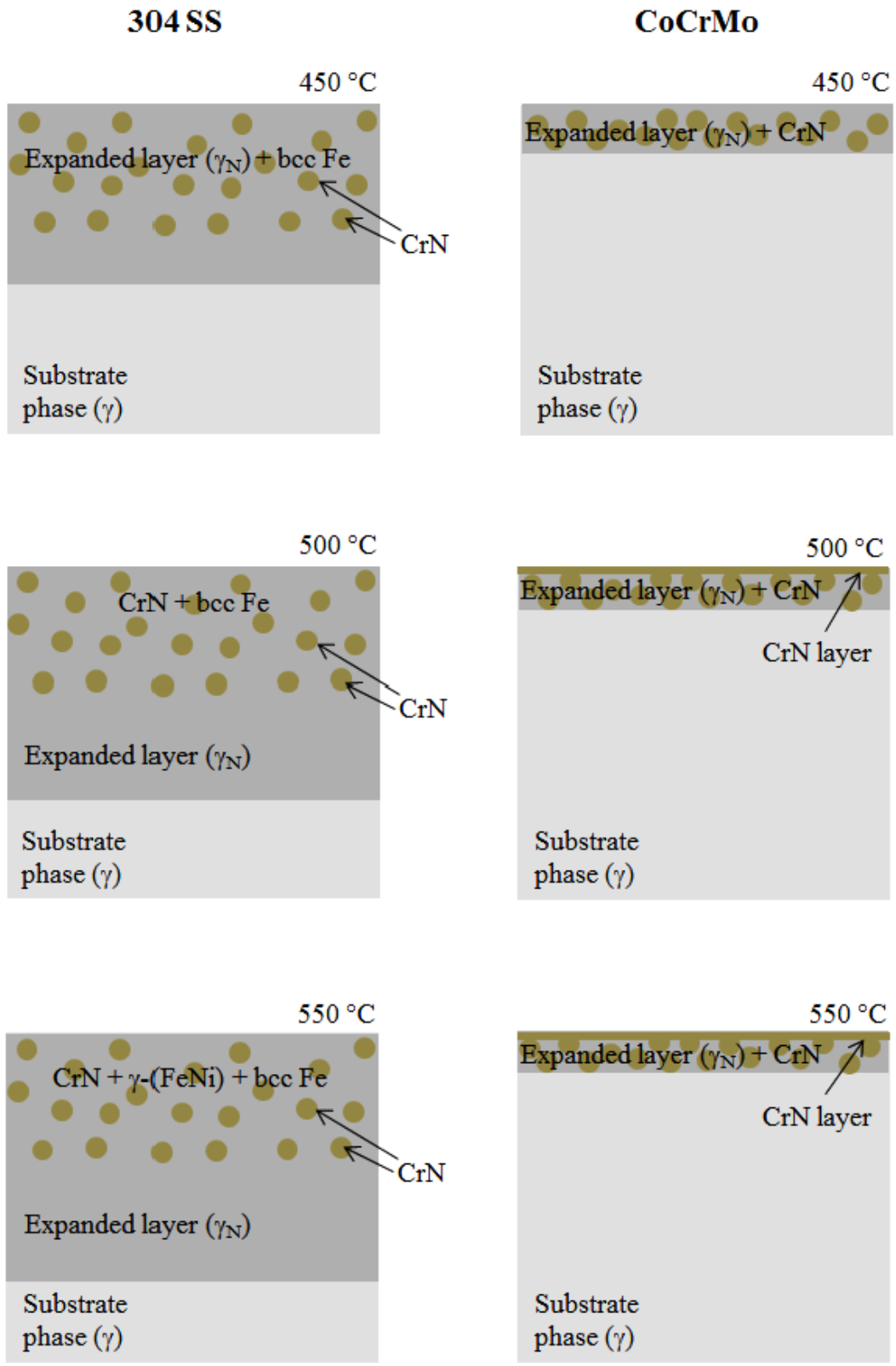

Figure 3.8. (cont.)

One interesting feature in Figure 3.3 and Figure 3.6 is that XRD peaks of γ_N are shifted to lower 2θ angles compared to the substrate γ peaks after nitrogen implantation process. The main reason of these shifts is due to the expansion that nitrogen creates in fcc lattice. Table 3.1 indicates 2θ peak centers of N implanted and substrate phases after PIII process at treatment temperatures (300, 350 °C). As can be seen in Table 3.1, the nitrogen implanted $\gamma_N(200)$ peaks are shifted more than $\gamma_N(111)$ peaks. It means larger lattice expansions in [200] direction than in [111] direction. It is probably due to higher N content in [200] direction compared to [111] direction.

Table 3.1. The 2θ centers of (111) and (200) peaks

	PIII temperature (°C)	γ(111)	$\gamma_N(111)$	γ(200)	$\gamma_N(200)$
304 SS	300	43.607	41.054	50.795	46.355
	350	43.563	39.335	50.863	44.782
CoCrMo	300	43.737	39.953	50.949	45.815
	350	43.762	40.025	50.971	45.764

Based on the XRD data of substrate and N implanted samples, 2θ values and lattice constants were quantitatively calculated using a curve-fitting program. These values are listed in Table 3.2.

Table 3.2. Lattice parameters, a, in Å for substrate and N implanted samples. <a> presents average lattice constants, while Δa/a refers to the relative difference in lattice parameters. Also, on the last column, average nitrogen contents are given in at.%, which were obtained from EDX analysis.

304 SS	Implantation temperature (°C)	a(111) (Å)	a(200) (Å)	<a> (Å)	$\frac{<\Delta a>}{<a>}$ (%)	Average N. Content (at.%)
	Substrate	3.596	3.598	3.597	-	-
	300	3.808	3.917	3.863	7.5	35
	350	3.967	4.048	4.008	11.4	39
	400	3.812	3.814	3.814	6.2	36

CoCrMo	Implantation temperature (°C)	a(111) (Å)	a(200) (Å)	<a> (Å)	$\frac{<\Delta a>}{<a>}$ (%)	Average N. Content (at.%)
	Substrate	3.581	3.584	3.583	-	-
	300	3.908	3.961	3.935	9.8	36
	350	3.902	3.965	3.934	9.8	38
	400	3.858	4.007	3.933	9.9	34
	450	3.837	-	3.837	7.0	36
	500	3.685	3.700	3.693	3.1	33
	550	3.667	3.685	3.676	2.5	31

Table 3.2 indicates the lattice constant values, a(111) and a(200) for both the substrate and the nitrogen implanted samples. In addition, in this table, average nitrogen concentrations can be found, which were obtained from EDX analysis.

CHAPTER 4

SURFACE TOPOGRAPHY

In this part, surface topography of substrate 304 SS and CoCrMo alloy samples as well as nitrogen implanted materials is presented. The experiments were carried out by using Atomic Force Microscopy (AFM) and Scanning Electron Microscopy (SEM). The aim of the experiments is to investigate surface changes (i.e., roughness, morphology) on samples as a result of nitrogen PIII process at different processing temperatures. In addition to these, the roughness of the sample surfaces depending on both average (Ra) and root-mean-square (RMS) were measured by AFM.

4.1. Substrate 304 SS and CoCrMo Alloy Surfaces

Before nitrogen PIII process, all 304 SS and CoCrMo samples were polished to mirror-like quality (see materials and experimental section). After polishing, AFM and SEM measurements were performed in order to investigate the surface topography of all polished specimens.

Figure 4.1 shows AFM topographical images of polished 304 SS and CoCrMo alloy with the scan area of 30 μm × 30 μm.

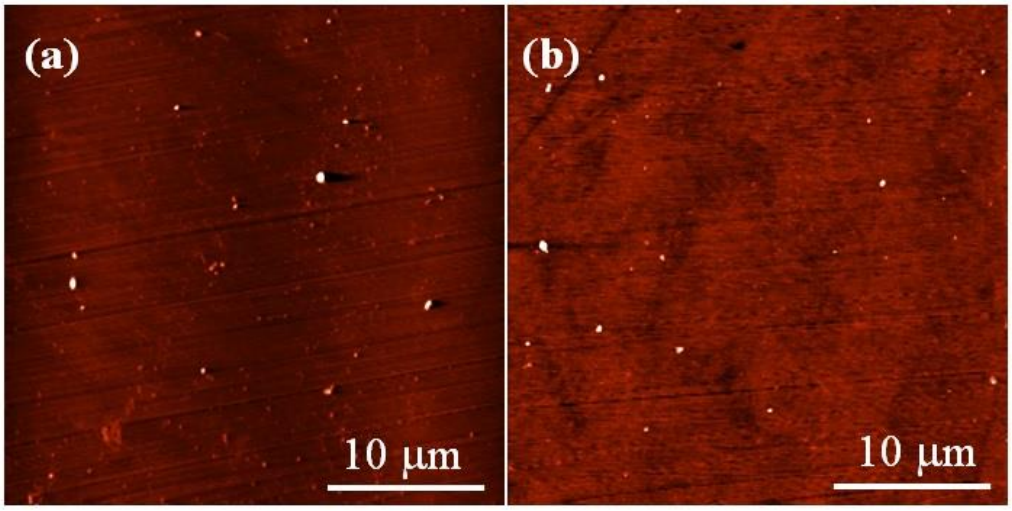

Figure 4.1. AFM images of polished 304 SS (a) and CoCrMo (b)

As can be seen from the images, the white particles on the surface of samples in both pictures are believed to be due to polishing defect. They are likely to be diamond particles from the polishing solution. In addition to that, the scratches on the surfaces are seen in the figures.

The above images were analysed by AFM, and the average roughness (Ra) and RMS (root-mean-square) roughness values for each polished sample were estimated based on at least three different scan areas. Table 4.1 lists the roughness values obtained from the analysis of the AFM images. As shown from Table 4.1, roughness value of CoCrMo alloy is less than 304 SS.

Table 4.1. Average (Ra) and RMS roughness values of polished 304 SS and CoCrMo alloy surfaces based on the AFM measurements.

	Ra (nm)	Rms (nm)
304 SS	2.45	4.94
CoCrMo	0.94	1.47

The SEM images of the polished 304 SS and CoCrMo alloy are shown in Figure 4.2. According to the SEM pictures, the scratches on both 304 SS and CoCrMo alloy are clearly revealed.

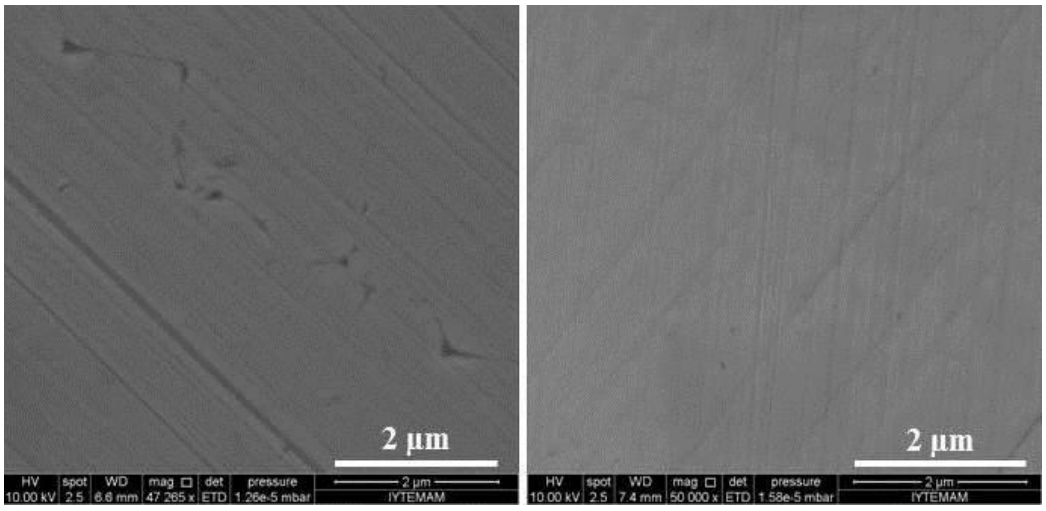

Figure 4.2. SEM images of polished 304 SS (left) and CoCrMo (right)

4.2. Nitrogen Implanted 304 SS and CoCrMo Samples

After nitrogen PIII process, surface topographical features of N implanted 304 SS and CoCrMo samples were investigated by AFM and SEM. Figure 4.3 shows AFM results of N implanted 304 SS samples at different processing temperatures, while Figure 4.5 indicates AFM results of N implanted CoCrMo samples. In addition to these AFM images, surface topographical features of N implanted 304 SS and CoCrMo surfaces obtained via SEM are shown in Figure 4.4 and Figure 4.6, respectively.

As can be seen from the 2-D and 3-D AFM images of the N implanted 304 SS surfaces with the scan areas of 30 μm × 30 μm in Figure 4.3, the grains are quite visible at low processing temperatures (300, 350 °C), whereas they are not clear for 304 SS samples processed at higher temperatures 400 °C and above. This may be due to more sputtering effect during PIII experiment at higher processing temperatures. And also, it may possibly be due to CrN precipitates into N implanted layer, as mentioned in both XRD and GIXRD data. The 2-D and 3-D AFM images of N implanted CoCrMo samples with the scan areas of 30 μm × 30 μm are illustrated in Figure 4.5. There, at all PIII processing temperatures, the grain shape and sizes of N implanted CoCrMo samples are quite visible.

The SEM images of the N implanted 304 SS samples at different processing temperatures are given in Figure 4.4. As shown in the figure, the grains of N implanted samples processed at lowest temperatures (300, 350 °C) are quite visible. However, as the treatment temperature increases, this visibility becomes weak. Surface topographical features of N implanted CoCrMo surfaces obtained via SEM are shown in Figure 4.6. One can clearly see the grains which become quite visible as the processing temperature increases compared to 304 SS.

Both AFM and SEM images correlate quite well for each sample category. In addition, the images give information about grain size of the sample. As can be seen from the all AFM and SEM images, the nitrogen implantation process does not change grain sizes of investigated samples in this study.

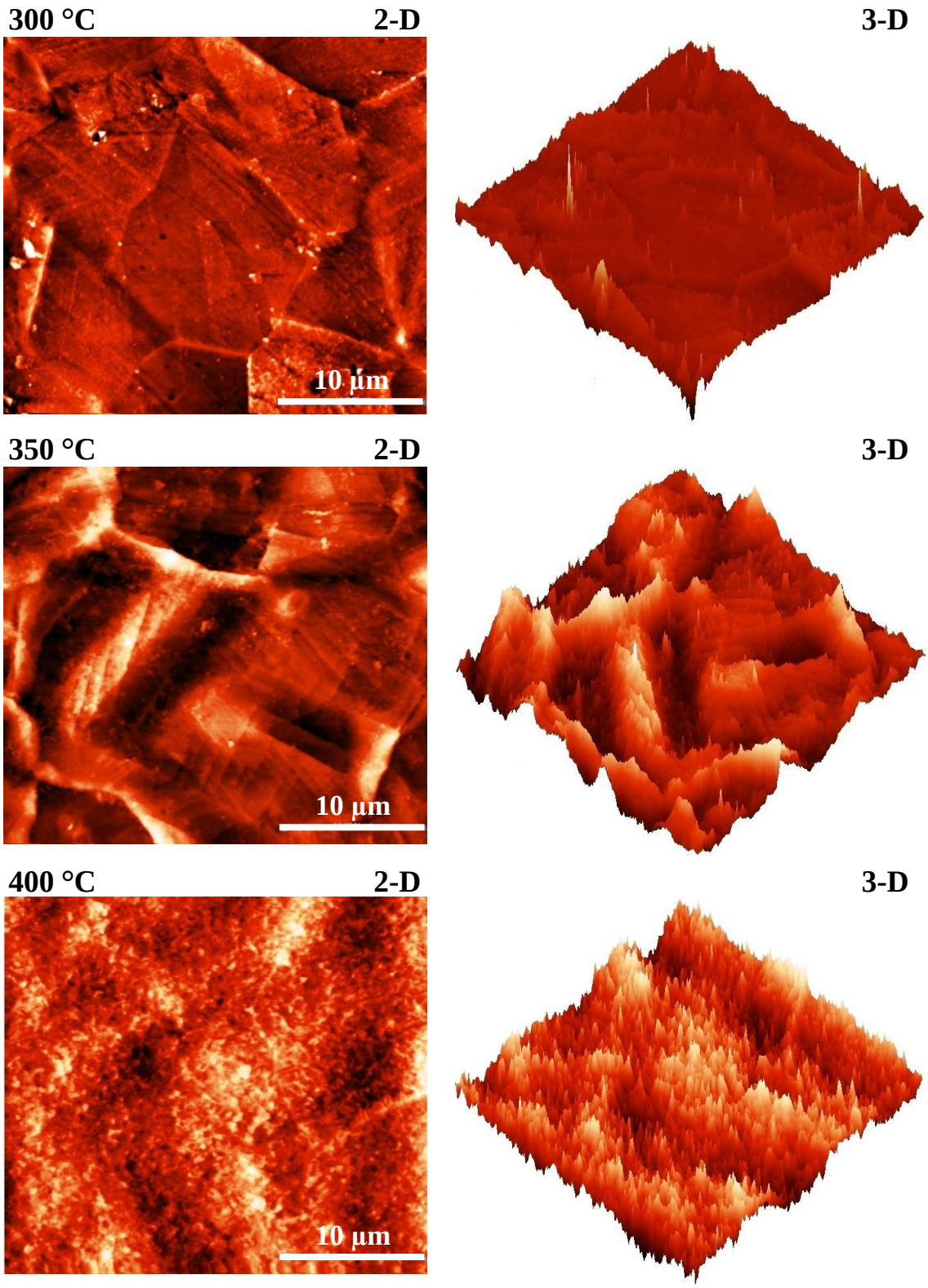

Figure 4.3. AFM images 2-D (left) and 3-D (right) of nitrogen implanted 304 SS as a function of PIII temperature

(cont. on next page)

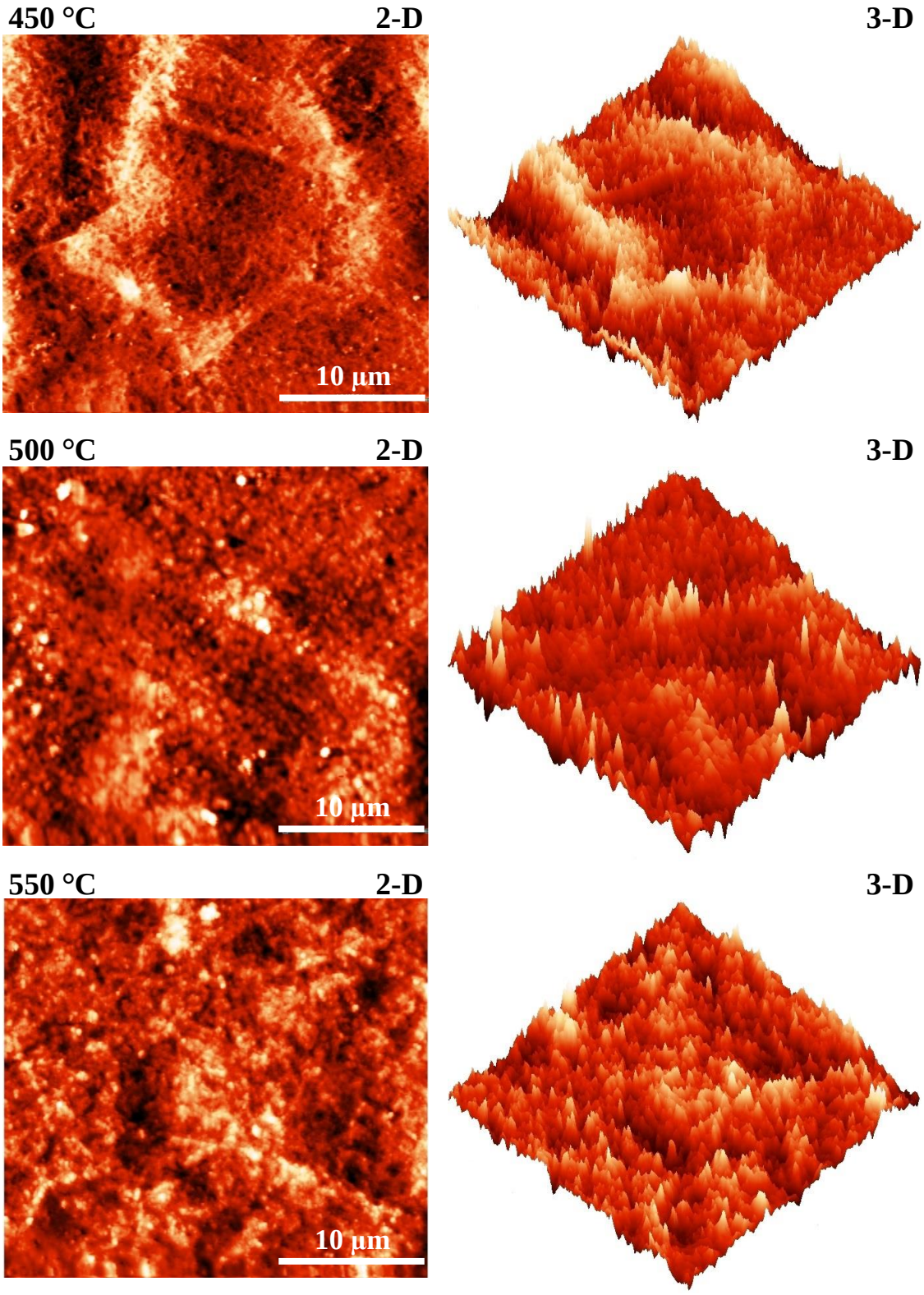

Figure 4.3. (cont.)

300 °C

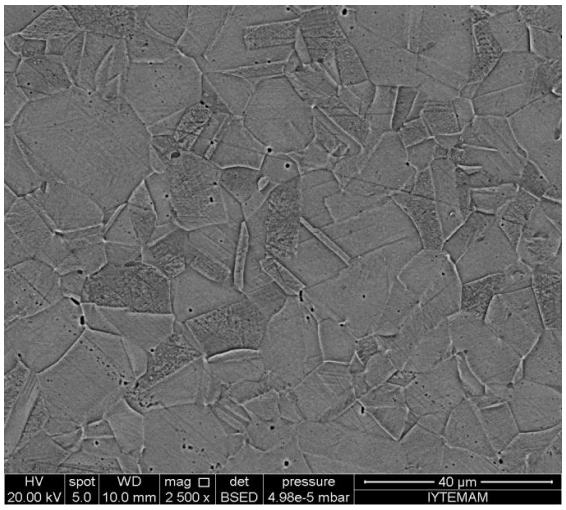

350 °C

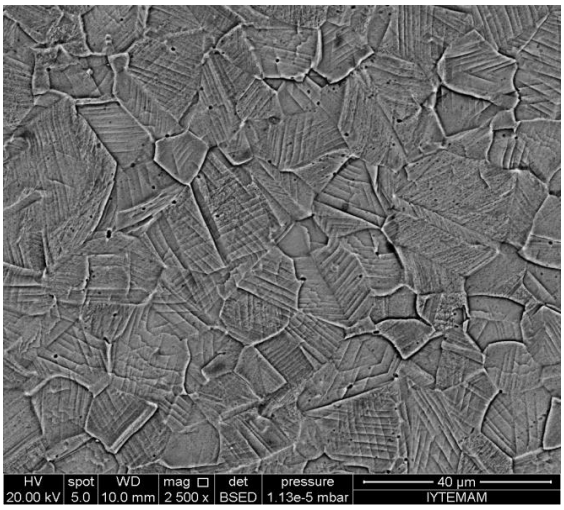

400 °C

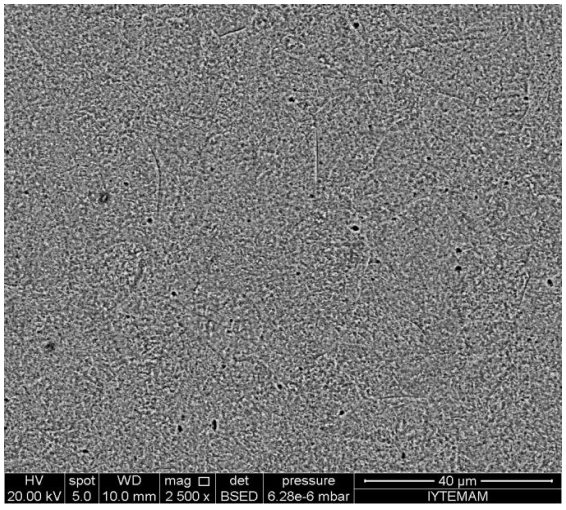

450 °C

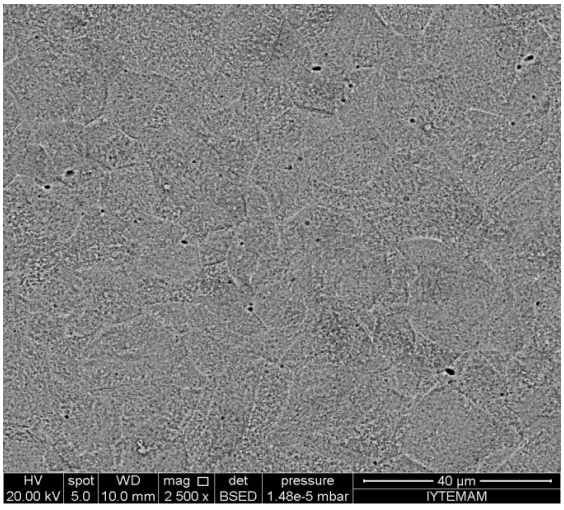

500 °C

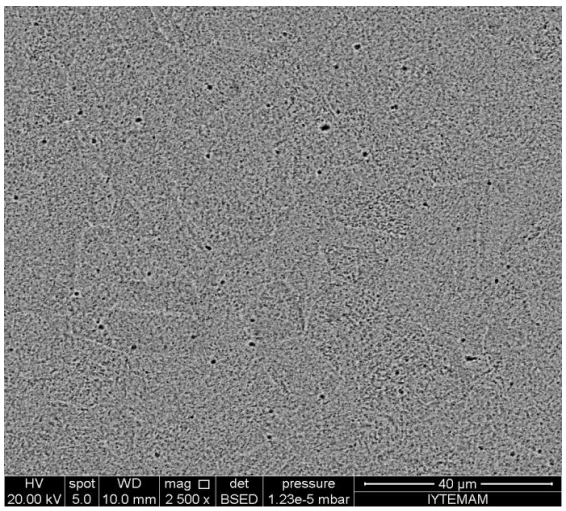

550 °C

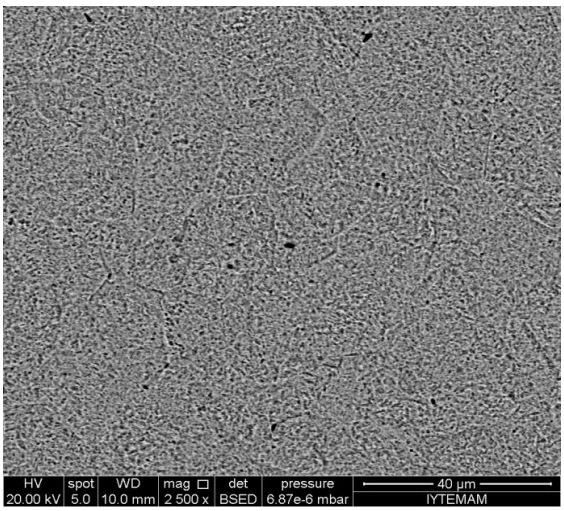

Figure 4.4.SEM pictures of nitrogen implanted 304 SS at different processing temperatures

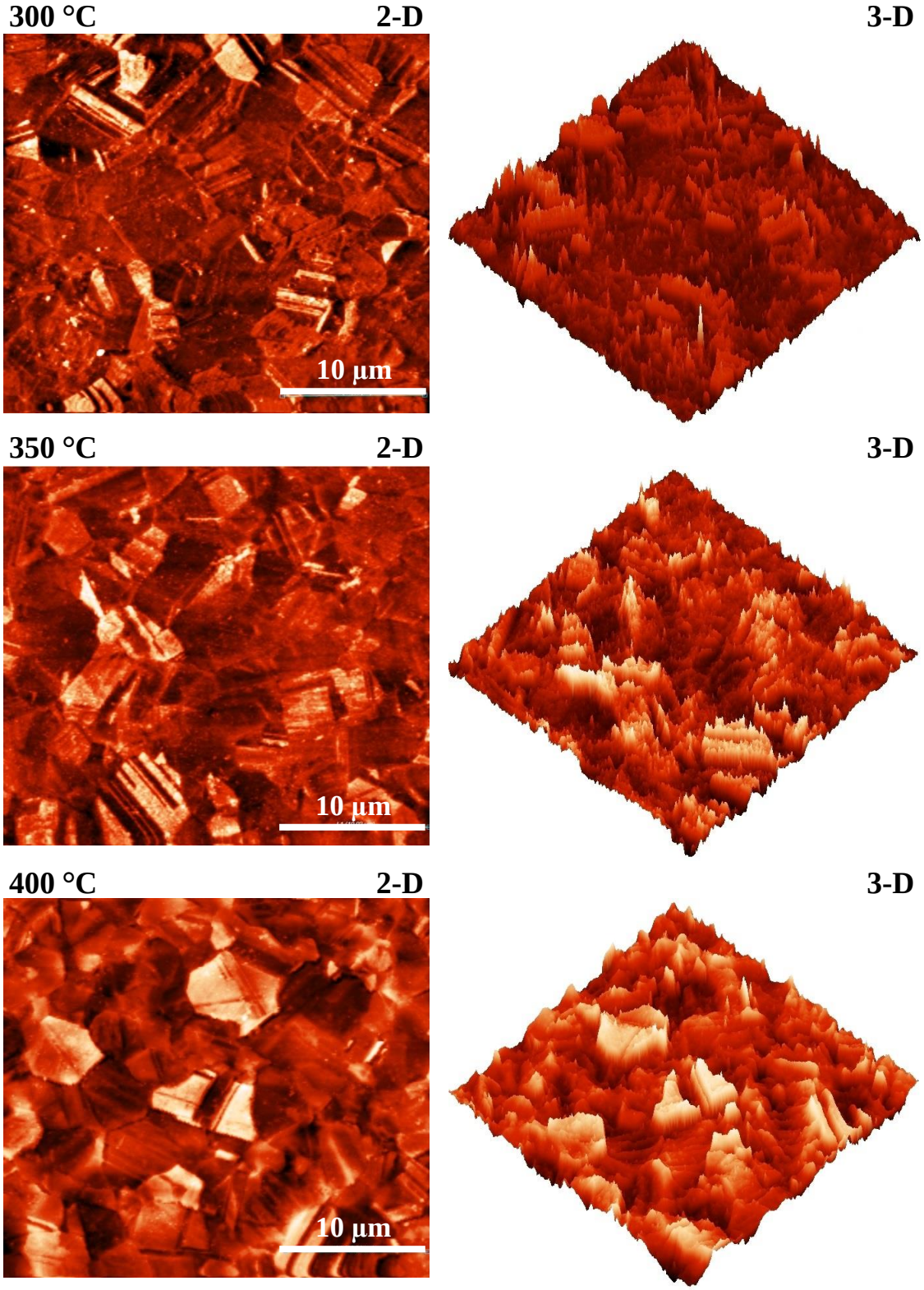

Figure 4.5. AFM images 2-D (left) and 3-D (right) of nitrogen implanted CoCrMo as a function of PIII temperature

(cont. on next page)

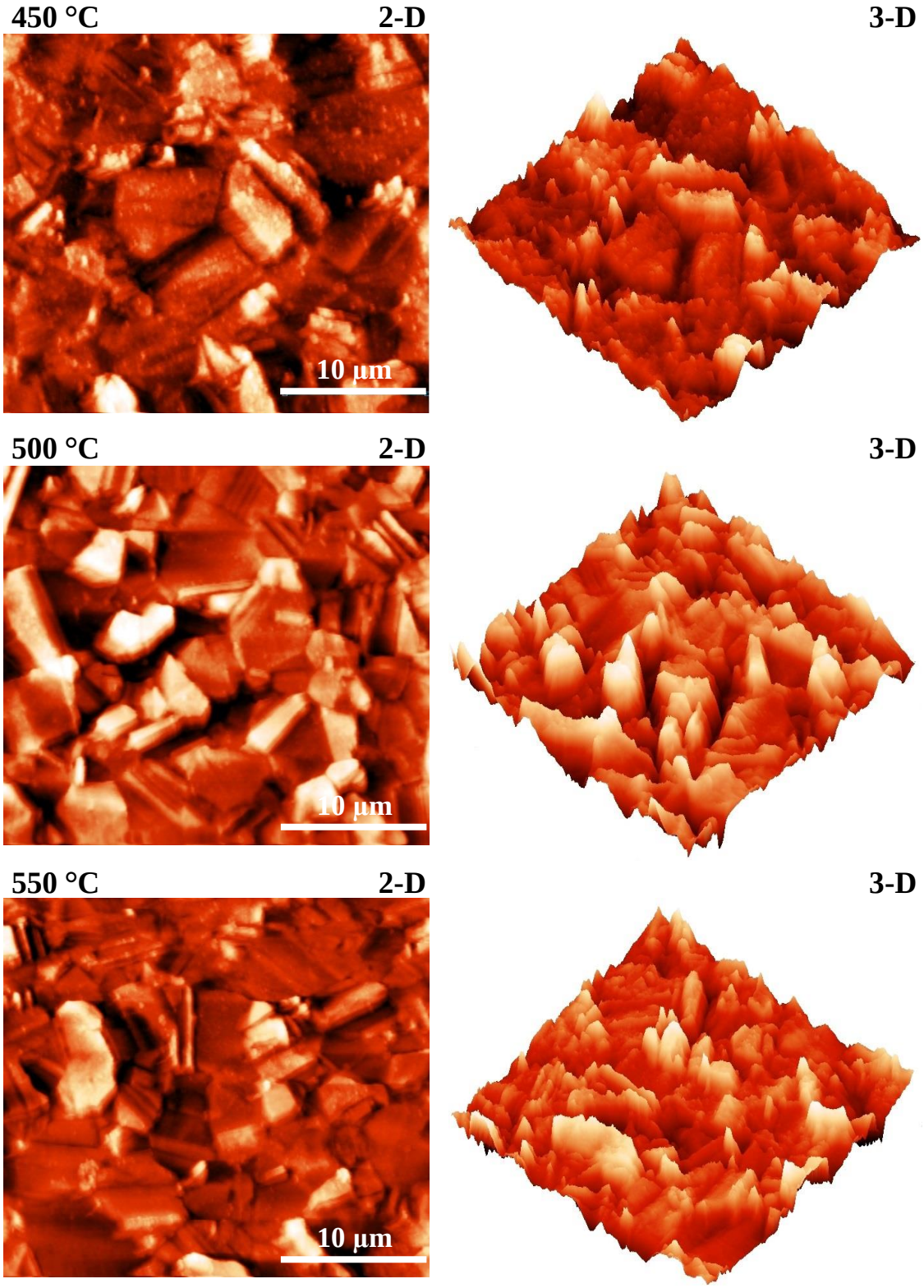

Figure 4.5. (cont.)

300 °C

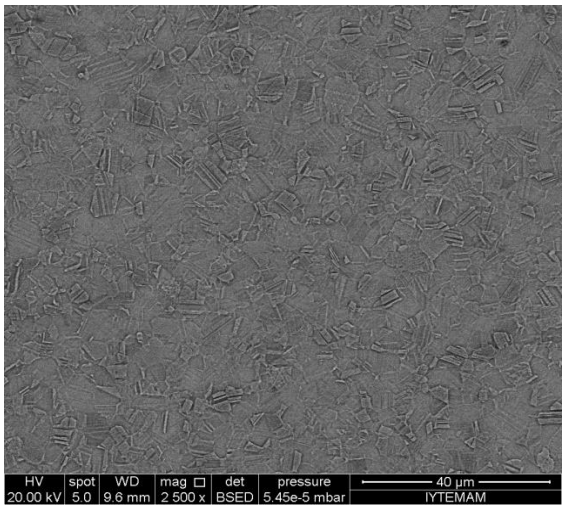

350 °C

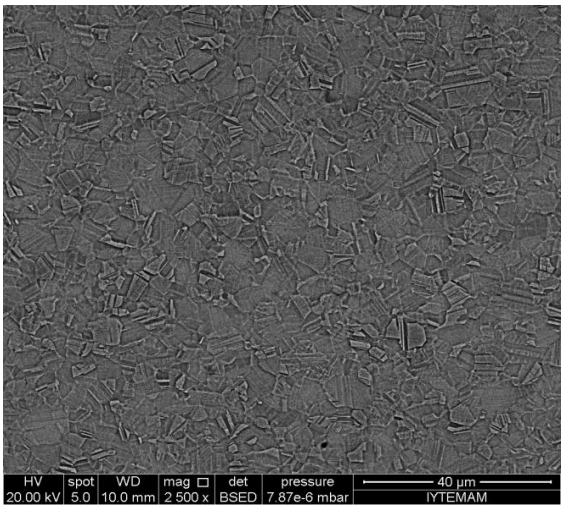

400 °C

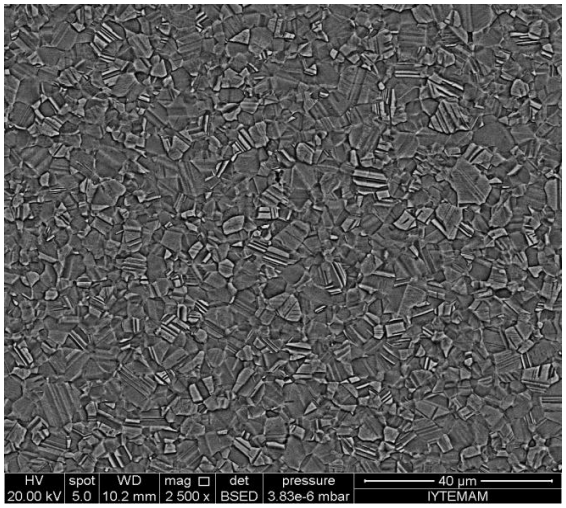

450 °C

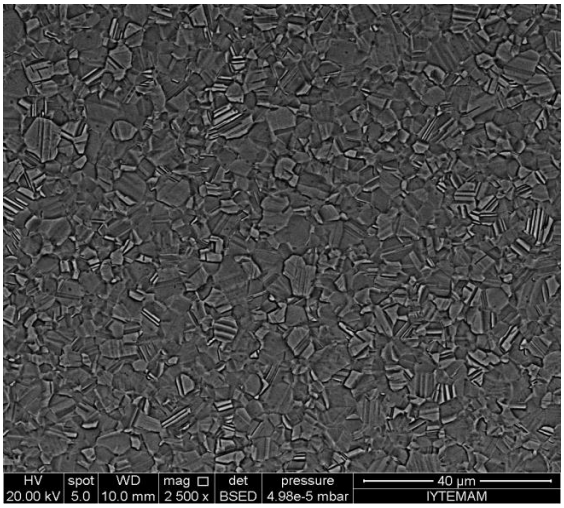

500 °C

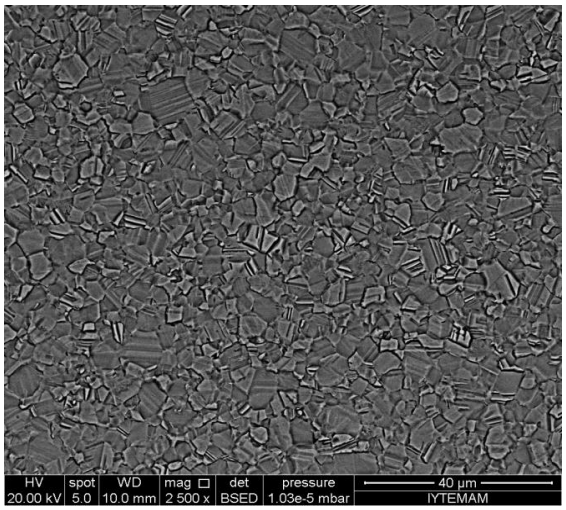

550 °C

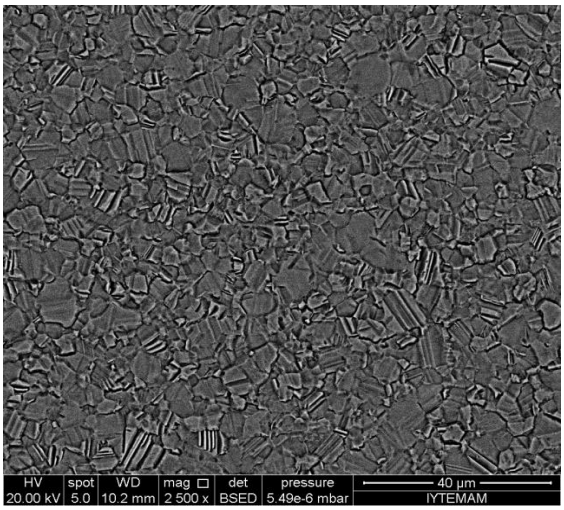

Figure 4.6. SEM pictures of nitrogen implanted CoCrMo at different processing temperatures

One feature obtained from both AFM and SEM images is that the N implanted samples at all treatment temperatures do not have a homogenous grain structure on the surface, grain size and shape change through the surface. It may be due to that the different grains may have different roughness values depending on different grains have different lattice expansions (implying different N contents). In addition, as can be clearly seen from the SEM pictures, the grain size of N implanted 304 SS samples is larger than N implanted CoCrMo samples. A study (Öztürk et al., 2006) in literature shows that the grain sizes for CoCrMo samples change from 5 μm to 15 μm. Another study (Öztürk et al., 2009) indicates that the grain size of austenitic stainless steel (SS) changes range between 25 μm and 50 μm.

As can be seen from the figures obtained from both AFM and SEM, there is a clear evidence that the nitrogen implanted surfaces are rougher than the polished substrate surfaces. During the nitrogen PIII process, AFM and SEM results show that significantly a sputtering effect is revealed. And, also this sputtering is much more intense as the processing temperature increases. As discussed in the experimental section, in order to increase the processing temperature, pulse frequency is increased and this results in higher nitrogen ion beam. The sputtering increase may be due to higher nitrogen coming on the samples. The surface roughness increases as a function of processing temperature. Although there is a significant sputtering, the images clearly show that the grain size remains the same.

Table 4.2 lists the average and RMS roughness values of N implanted surfaces as well as polished surfaces. Also, these RMS roughness values of the all samples are shown in Figure 4.7. As can be seen from the table and figure, roughness values of N implanted samples increase as a function of PIII processing temperature. While the roughness of the 304 SS is approximately 31 nm, the average roughness of CoCrMo surface is about 61 nm for the samples processed at 500 °C. Here, the higher increase in roughness values is revealed for N implanted 304 SS at 350 °C, whereas it becomes for N implanted CoCrMo at processing temperature of 400 °C. It may be due to that, as mentioned in XRD results, γ_N formation in both 304 SS and CoCrMo samples fully was revealed these temperatures. And, larger lattice expansion rates for differently oriented grains are revealed into samples processed at these temperatures.

Table 4.2. Average (Ra) and root-mean-square (RMS) roughness values of polished and N implanted 304 SS and CoCrMo surfaces based on the AFM measurements

	304 SS		CoCrMo	
T (°C)	Ra (nm)	Rms (nm)	Ra (nm)	Rms (nm)
substrate	2.4	4.9	0.9	1.5
300	17.0	23.6	17.1	22.8
350	48.5	63.2	27.7	36.0
400	40.8	51.9	59.5	75.1
450	42.1	53.8	60.3	77.6
500	31.2	41.3	60.9	79.0
550	46.7	59.2	60.5	78.3

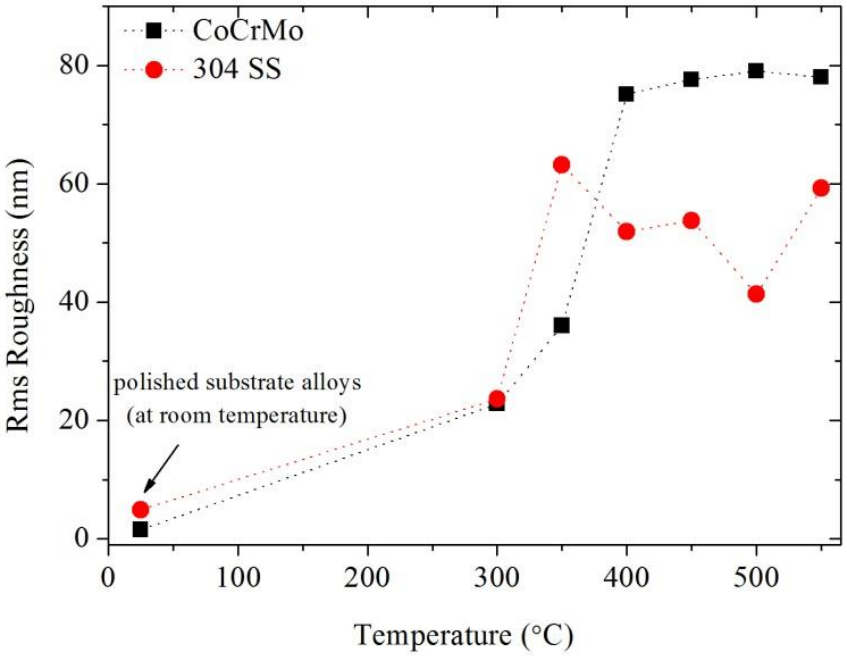

Figure 4.7. RMS roughness values of the substrate samples and N implanted 304 SS and CoCrMo samples as a function of nitrogen implantation temperature

As shown the AFM images, some grains in a specimen appear to be higher than others. White grains refer to have been higher compared to dark grains. It can be said that the different grains may have different roughness values depending on that different grains have different lattice expansions. According to the XRD results, the lattice expansion of (200) oriented grains is higher than the lattice expansion of (111) oriented

grains. Therefore, the reason for unhomogenity of the surfaces may be due to different nitrogen concentration of the grains as well as their different lattice expansions. Also, the compressive stresses may contribute to the increased surface roughness of the N implanted samples (Ozturk and Williamson, 1995).

One important feature obtained AFM and SEM images are that while the surface changes on N implanted CoCrMo samples do not observed at all treatment temperature, it reveals on N implanted 304 SS specimens at the processing temperature 400 °C and above. As discussed in XRD results, for N implanted 304 SS, CrN decomposition starts at the processing temperature 400 °C. And, CrN decomposition for N implanted CoCrMo becomes at 450 °C. However, there is one important thing between them, which is the intensity of CrN peaks into 304 SS is much more intense compared to CoCrMo samples.

CHAPTER 5

MFM IMAGING ANALYSIS

Magnetic characterization of the polished and N implanted samples investigated in this work was performed using magnetic force microscopy (MFM). The magnetic structures of the sample surfaces were imaged with MFM as a result of variation in the force between the magnetized probe and magnetic stray field originating from the sample surface. The topographic and magnetic images of the samples were simultaneously obtained from the same scanning regions with two-pass technique. As mentioned before (Chapter 2, MFM), during two-pass technique in the MFM measurements, both topography and magnetic image are obtained simultaneously; the second pass is executed with displacement from the first pass level, which can be changed from sample to sample. In our experiments, it was tried different tip-sample distances (ranging from 60 nm to 300 nm) to obtain better images. It is well-known that while the tip-surface distance increases, the magnetic signal weakens and shows a lower magnetic contrast. A study (Dias and Andrade, 2000) about the tip-sample distance shows that the short-range forces do not act for distances above 20-25 nm. Magnetic interactions are related to long-range forces, which act typically between 10 and 500 nm depending on the sample. Magnetic interaction are commonly found between 5 and 300 nm in similar stainless steels (Neves and Andrade, 1999). In our case, at distances around 300 nm, the magnetic interaction could still be observed for N implanted CoCrMo alloy surfaces.

5.1. Substrate 304 SS and CoCrMo Alloy Surfaces

Figure 5.1 shows the results of MFM measurement for the polished 304 SS and CoCrMo alloy surfaces. As can be seen from Figure 5.1, there are only scratches and dust particles in the AFM (topographic) images of the polished samples. In the MFM (phase) images, the magnetic structure is not observed on the surface of the polished CoCrMo alloy, while distinct magnetic patterns are easily identified in certain region of the MFM image taken on the surface of the polished 304 SS sample.

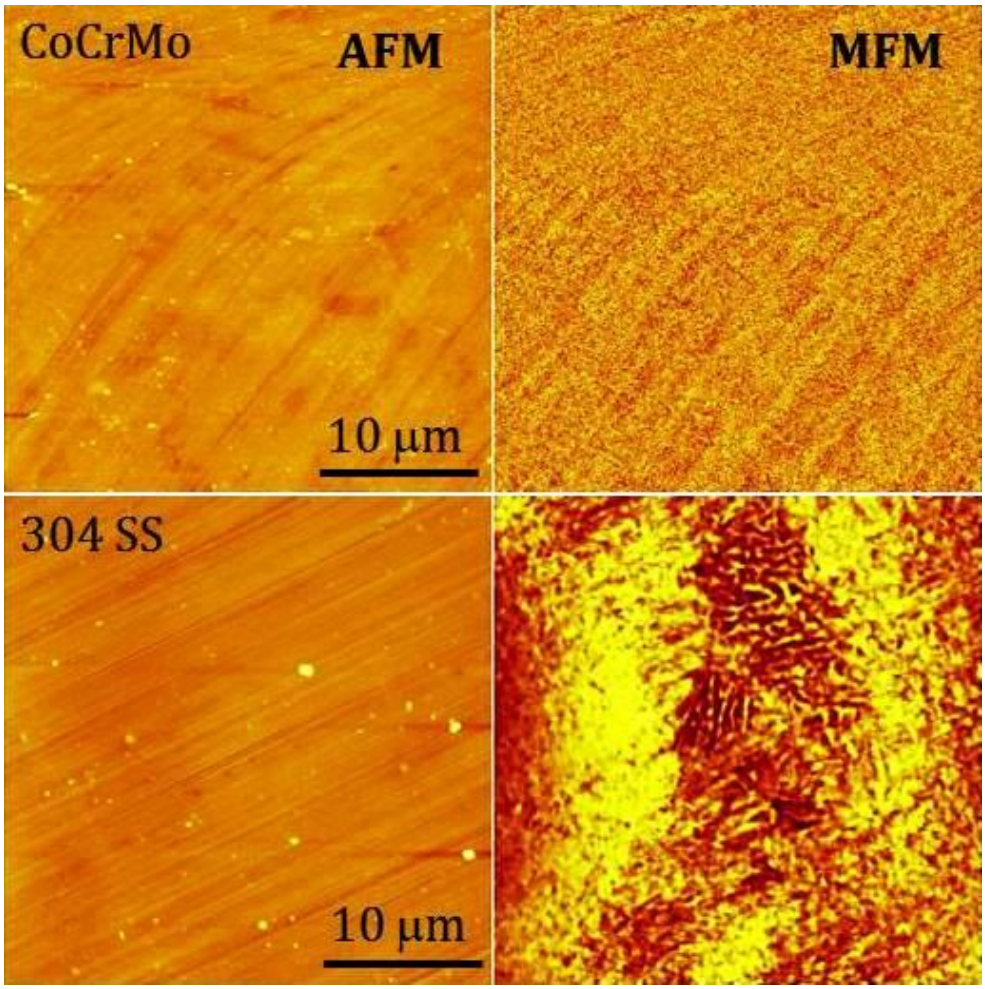

Figure 5.1. AFM (left) and MFM (right) images of the same regions for the polished 304 SS and CoCrMo alloy

The magnetic patterns on 304 SS are magnetic domains of the strain-induced martensite phase that is formed on the top surface (~ 50 - 100 nm) due to the polishing process, which is confirmed by both XRD and GIXRD results. Parts of the image with no magnetic contrast probably belong to the untransformed paramagnetic austenite. On the other hand, it seems the polishing process does not modify the magnetic structure of the CoCrMo alloy since no magnetic contrast in the MFM image of the polished surface of CoCrMo alloy. Several studies (Seetharaman and Krishnan, 1981; Tavares et al., 2002) in literature show that austenitic stainless steels may become ferromagnetic when the martensite phase is produced by effects such as cold work deformation, stress.

5.2. Nitrogen Implanted 304 SS and CoCrMo Alloy Surfaces

Figure 5.2 demonstrates AFM (topographic) and MFM (phase) images taken on the surface of N implanted 304 SS at processing temperature of 350 °C.

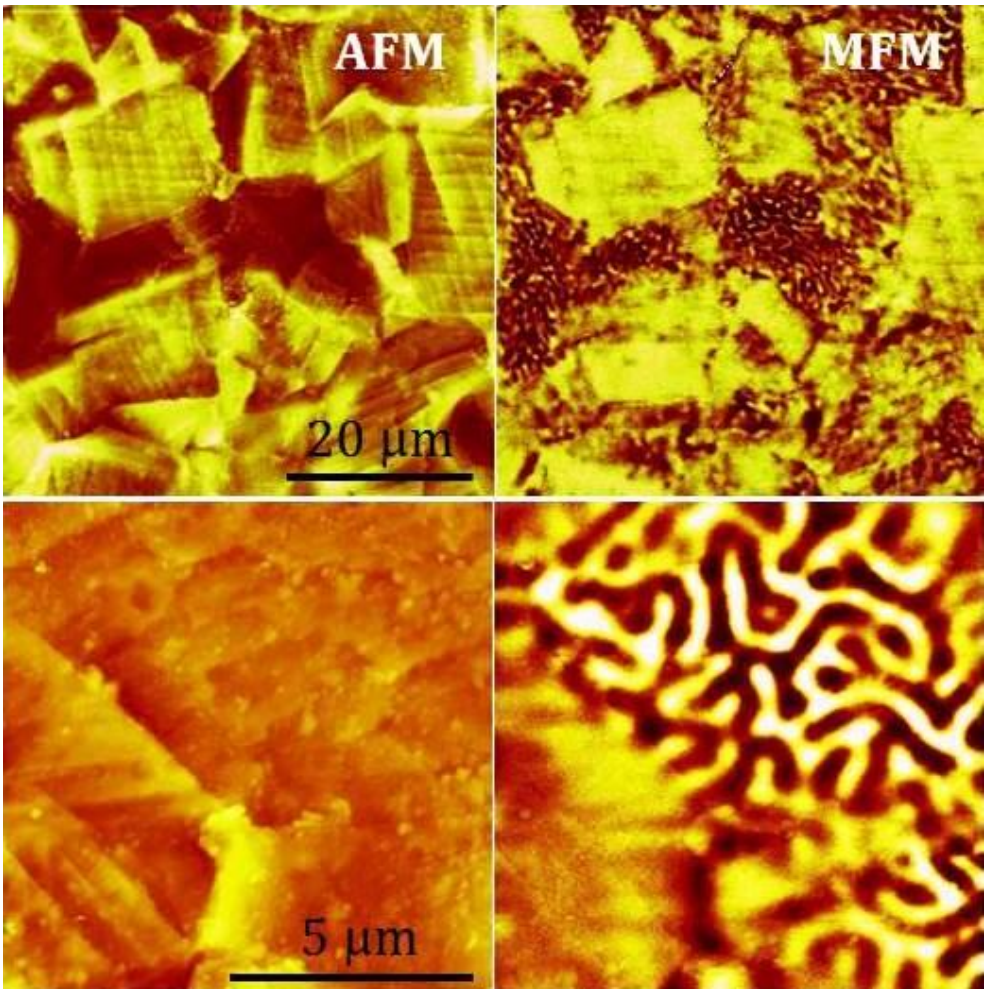

Figure 5.2. AFM (left) and MFM (right) images of the same regions for the N implanted 304 SS. The figure below displays the images from higher magnification for same specimen

Stripe-like domains are quite visible in parts of the image suggestive of ferromagnetism for the N implanted layer. There is a correlation with the XRD results which only indicate the expanded phase layer on this sample at this temperature. On the other hand, as can be seen from the image, there is no magnetic contrast in some grains. This may be due to the paramagnetic γ_N or the magnetization lies in plane (stripe domains are typical of mostly out-of-plane magnetization).

In this study, MFM imaging was not possible for N implanted 304 SS samples at other processing temperatures. We believe that this may be probably due to technical problems. In addition to this, as shown in AFM and SEM results, some defects on the surfaces of 304 SS samples processed at temperatures higher than 350 °C were observed, which was due to much more sputtering during PIII process. Because of this, MFM imaging might not able to analysed for N implanted samples at higher processing temperatures. In literature, a study (Basso et al., 2009) of magnetic and structural features of an ion implanted 316 SS suggest that the variations of the magnetic domain pattern can be associated with grain boundary, crystalline defects and local deformation.

Imaging by MFM for N implanted 304 SS at higher temperatures would be important to distinguish the ferromagnetism of the expanded phase/layer from the layer treated at 350 °C. The XRD data for the 304 SS sample treated at 550 °C shows CrN precipitates and the Cr-depleted matrix of bcc α-(Fe, Ni) as a consequence of the expanded phase layer decomposition. It would be interesting to investigate the surface of this sample using MFM since bcc α phase is known to be ferromagnetic.

Figure 5.3 displays a sequence of AFM/MFM images showing the surface of N implanted CoCrMo samples with increasing processing temperatures. MFM imaging was carried out on all N implanted CoCrMo specimens except on the sample implanted at 300 °C. As can be seen from Figure 5.3, the ferromagnetism for the N implanted CoCrMo surfaces is quite visible through the observation of the striped domains, especially for the samples treated at 400 and 450 °C. The dark (light) stripe domain patterns observed in the MFM images are up (down) modulation of out-of-plane magnetization component. As shown from the images above, the magnetic domains in the MFM images exhibit different patterns from one grain to another. The domain morphology (i.e., size and shape) and the periodicity of domains even changes within a given grain.

Different domain patterns suggest different magnetic behaviour from grain-to-grain. For the surfaces treated at 400 and 450 °C, this is probably attributed to different amounts of lattice expansion (due to different N contents) in the different grains as evidenced in the XRD results. According to the XRD data, the expanded phase is the dominant crystal structure in these surfaces, and the (200) γ_N peak is shifted more than the (111) γ_N peak. The domain size/shape variations observed on the different grains may be due to the different intrinsic magnetic properties of the expanded phase in those

grains. Although not carried out in this study, published papers (Menéndez et al., 2010; Wu et al., 2011) have already established correlations between the domain structure and crystal orientation.

Although it is not seen as distinct and striped domains on the images of the surfaces at 400 and 450 °C, the MFM images of the sample surfaces treated at 500 and 550 °C show domain patterns/structures. The domains are much more apparent for the sample surface treated at 550 °C compared to that at 500 °C although their XRD patterns are nearly identical. It is also clear from the MFM images that some grains show no magnetic contrast. This may be due to either an in-plane magnetization component or the expanded phase with less lattice expansion (lower N content). The latter seems more plausible since the XRD data for these samples show the expanded phase decomposing into CrN precipitates and the Cr-depleted matrix, fcc γ-Co(Mo)

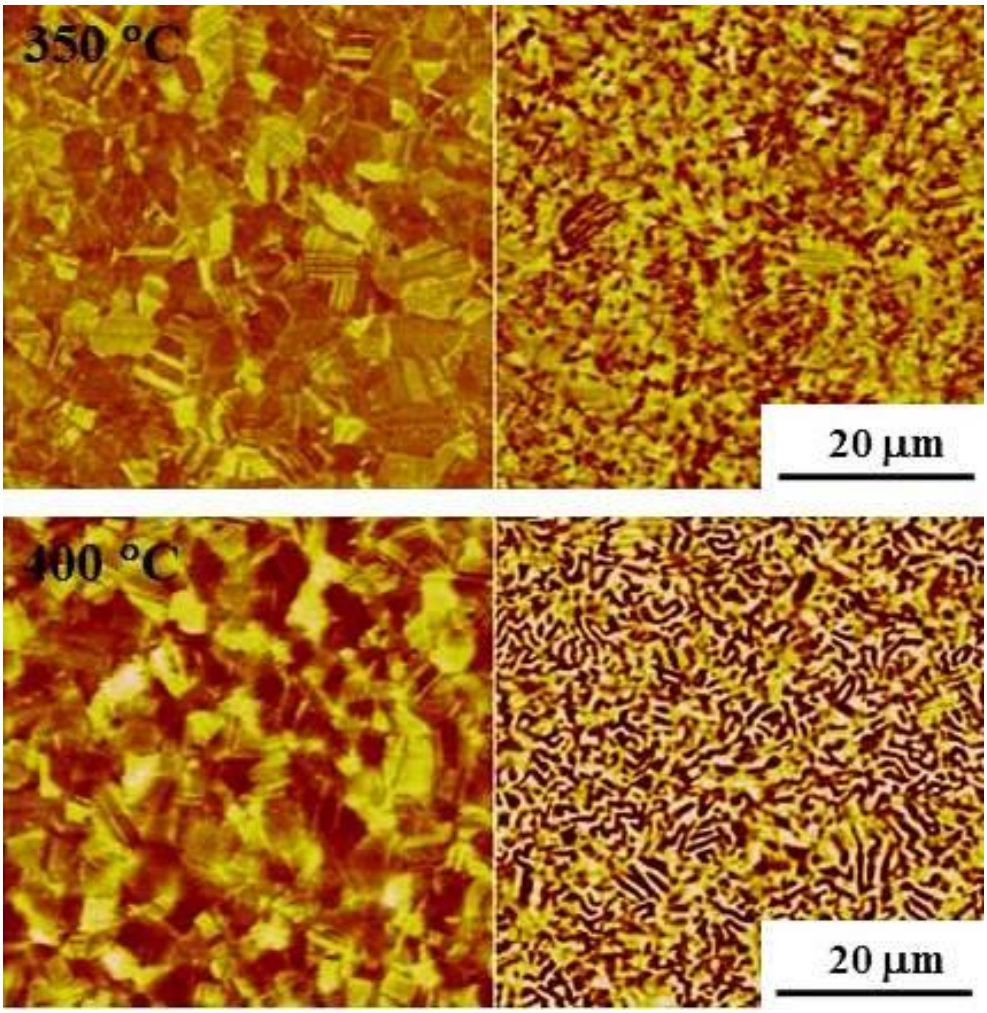

Figure 5.3. AFM (right) and MFM (right) images of the same regions for N implanted CoCrMo at different processing temperatures

(cont. on next page)

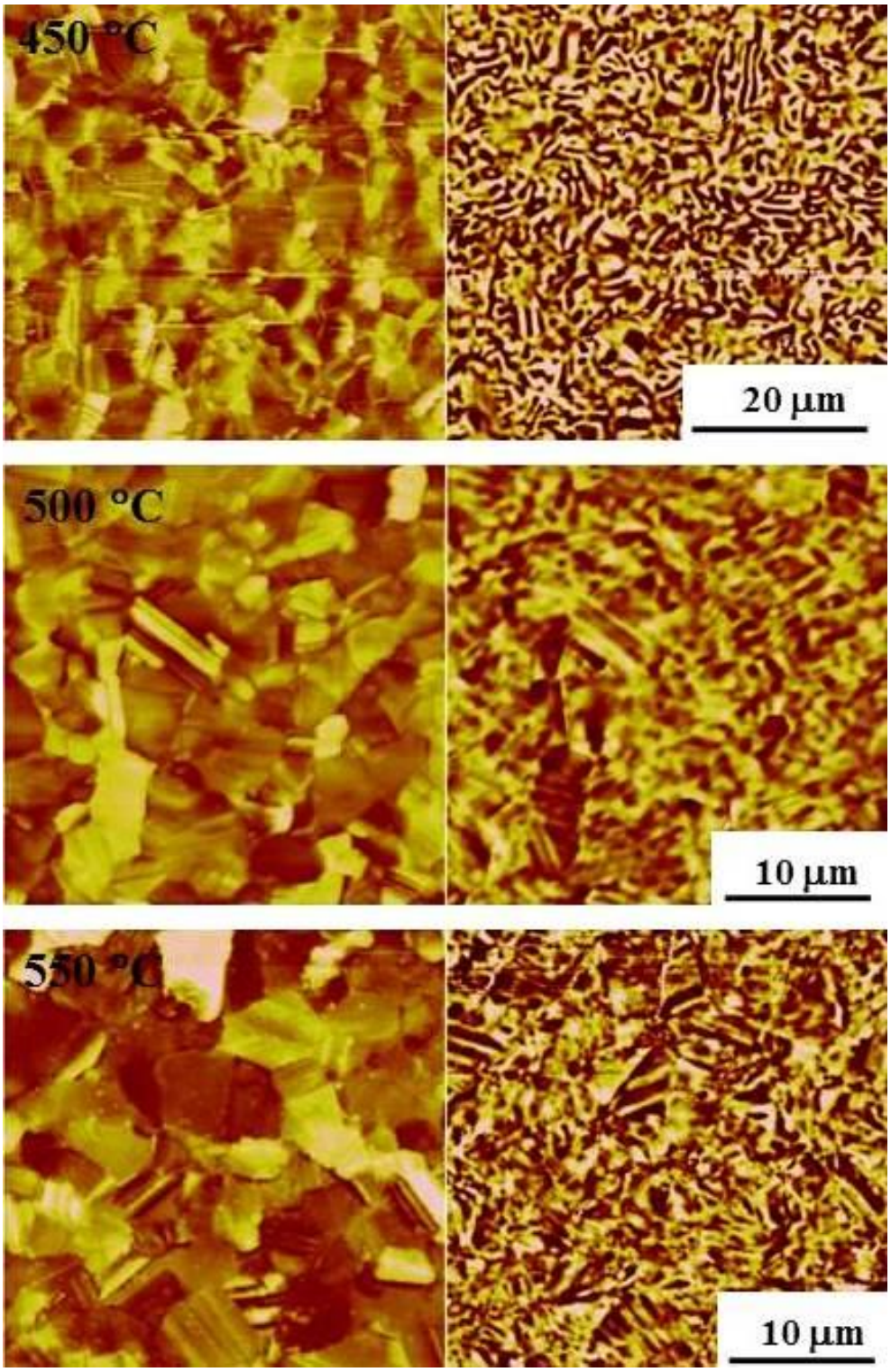

Figure 5.3. (cont.)

5.3. Expanded Phase (γ_N) Magnetism

The most important finding in this study is related to the magnetic nature of the expanded austenite layer on CoCrMo alloy. The γ_N phase/layer on CoCrMo is found to be ferromagnetic. The ferromagnetism is revealed through the observation of the stripe-like domains. The result is quite new and significant, since, to the authors' knowledge, this is the second study to date reporting ferromagnetism for the expanded phase in this alloy system. The original study (Öztürk et al., 2011), plasma nitriding of medical grade CoCrMo alloy with compositions similar to the one in this research, found that the expanded phase/layer formed at 400 ºC on this alloy has ferromagnetic properties as evidenced through the observation of stripe domains via MFM imaging and through hysteresis curves via MOKE. In comparison, there are quite a few studies reporting ferromagnetism for the γ_N phase/layer formed on austenitic stainless steels by various ion beam as well as gas nitriding processes (Wu et al., 2011).

In this and many other investigations, the ferromagnetism of the γ_N layers in austenitic SS and CoCrMo has been made clear through the stripe domain mapping by MFM imaging analysis (Fewell et al., 2000; Wu et al., 2011). MFM imaging is also carried out successfully on alloyed and unalloyed ferritic and/or dual phase stainless steels (DSS) as an alternative technique compared to destructive techniques such as chemical etching (Batista et al., 2013; Dias and Andrade, 2000).

A careful investigation of MFM images and comparison with the XRD data suggest a good correlation between the magnetic structure development of the surfaces of the N implanted CoCrMo samples and the development and decomposition of the expanded phase/layers on them. For example, the MFM image of the surface of the CoCrMo sample implanted at 350 ºC is composed of indistinct magnetic domains with weak magnetic contrast, while the imaging of the sample surface implanted at 400 ºC reveals distinct, stripe domains with strong magnetic contrast. The XRD results show that at the treatment temperature of 400 ºC, the expanded layer formation is complete with much thicker layer in comparison to the less developed γ_N layer on the sample processed at 350 ºC. This correlation also holds true for the 304 SS specimen that was N implanted at 350 ºC (MFM image containing stripe domains and XRD data indicating fully developed γ_N layer). The MFM image of the surface of the CoCrMo sample treated at 450 ºC also shows distinct stripe domain structures. The XRD results for this

sample suggest CrN precipitates within the expanded phase matrix. Apparently, the decomposed phase with precipitates in the sub-micrometer range still retains a memory of the original magnetic structure.

The MFM images in Figures 5.1, 2 and 3 show that domain morphology (size and shape) changes from grain-to-grain and even within a grain. This is attributed to N content and lattice expansion variations in these grains as evidenced from the XRD data. Also, it is likely that the γ_N has different intrinsic magnetic properties in differently oriented grains. In this study, the relationship between crystal orientation and the domain structure (for example, through both MFM and EBSD) has not been carried out, but few such studies do exist in literature, particularly for the expanded phase layer on SS alloy (Menéndez et al., 2008; Menéndez et al., 2010; Wu et al., 2011). There is no such study for the expanded phase layer on CoCrMo alloy. However, an alternative explanation involves plastic mechanical deformation due to the high stress values present in the expanded austenite layers. As dislocation lines are appearing at the surface within grains, exhibiting a regular, parallel spacing, an association of the domain boundaries within grains with these dislocation lines may be possible.

5.4. Physical Origin of Ferromagnetism in Expanded Phase

The ferromagnetic state for the γ_N phase/layers observed in this study is mainly linked to large lattice expansions (~ 9%) due to high N contents (~ 35 at.%) (Öztürk et al., 2011). As an interstitial impurity, nitrogen expands the host lattices of the stainless steel and CoCrMo alloy. At a more fundamental level, the origin of ferromagnetism in the γ_N phases comes from electronic structure of Fe (for stainless steel) or Co (for CoCrMo alloy) and more precisely from 3d orbitals. Expanding the lattice reduces the 3d-3d overlap enhancing Fe or Co magnetic moments. A plausible explanation related to the ferromagnetism observed in the expanded austenite layer in 316 SS was recently given by Basso et al (Basso et al., 2009). The authors claimed that the most important effect governing the ferromagnetism is the N-Cr interaction, which removes Cr 3d electrons from the metal alloy valence band promoting ferromagnetism. An earlier study (Blawert et al., 2001) suggested that both the lattice expansion and the defect density might be important for the magnetic properties of the expanded phase. This study indicated that fine changes in the atomic distances due to the stacking faults can

induce paramagnetic to ferromagnetic transformation (the expanded phase normally contains a high density of dislocations, slip lines, deformation twins, and stacking faults).

CHAPTER 6

COMPOSITION - DEPTH ANALYSIS

6.1. Compositional Characterization

Elemental compositions of the nitrogen implanted 304 SS and CoCrMo samples as well as substrate specimens were obtained by EDX. The compositions of the substrate samples determined by the EDX analysis are listed in Table 6.1, with respect to both at.% and wt.%. The results correlate well with the elemental compositions in Chapter 2 that were assessed by TIPSAN.

Table 6.1. The main elemental compositions obtained by EDX for substrate 304 SS and CoCrMo samples

		Fe	Cr	Ni
304 SS	wt.%	73.17	18.46	8.37
	at.%	72.79	19.38	7.83

		Co	Cr	Mo
CoCrMo	wt.%	66.77	27.97	5.26
	at.%	65.62	30.49	3.89

The EDX data were collected from the surfaces of substrate and N implanted samples. Consecutive EDX measurements were taken from three different areas. One measurement for each sample is performed on area of the selected images, as shown Figure 6.1.

Table 6.2 lists average elemental compositions of the nitrogen implanted 304 SS and CoCrMo samples. As can be clearly seen from Table 6.2, the average nitrogen concentration of the N implanted layers with respect to different implantation temperatures changes between 25 at.% and 40 at.% for 304 SS; between 31 at.% and 38 at.% for CoCrMo. The data presented in Table 6.2 correlates well with the SIMS nitrogen concentration depth results.

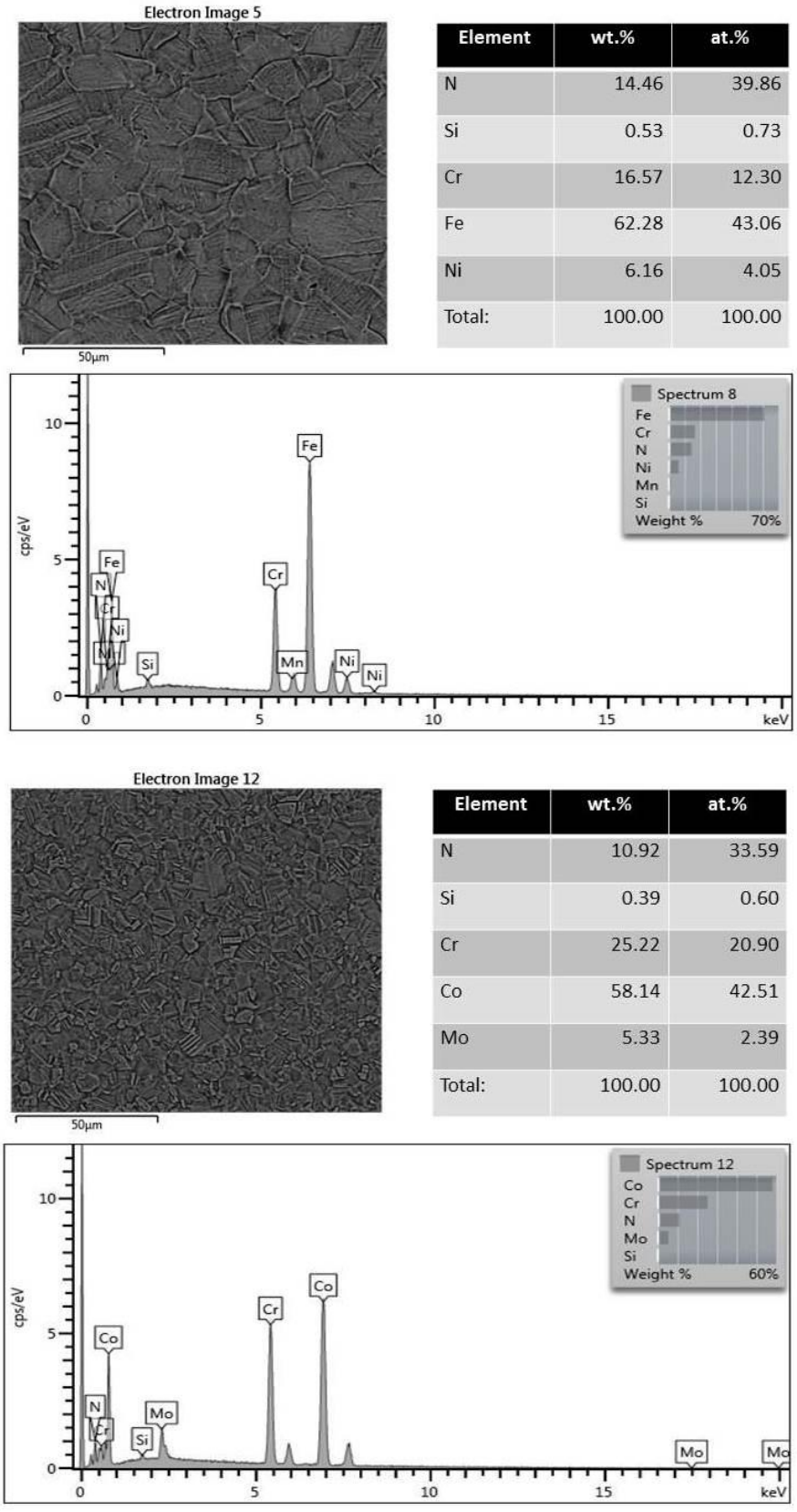

Figure 6.1. The EDX measurements of the N implanted 304 SS at 350 °C (upper data) and N implanted CoCrMo at 400 °C (lower data)

During nitrogen implantation, the nitrogen places octahedral sites in our substrate samples' crystal structure by decreasing the atomic weight concentration of the base atoms (Fe, Co, Cr, Ni) in the lattice. But, as can be noticed, for the samples processed at high temperatures 450 °C and above, the decrease in the atomic weight concentration of Cr is less compared to the concentration decrease of Fe and Ni in 304 SS; Co and Mo in CoCrMo sample. This may be attributed to the CrN formation in γ_N layer agreeing with the GIXRD results at processing temperatures of 450 °C and above.

Table 6.2. The EDX average elemental composition values of N implanted 304 SS and CoCrMo samples as well as substrates.

	wt.%				at.%			
304 SS	Fe	Cr	Ni	**N**	Fe	Cr	Ni	**N**
Substrate	73.17	18.46	8.37	**-**	72.79	19.38	7.83	**-**
300 °C	63.28	16.67	7.00	**12.57**	46.02	12.89	4.79	**36.09**
350 °C	62.58	16.49	6.57	**14.34**	43.76	12.27	4.32	**39.62**
400 °C	62.58	17.50	7.38	**12.30**	45.65	13.61	5.08	**35.51**
450 °C	65.66	17.58	7.15	**9.42**	51.11	14.55	5.24	**28.97**
500 °C	65.34	18.08	8.18	**7.75**	52.88	15.58	6.72	**24.79**
550 °C	63.97	18.02	10.32	**7.63**	52.00	15.58	7.90	**24.50**

	wt.%				at.%			
CoCrMo	Co	Cr	Mo	**N**	Co	Cr	Mo	**N**
Substrate	66.77	27.97	5.26	**-**	65.62	30.49	3.89	**-**
300 °C	57.84	25.04	5.17	**11.95**	41.58	20.26	2.26	**35.88**
350 °C	57.15	24.95	5.08	**12.80**	40.31	19.79	2.18	**37.71**
400 °C	58.21	25.23	5.35	**11.12**	42.75	20.81	2.38	**34.04**
450 °C	56.84	25.66	5.51	**11.97**	41.10	20.75	2.41	**35.93**
500 °C	57.91	25.80	5.55	**10.73**	42.90	21.47	2.50	**33.15**
550 °C	58.98	25.77	5.36	**9.87**	44.50	21.88	2.47	**31.13**

6.2. SIMS Nitrogen Concentration Depth Profiles

Nitrogen concentration profiles of the N implanted 304 SS and CoCrMo samples were obtained by SIMS as a function of depth. Figure 6.2 and Figure 6.3 indicate SIMS results of N implanted 304 SS and CoCrMo samples at different processing temperatures, respectively. As can be clearly seen from the figures, a comparison of the nitrogen depth profiles for both alloys presents a similar nitrogen distribution. The nitrogen concentration values are quite high at the surfaces of N implanted samples (ranging from ~20 to ~30 at.% for 304 SS; from ~30 to ~40 at.% for CoCrMo samples). At low processing temperatures (300, 350 °C), they decrease rapidly for both samples, while at higher processing temperatures (400, 450 °C), they decrease slowly to a level of ~15 at.% for 304 SS; ~20 at.% for CoCrMo and then decrease exponentially. The diffusion depth value reaches about 12 μm in 304 SS at 450 °C, whereas the diffusion depth in CoCrMo alloy is about 3.2 μm for the same treatment temperature. In this study, SIMS analyses were not performed for the nitrogen implanted 304 SS specimens at treatment temperatures of 500 and 550 °C due to time constraints.

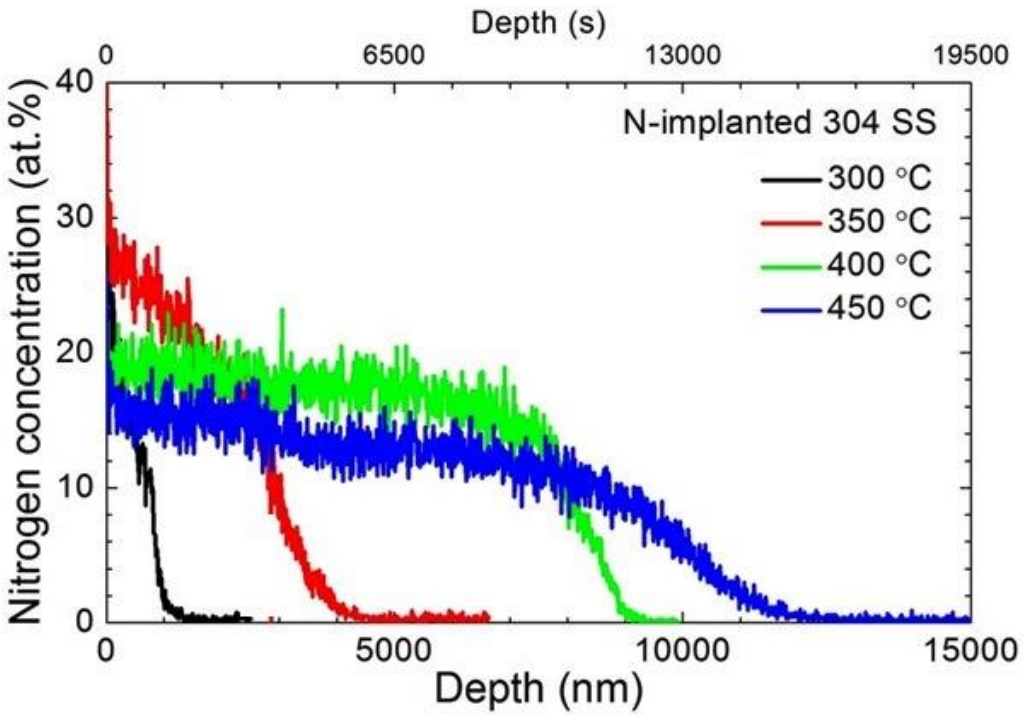

Figure 6.2. SIMS nitrogen depth profiles for N implanted 304 SS samples

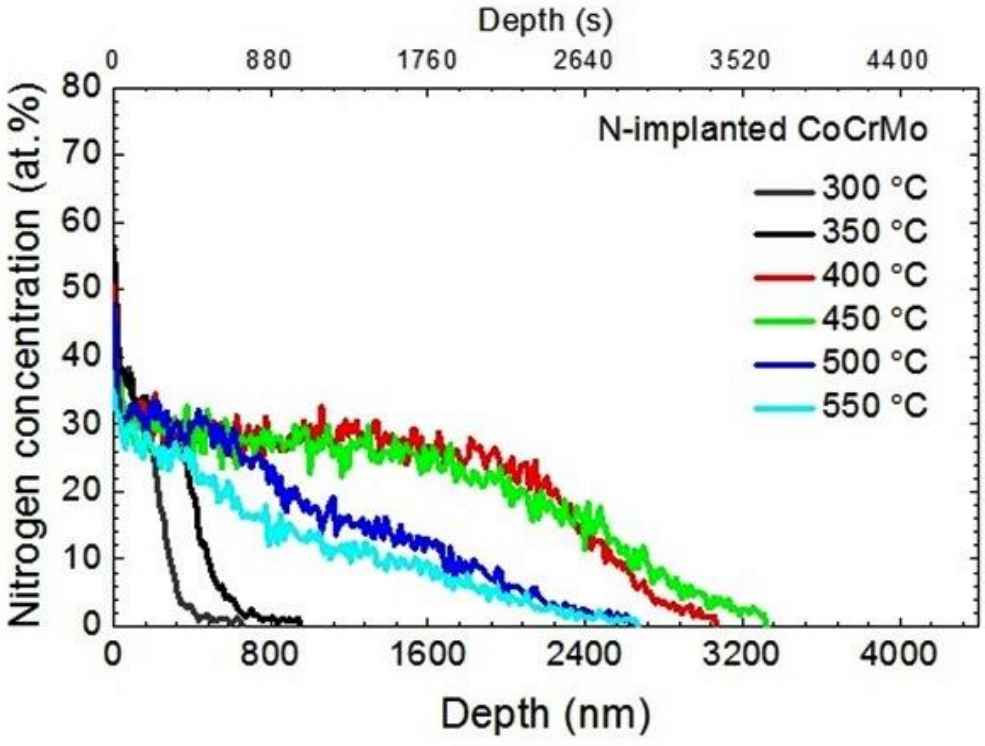

Figure 6.3. SIMS nitrogen depth profiles for N implanted CoCrMo samples

A study (Lutz et al., 2008b), investigating the nitrogen diffusion into CoCr alloys by plasma immersion ion implantation and plasma nitriding experiments at different treatment temperatures ranging from 250 °C to 600 °C, found out that the surface concentration of nitrogen reaches values between 30 and 35 at.%, nearly independent of the treatment temperature.

There are few studies (Lutz et al., 2008b; Lutz and Mändl, 2009) about the nitrogen diffusion in CoCrMo in the nitriding experiments, intended to explain the nitrogen diffusion. The nitrogen depth profiles in austenitic stainless steel (SS) and CoCr alloy (see Figure 6.2 and Figure 6.3) indicate plateau-type shapes slowly decreasing from surface, followed by a rather sharp leading edge. According to the nitrogen concentration profiles in the figures, the sharp decrease starts around 15 at.% for 304 SS; 20 at.% for CoCrMo alloy. The nitrogen profiles obtained for CoCr alloys in literature (Lutz et al., 2008a; Lutz et al., 2008b; Lutz and Mändl, 2009) correlate well with data related to the nitrogen diffusion in CoCrMo samples investigated in this study.

Another interesting feature in Figure 6.2 and 6.3 is the average nitrogen penetration depths of the N implanted samples. The N implanted layer thickness values obtained by SIMS nitrogen concentration depth profiles are given in Table 6.3.

Table 6.3. Thickness of nitrogen implanted layers obtained by SIMS results.

Temperatures T (°C)	Thickness for 304 SS (μm)	Thickness for CoCrMo (μm)
300	1	0.4
350	4	0.8
400	9	3
450	12	3.1
500	-	2.5
550	-	2.4

As mentioned in the experimental section, during the temperature increase in the PIII implantation process, pulse frequency is increased in order to raise the processing temperature. This leads to higher nitrogen penetration depths due to higher pulse frequencies which also mean higher N contents.

In a study (Manova et al., 2007), the thickness of the nitrided layer (plasma immersion ion implantation of 304 SS at 450 °C) are measured at 5 at.% of the nitrogen concentration in concentration-depth profile. The thickness values in Table 6.3 are estimated by taking 5 at.% (as a reference) nitrogen concentration of the leading edge of the nitrogen concentration depth profiles. The thickness values obtained from SIMS are quite consistent with the cross-sectional SEM results, which it will be mentioned in Chapter 7 (cross-section sample characterization).

Different nitrogen penetration depths for 304 SS and CoCrMo samples may be attributed to the different Cr contents. According to EDX results, the atomic concentration of Cr is ~20 at.% for 304 SS, whereas the atomic concentration of Cr is ~30 at.% for CoCrMo alloy. The Cr element might have a significant role in the nitrogen diffusion in 304 SS and CoCrMo samples during the nitrogen implantation. And also CoCrMo has a smaller grain size resulting in lower penetration depths in CoCrMo grains compared to 304 SS.

CHAPTER 7

CROSS – SECTIONAL CHARACTERIZATION

Cross-sectional characterization of the N implanted 304 SS and CoCrMo specimens were performed by using SEM. The cross-sectional sample preparation is described in the materials and experimental methods (Chapter 2). The aim of the cross-sectional characterization is mainly to estimate the N implanted layer thicknesses as well as to investigate the phases of the N implanted layers.

Cross-sectional SEM results for the N implanted 304 SS and CoCrMo specimens at the processing temperatures of 300, 400 and 500 °C are shown in Figure 7.1 and Figure 7.2, respectively. Note that the cross-sectional SEM images were taken under different magnifications for more detailed view of the implanted layer. However, here, SEM images obtained from same magnification were presented to compare thicknesses of N implanted layer on both alloys.

Figure 7.1 shows γ_N phase formations in the N implanted layers of 304 SS at all processing temperatures. At the lowest processing temperature of 300 °C, as seen in Figure 7.1, there is only formation of the γ_N phase on top surface and this expanded layer is quite thin. At higher processing temperature, 400 °C, the N implanted layer expands, along with the formation of a new phase, labelled as CrN. The γ_N phase and CrN in this N implanted layer were observed layer by layer via XRD and GIXRD. At the processing temperature of 500 °C, the N implanted layer is composed of γ_N, CrN, and also bcc α-(Fe,Ni) phase. These findings correlate well with surface topography results obtained both by SEM and AFM, where CrN precipitates in N implanted 304 SS samples processed at temperatures of 400 and 500 °C were observed.

Figure 7.2 indicates the formation of the γ_N phases in N implanted CoCrMo samples at the processing temperatures of 300, 400 and 500 C. At the lowest processing temperature of 300 °C, the thickness of the γ_N phase is very low compared to the N implanted 304 SS at the same processing temperature. The moderately low thickness of the N implanted layer was also determined according to the XRD and GIXRD results. At the higher processing temperature of 400 °C, the cross sectional SEM image clearly indicates a thicker N implanted layer. The thickness of layer of the N implanted sample

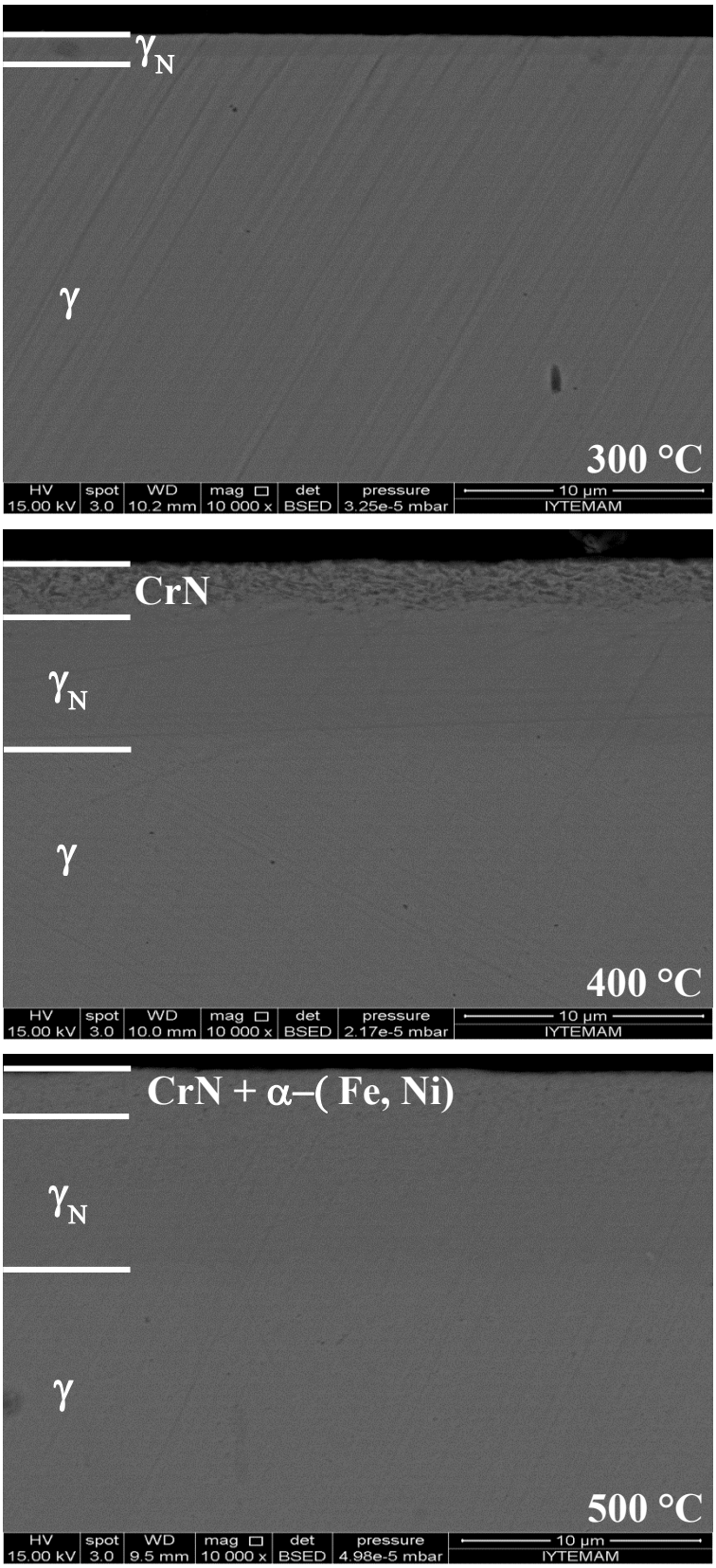

Figure 7.1. Cross-sectional SEM images of 300, 400 and 500 °C nitrogen implanted 304 SS (γ refers to substrate, γ_N refers to expanded phase)

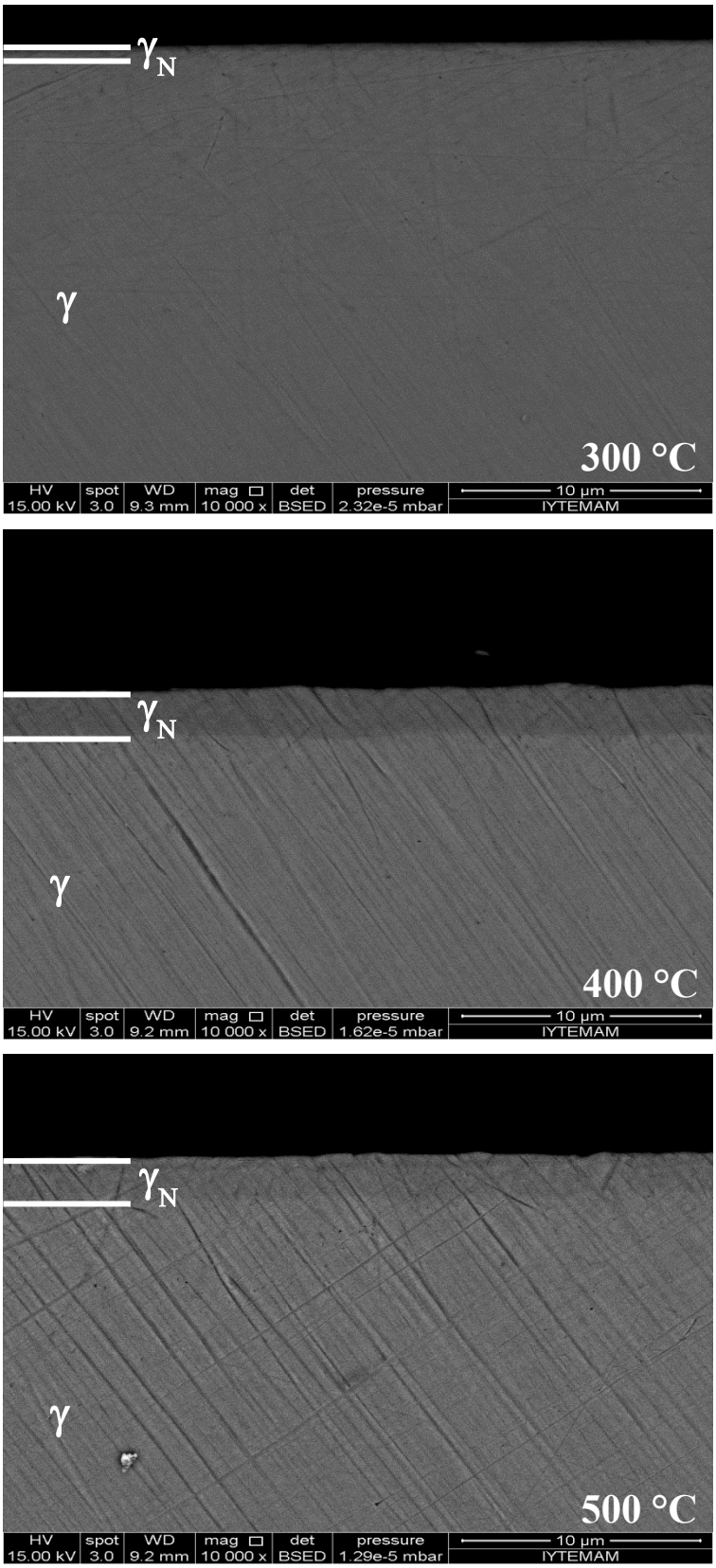

Figure 7.2. Cross-sectional SEM images of 300, 400 and 500 °C nitrogen implanted CoCrMo samples (γ refers to substrate, γ_N refers to expanded phase)

at the processing temperature of 500 °C was approximately the same with respect to the specimen N implanted at 400 °C.

The average thicknesses of the N implanted layers obtained from cross-sectional SEM analyses are listed in Table 7.1. The results presented in Table 7.1 are averages of the measurements taken from at least three different regions. According to the table, the thicknesses of the N implanted 304 SS samples are higher compared to N implanted CoCrMo alloys. The thickness of N implanted 304 SS at the processing temperature of 550 °C is approximately 15 μm, whereas, the thickness of N implanted CoCrMo at the same temperature is only about 2 μm. The results suggest that nitrogen diffusion in 304 SS is much higher compared to the CoCrMo alloys. This can be explained with the higher Cr content of CoCrMo alloy compared to 304 SS. And also, it may possibly be due to the smaller grain sizes of the CoCrMo alloy.

Table 7.1. Nitrogen implanted layer thicknesses obtained from cross-sectional SEM images.

Temperature (°C)	Thickness in 304 SS (μm)	Thickness in CoCrMo (μm)
300	1.11	0.24
350	3.24	0.48
400	10.10	2.55
450	11.50	2.70
500	14.90	2.36
550	15.13	2.06

SIMS and cross-sectional SEM data given in Table 6.3 and Table 7.1 respectively are plotted in Figure 7.3. As can be clearly seen from Figure 7.3, the thicknesses of the N implanted samples increase as a function of nitrogen PIII temperature due to the aforementioned chromium (Cr) content and grain size effects. And also, in the nitrogen PIII process, pulse frequency of ions is increased in order to raise the processing temperature. This leads to higher nitrogen penetration depths due to higher pulse frequencies.

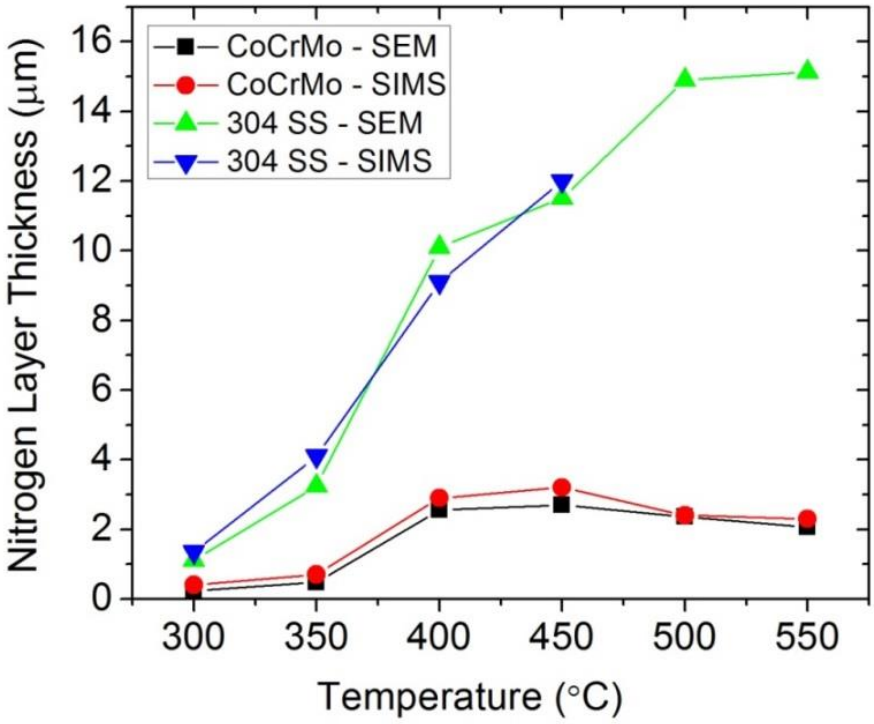

Figure 7.3. Nitrogen layer thickness of N implanted samples obtained from both SEM and SIMS results

According to cross-sectional SEM image of the N implanted 304 SS specimen at the processing temperature of 400 °C, N implanted layer was composed of CrN and γ_N phases. The distribution of CrN and γ_N phases in the N implanted layer was revealed in the XRD and GIXRD results that were given in Chapter 3. Depending on the XRD, GIXRD and cross-sectional SEM results, it can be said that the upper layer may be probably the CrN precipitates and the lower is expanded γ_N layer. The results correlate well with a study (Chen et al., 2008) in literature.

In the cross-sectional SEM results, γ_N-(Fe,Cr,Ni) observation is quite similar with our cross-sectional SEM results in the literature based on nitriding of austenitic stainless steels (Öztürk et al., 2009) and γ_N-(Co,Cr,Mo) observations based on nitriding of CoCrMo studies (Öztürk et al., 2006).

CHAPTER 8

SURFACE HARDNESS

This section covers surface hardness profiles of the substrate and the nitrogen implanted samples. The measurements were carried out by dynamic nanoindentation experiments using a Berkovich tip. Several indentations were made applying each of the following loads: 20 and 50 mN for each nitrogen implanted specimen.

The aim of this analysis was to investigate the hardness properties of N implanted surfaces compared to polished samples.

8.1. Substrate and N Implanted 304 SS

The hardness of the substrate and nitrogen implanted 304 SS samples are shown in Figure 8.1. The experiments were conducted with the substrate by applying loads of 10, 50, 100, 200, 300 mN and with the N implanted surfaces by applying loads of 20, 50 mN, respectively.

As can be clearly seen from Figure 8.1, for the polished 304 SS, at the lowest two applied loads (10-50 mN) higher hardness values were attained. This relatively high hardness values can be attributed to the martensite phase formation on the top surface of polished 304 SS. This martensite phase was also confirmed on the by the XRD and GIXRD results. On the other hand, the hardness values of the substrate decrease gradually larger indenter loads to smaller values. This can be explained by the fact that at higher indentation loads the penetration depth of the indenter increases resulting in more and more contribution from the substrate phase.

The hardness values for the N implanted 304 SS samples had a nearly 5 fold increase compared to the substrate. The increase in hardness values is attributed to only the expanded phase layer in N implanted sample at the processing temperature of 350 C. At higher processing temperatures the hardness increase is due to the composite matrix of CrN and expanded γ_N phases. Also compressive stresses effective in the N implanted layers might contribute to the hardness. However, the hardness of 304 SS sample processed at 300 °C was seen to be lower with respect to the N implanted samples

processed at other temperatures. According to the XRD, GIXRD and cross-sectional SEM results, the thickness of the γ_N layer processed at 300 °C is much thinner than the other N implanted samples. This results in more contribution from the substrate phase lowering the hardness values.

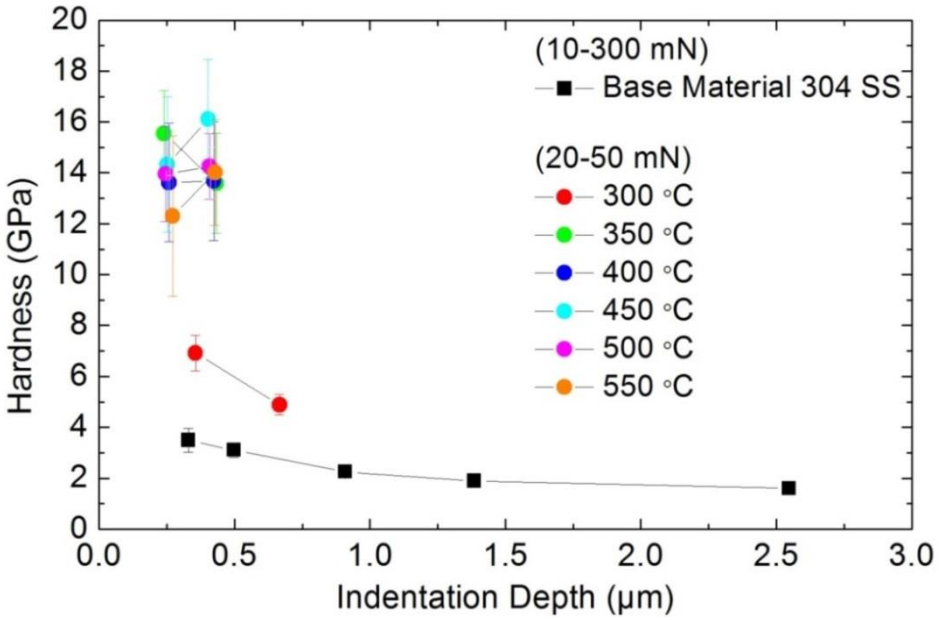

Figure 8.1. Hardness of substrate and N implanted 304 SS as a fuction of indentation depth (PIII processing temperatures from 300 to 550 °C)

One of the important points in the graph is the average indent depths of the indenter used in the hardness measurements. As can be seen in Figure 8.1, at the processing temperature 350 °C and above, the indentation depths change from ~ 0.25 μm (for 20 mN load) to ~ 0.4 μm (for 50 mN load). However, at lowest treatment temperature (300 °C), the indentation depth changes from ~ 0.35 μm to ~ 0.65 μm corresponding to applied loads 20 and 50 mN, respectively. As mentioned in the cross-section SEM and SIMS results, the thickness of the N implanted layer, at the treatment temperature (300 °C) is very thin compared to samples processed at other temperatures. According to these results, it can be explained that the indenter penetrates more in the N implanted layer at 300 °C compared to the sample at 350 °C.

8.2. Substrate and N Implanted CoCrMo

Figure 8.2 indicates the hardness values of the substrate and N implanted CoCrMo specimens. The hardness value (~ 5 GPa) of substrate CoCrMo sample is used as a reference, which is obtained from the literature. As can be seen from Figure 8.2, the hardness value is the substrate CoCrMo is about 5 GPa, wheras, at the lower processing temperatures of 300 and 350 °C the hardness values of the N implanted samples increase up to 6-7 GPa. The small hardness increase at low temperatures are due to the much more thinner γ_N layer compared to the N implanted CoCrMo samples processed at higher temperatures. As mentioned in the XRD, GIXRD and cross-sectional SEM results, γ_N layers on CoCrMo samples at lower processing temperatures (300 and 350 °C) are found to be significantly thinner compared to samples processed at higher temperatures. At the higher processing temperatures of 400 °C and above, the hardness values of the N implanted CoCrMo samples range between 12 and 15 GPa. This increase suggests the formation of only a thicker γ_N layer at the processing temperature of 400 °C. At higher processing temperatures (400, 500 and 550 °C), the increased hardness values of N implanted CoCrMo alloy may be due to CrN precipitates as well as the formation of γ_N phase.

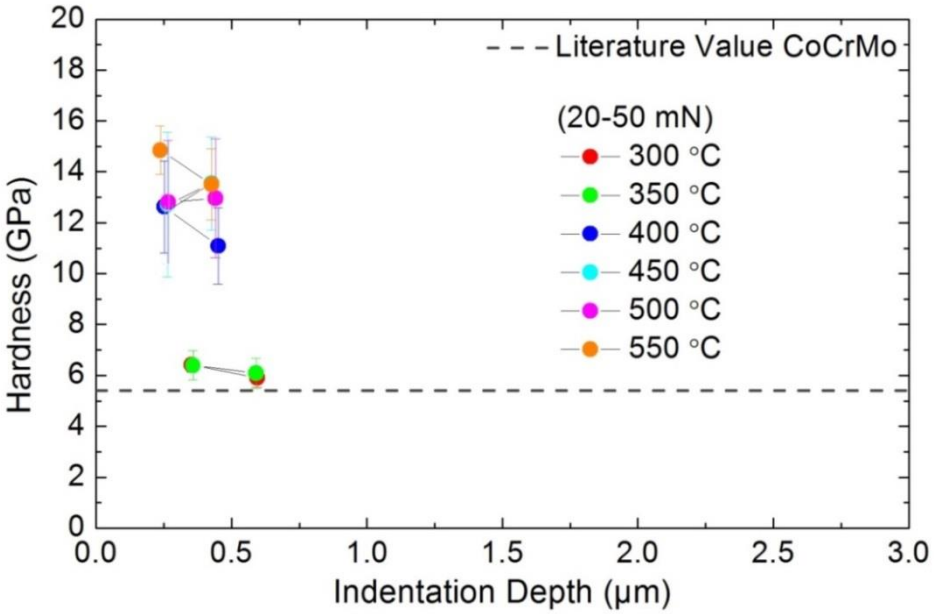

Figure 8.2. Hardness of substrate and N implanted CoCrMo as a fuction of indentation depth (PIII processing temperatures from 300 to 550 °C)

However, at lower processing temperatures (300, 350 °C), the hardness values of N implanted surfaces at 20 mN are quite close to the hardness value of the substrate material. Additionally, it could be seen that at higher indenter load, 50 mN, it approaches the hardness value of the substrate material. It is due to more contribution of substrate phase, as evidenced both XRD and GIXRD at low treatment temperatures of 300 and 350 °C.

These hardness results are in good correlation with the results obtained cross-sectional SEM, XRD and SIMS analysis. According to cross-sectional SEM results, thickness values of γ_N phase for CoCrMo samples were measured as thinner layer (~ 0.2 μm at 300 °C, ~ 0.5 μm at 350 °C) compared to other temperatures. Also, these results correlated quite well the nitrogen depth profiles obtained by SIMS. In addition, the both XRD and GIXRD data suggest that the N implanted CoCrMo processed at low temperatures have thinner layer in conjunction with the peaks of substrate phase.

CHAPTER 9

CONCLUSIONS

In this research, new data related to magnetic nature of the expanded austenite layer/phase formed on austenitic stainless steel (304 SS) and CoCrMo alloys by nitrogen plasma immersion ion implantation is investigated.

The ferromagnetism of the expanded phase layers is revealed through MFM imaging analysis of stripe-like domain structures. Combined MFM imaging analysis and XRD data suggest a correlation exists between the magnetic structure development and the expanded phase development and decomposition stages.

While distinct stripe domains with strong magnetic contrast are observed for the fully developed expanded phase layers on CoCrMo (also on 304 SS), indistinct domains with weak magnetic contrast are found for the expanded phase layer at earlier stages of its development (i.e. processing temperatures of 300, 350 ºC) and at the stage where the expanded phase matrix is decomposing into CrN precipitates and the Cr-depleted matrix, fcc γ-(Co,Mo) for CoCrMo alloy and CrN precipitates plus bcc α-(Fe, Ni).

The MFM data presented suggests that the expanded phase magnetic behavior is changing with crystallographic orientation and this is consistent with lattice expansion and N content variations as evidenced from the XRD.

Expanded phase, γ_N layers are produced in the range 1 to 15 micrometre for 304 SS and range 0.2 to 3 micrometre for CoCrMo, it changes due to different PIII processing temperatures.

The larger lattice expansions in the (200) planes are found compared to the (111) planes for the N implanted samples.

Comparing to polished 304 SS and CoCrMo specimens, the average roughness of the N implanted surfaces at highest treatment temperature of 550 °C increased about 15 and 60 times, respectively.

According to the SIMS profiles, the average nitrogen concentration reaches about ranging from ~20 to ~30 at.% for 304 SS; from ~30 to ~40 at.% for CoCrMo samples based on PIII processing temperature. The nitrogen is found to diffuse deeper in the 304 SS compared to CoCrMo alloys.

Significant hardness improvements are observed for the nitrogen implanted materials. The hardness increase is attributed to the formation of the expanded austenite layer at lower processing temperatures. With higher treatment temperatures, nanometer size CrN precipitates distributed within the γ_N matrix are contributing to the enhanced hardness.

REFERENCES

Baranowska, J. 2004. Characteristic of the nitride layers on the stainless steel at low temperature. *Surface and coatings Technology*. 180:145-149.

Basso, R., V. Pimentel, S. Weber, G. Marcos, T. Czerwiec, I. Baumvol, and C. Figueroa. 2009. Magnetic and structural properties of ion nitrided stainless steel. *Journal of Applied Physics*. 105:124914-124914-124915.

Batista, L., U. Rabe, and S. Hirsekorn. 2013. Magnetic micro-and nanostructures of unalloyed steels: domain wall interactions with cementite precipitates observed by mfm. *NDT & E International*.

Bazzoni, A., S. Mischler, and N. Espallargas. 2013. Tribocorrosion of Pulsed Plasma-Nitrided CoCrMo Implant Alloy. *Tribology Letters*. 49:157-167.

Blawert, C., H. Kalvelage, B. Mordike, G. Collins, K. Short, Y. Jirásková, and O. Schneeweiss. 2001. Nitrogen and carbon expanded austenite produced by PI< sup> 3</sup>. *Surface and Coatings Technology*. 136:181-187.

Brundle, C.R., C.A. Evans Jr, and S. Wilson. 1992. Encyclopedia of materials characterization: surfaces, interfaces, thin films. Gulf Professional Publishing.

Buhagiar, J., and H. Dong. 2012. Corrosion properties of S-phase layers formed on medical grade austenitic stainless steel. *Journal of Materials Science: Materials in Medicine*. 23:271-281.

Chen, J., X. Li, T. Bell, and H. Dong. 2008. Improving the wear properties of Stellite 21 alloy by plasma surface alloying with carbon and nitrogen. *Wear*. 264:157-165.

Collins, G., R. Hutchings, K. Short, J. Tendys, X. Li, and M. Samandi. 1995. Nitriding of austenitic stainless steel by plasma immersion ion implantation. *Surface and Coatings Technology*. 74:417-424.

Dias, A., and M.S. Andrade. 2000. Atomic force and magnetic force microscopies applied to duplex stainless steels. *Applied surface science*. 161:109-114.

Fewell, M., D. Mitchell, J. Priest, K. Short, and G. Collins. 2000. The nature of expanded austenite. *Surface and coatings Technology*. 131:300-306.

Gavriljuk, V.G., and H. Berns. 1999. High nitrogen steels: structure, properties, manufacture, applications. Springer.

H. Sanda, M. Takai, S. Namda, A. Chayahara, M. Satou, Appl. Phys. A. 50 (1990) 573

Kamachimudali, U., T. Sridhar, and B. Raj. 2003. Corrosion of bio implants. *In* Sadhana (Academy Proceedings in Engineering Sciences). Vol. 28. Indian Academy of Sciences. 601-637.

K. Ichii, K. Fujimura, T. Takase, Technol. Reports Kansai Univ., Vol. 127, 1986 p. 134.

Khatak, H.S., and B. Raj. 2002. Corrosion of austenitic stainless steels: mechanism, mitigation and monitoring. Woodhead publishing.

Lanning, B.R., and R. Wei. 2004. High intensity plasma ion nitriding of orthopedic materials: Part II. Microstructural analysis. *Surface and Coatings Technology*. 186:314-319.

Lutz, J., C. Diaz, J. Garcia, C. Blawert, and S. Mändl. 2011a. Corrosion behaviour of medical CoCr alloy after nitrogen plasma immersion ion implantation. *Surface and Coatings Technology*. 205:3043-3049.

Lutz, J., J.W. Gerlach, and S. Mändl. 2008a. PIII nitriding of fcc-alloys containing Ni and Cr. *physica status solidi (a)*. 205:980-984.

Lutz, J., A. Lehmann, and S. Mändl. 2008b. Nitrogen diffusion in medical CoCrNiW alloys after plasma immersion ion implantation. *Surface and Coatings Technology*. 202:3747-3753.

Lutz, J., and S. Mändl. 2009. Effect of ion energy and chemistry on layer growth processes during nitriding of CoCr alloys. *Nuclear Instruments and Methods in Physics Research Section B: Beam Interactions with Materials and Atoms*. 267:1522-1525.

Lutz, J., D. Manova, J.W. Gerlach, M. Stormer, and S. Mandl. 2011b. Interpretation of Glancing Angle and Bragg–Brentano XRD Measurements for CoCr Alloy and Austenitic Stainless Steel After PIII Nitriding. *Plasma Science, IEEE Transactions on*. 39:3056-3060.

Mandl, S., and B. Rauschenbach. 2000. Anisotropic strain in nitrided austenitic stainless steel. *Journal of Applied Physics*. 88:3323-3329.

Manova, D., T. Höche, S. Mändl, and H. Neumann. 2009. Development of CrN precipitates during the initial stages of PIII nitriding of stainless steel thin films. *Nuclear Instruments and Methods in Physics Research Section B: Beam Interactions with Materials and Atoms*. 267:1536-1539.

Manova, D., S. Mändl, H. Neumann, and B. Rauschenbach. 2007. Influence of grain size on nitrogen diffusivity in austenitic stainless steel. *Surface and Coatings Technology*. 201:6686-6689.

Menéndez, E., A. Martinavicius, M. Liedke, G. Abrasonis, J. Fassbender, J. Sommerlatte, K. Nielsch, S. Suriñach, M. Baró, and J. Nogués. 2008. Patterning of magnetic structures on austenitic stainless steel by local ion beam nitriding. *Acta Materialia*. 56:4570-4576.

Menéndez, E., J.-C. Stinville, C. Tromas, C. Templier, P. Villechaise, J.-P. Rivière, M. Drouet, A. Martinaviçius, G. Abrasonis, and J. Fassbender. 2010. Out-of-plane magnetic patterning on austenitic stainless steels using plasma nitriding. *Applied Physics Letters*. 96:242509-242509-242503.

Menéndez, E., C. Templier, G. Abrasonis, P. Garcia-Ramirez, J. Santiso, A. Vantomme, K. Temst, and J. Nogués. 2013. Magnetic properties of single crystalline expanded austenite obtained by plasma nitriding of austenitic stainless steel single crystals. *ACS applied materials & interfaces*.

Neves, B., and M. Andrade. 1999. Identification of two patterns in magnetic force microscopy of shape memory alloys. *Applied physics letters*. 74:2090-2092.

Öztürk, O., S. Okur, L. Pichon, M.O. Liedke, and J.P. Riviere. 2011. Magnetic layer formation on plasma nitrided CoCrMo alloy. *Surface and Coatings Technology*. 205:S280-S285.

Öztürk, O., S. Okur, and J. Riviere. 2009. Structural and magnetic characterization of plasma ion nitrided layer on 316L stainless steel alloy. *Nuclear Instruments and Methods in Physics Research Section B: Beam Interactions with Materials and Atoms*. 267:1540-1545.

Öztürk, O., U.u. Türkan, and A.E. Erogˇlu. 2006. Metal ion release from nitrogen ion implanted CoCrMo orthopedic implant material. *Surface and Coatings Technology*. 200:5687-5697.

Ozturk, O., and D. Williamson. 1995. Phase and composition depth distribution analyses of low energy, high flux N implanted stainless steel. *Journal of applied physics*. 77:3839-3850.

Pichon, L., S. Okur, O. Öztürk, J. Rivière, and M. Drouet. 2010. CoCrMo alloy treated by floating potential plasma assisted nitriding and plasma based ion implantation: Influence of the hydrogen content and of the ion energy on the nitrogen incorporation. *Surface and Coatings Technology*. 204:2913-2918.

Poon, B., D. Rittel, and G. Ravichandran. 2008. An analysis of nanoindentation in linearly elastic solids. *International Journal of Solids and Structures*. 45:6018-6033.

Pulido, M.D., and A.R. Parrish. 2003. Metal-induced apoptosis: mechanisms. *Mutation Research/Fundamental and Molecular Mechanisms of Mutagenesis*. 533:227-241.

Roth, J.R. 2002. Industrial Plasma Engineering: applications to nonthermal plasma processing. Vol. 2. CRC Press.

Seetharaman, V., and R. Krishnan. 1981. Influence of the martensitic transformation on the deformation behaviour of an AISI 316 stainless steel at low temperatures. *Journal of Materials Science*. 16:523-530.

Tavares, S., M. Da Silva, J. Neto, S. Miraglia, and D. Fruchart. 2002. Ferromagnetic properties of cold rolled AISI 304L steel. *Journal of magnetism and magnetic materials*. 242:1391-1394.

Walczak, J., F. Shahgaldi, and F. Heatley. 1998. In vivo corrosion of 316L stainless-steel hip implants: morphology and elemental compositions of corrosion products. *Biomaterials*. 19:229-237.

Wei, R., J. Vajo, J. Matossian, P. Wilbur, J. Davis, D. Williamson, and G. Collins. 1996. A comparative study of beam ion implantation, plasma ion implantation and nitriding of AISI 304 stainless steel. *Surface and Coatings Technology*. 83:235-242.

Williamson, D., O. Ozturk, R. Wei, and P. Wilbur. 1994. Metastable phase formation and enhanced diffusion in fcc alloys under high dose, high flux nitrogen implantation at high and low ion energies. *Surface and Coatings Technology*. 65:15-23.

Wozniak, M., A. Glowacka, and J. Kozubowski. 2005. Magnetic properties of austeno-ferritic stainless steel after cathodic hydrogen charging. *Journal of alloys and compounds*. 404:626-629.

Wu, D., H. Kahn, G. Michal, F. Ernst, and A. Heuer. 2011. Ferromagnetism in interstitially hardened austenitic stainless steel induced by low-temperature gas-phase nitriding. *Scripta Materialia*. 65:1089-1092.

Zhang, Z., and T. Bell. 1985. Structure and corrosion resistance of plasma nitrided stainless steel. *Surface Engineering*. 1:131-136.